Studies on Organic/Inorganic Nanocomposites of Lead Sulphide Quantum Dots in Solution-Processed Phthalocyanine Films

A thesis submitted by

Zahra Khozaee

in partial fulfilment of
the requirements of the degree of

Doctor of Philosophy

in the

School of Engineering and Materials Science
Queen Mary, University of London
Mile End Road
London, E1 4NS
UK

May 2012

School of Engineering and Materials Science
Queen Mary, University of London

PhD THESIS

DECLARATION

This thesis entitled

Studies on Organic/Inorganic Nanocomposites of Lead Sulphide Quantum Dots in Solution-Processed Phthalocyanine Films

was composed by me and is based on my own work. Where the work of the others has been used, it is fully acknowledged in the text, captions, tables and illustrations. This thesis has not been submitted for any other qualification.

Name Zahra KHOZAEE

Signed

Date May 2012

To my parents

and

beloved husband

Abstract

A unique organic/inorganic nanocomposite of lead sulphide (PbS) quantum dots (QDs) embedded in substituted metal-free phthalocyanine (C_6H_2Pc) has been prepared by a simple and low-cost method. The preparation procedure consists of exposure of a thin spun film of non-peripherally octa-hexyl lead phthalocyanine to hydrogen sulphide atmosphere. The formation of the PbS QDs has been verified using X-ray diffraction and transmission electron microscopy techniques. From the transmission electron microscopic measurements, the average size of the PbS QDs is found to be 4.5 nm, which is smaller than the exciton Bohr radius. Independent X-ray diffraction and optical absorption studies provide supportive evidence for the size of QDs.

Quantum confinement gives rise to a clear blue shift in the absorption spectrum with respect to the bulk PbS. The QDs band gap has been estimated to be 1.95 eV from Tauc's law and the frontier energy levels of the PbS QDs has been derived.

About two orders of magnitude increase in ohmic conductivity, from 6.0×10^{-12} for C_6H_2Pc to 3.1×10^{-10} for the nanocomposite, is observed by steady-state electrical measurements in sandwich structure between indium tin oxide and aluminium. Temperature-dependence of the electrical conduction is studied aimed to calculate the activation energy and determine the type of conductivity. The incorporation of the PbS QDs decreases the activation energy by about 0.5 eV at temperatures higher than 240 K. It is found that the Poole-Frenkel mechanism is in good consistency with the superlinear electrical behaviour of the nanocomposite.

The frequency response of alternating current (AC) conduction is found to obey the universal power-law. The cryogenic study of AC conduction reveals that the correlated barrier hopping (CBH) model closely fits to the experimental data at temperatures below 240 K. The parameters obtained by fitting the CBH model point out that the hopping process cannot take place directly between neighbouring PbS QDs but involves the localised states within the matrix.

Table of Contents

Title Page 1

Abstract 4

Table of Contents 6

List of Figures 10

List of Tables 18

Acronym 19

List of Symbols 22

Acknowledgments 26

Chapter 1 Introduction 27

Chapter 2 Background and Theoretical Outlines 34

2.1 Electronic structure of materials 34

2.2 Low-dimensional semiconductors: Quantum dots 37

2.3 Organic semiconductors 38

2.3.1 Electronic structure 39

2.3.2 Charge transport 40

2.4 Metal-organic semiconductor junction 41

2.4.1 Schottky contact 42

2.4.2 Ohmic contact 46

2.5 Conduction mechanisms in thin insulating films 47

2.5.1 Space-charge limited current 47

2.5.2 Poole-Frenkel 50

2.6 Alternating-current conduction 53

2.6.1 Correlated barrier hopping 54

2.6.2 Quantum-mechanical tunnelling 56

Chapter 3 Literature Review 57

3.1 Introduction to Phthalocyanines 57
3.1.1 Chemical structure 58
3.1.2 Derivatives 59
3.1.3 Electrical properties and applications 61
3.1.4 Optical properties and applications 63
3.1.5 Gas sensitivity 66
3.1.6 Bistable electrical behaviour 66
3.1.7 Frequency response 67
3.2 The importance of lead sulphide quantum dots 67
3.3 Nanocomposites 70
3.3.1 Preparation methods 71
3.3.2 Characterisation techniques 79
3.3.3 Calculation of particle size 83
3.3.4 Properties and applications 86

Chapter 4 Experimental Methods 98
4.1 Materials 98
4.1.1 Nanocomposite 98
4.1.2 Metal-free phthalocyanine 100
4.2 Preparation of C_6H_2Pc/PbS nanocomposite 100
4.2.1 Lead phthalocyanine film deposition 101
4.2.2 Exposure to H_2S atmosphere 103
4.3 Physical characterisation 104
4.3.1 X-ray diffraction 105
4.3.2 Transmission electron microscopy 107
4.3.3 Ultraviolet-Visible absorption spectroscopy 108
4.4 Electrical characterisation 110
4.4.1 Sandwich structure of Al-C_6H_2Pc/PbS-ITO 110

4.4.2 Employed equipments 114

Chapter 5 Material Characterisation 116

5.1 X-ray diffraction 116

5.2 PbS QDs size 117

5.3 Transmission electron microscopy 119

5.4 Compositional features 122

Chapter 6 Optical Absorption Spectroscopy 124

6.1 Optical absorption property 124

6.1.1 Absorption spectrum of C_6H_2Pc 126

6.1.2 Absorption spectrum of PbS QDs 127

6.2 PbS QDs band gap 130

6.3 PbS QDs size 132

6.4 Frontier energy levels of PbS QDs 132

Chapter 7 Steady-State Electrical Characterisation 134

7.1 Electrical conduction 134

7.2 Temperature-dependence 139

7.3 High-field conduction mechanism 141

Chapter 8 Impedance Spectroscopy 149

8.1 Experimental observations 149

8.2 Correcting the effect of lead resistance 154

8.3 AC conduction mechanism 161

8.4 Dielectric constant 166

Chapter 9 Conclusions and Future Work 170

9.1 Concluding remarks 170

9.2 Future work 172

Appendix 1 Standard database of Galena 177

Appendix 2 Particle in a 1-D box..... 180

References..... 181

List of Figures

Figure 2.1 Electronic structures of atom, molecule and bulk [9]. 35

Figure 2.2 A comparative energy band structure of insulators, semiconductors and conductors. 36

Figure 2.3 The size-dependence of band gap energy in quantum dots. QDs are able to emit light with different colours depending on their size. 38

Figure 2.4 π-electrons formed delocalised electron density above and below the plane of an ethylene molecule. 40

Figure 2.5 A typical Schottky contact for an n-type semiconductor. Energy diagram (a) before contact; (b) after contact: Mott-Schottky model; (c) after contact: vacuum level shift where E_{Fm} and E_{Fs} are the Fermi level energy of the metal and semiconductor respectively, E_c and E_v are the conduction and valence bands of the semiconductor, Φ_m is the work function of the metal, Φ_s is the work function of the semiconductor, Φ_B is the Schottky barrier height and χ is electron affinity. 43

Figure 2.6 The effect of applying an external voltage across a Schottky contact. The current increases exponentially in the forward bias while it has a very low amount in the reverse bias. 45

Figure 2.7 A typical ohmic contact for an n-type semiconductor. 46

Figure 2.8 Illustrative representation of the exponentially distributed traps within the forbidden gap. 50

Figure 2.9 Illustrative representation of the electron potential energy due to Coulombic potential and electric field. The amount of field lowering, $\Delta\phi = \beta_{PF} F^{1/2}$ 52

Figure 2.10 Illustration of the lowering of the hopping barrier height for two neighbouring sites in CBH model. 55

Figure 3.1 Typical structures of unsubstituted phthalocyanines, (a) metal-free phthalocyanine, (b) metallophthalocyanine (M stands for metal ion)... 58

Figure 3.2 Shuttlecock shape of metalophthalocyanines with large central atom such as Pb. 59

Figure 3.3 Ring numbering of a Pc molecule. 60

Figure 3.4 Example of chemical structures of substituted metal-free phthalocyanines, (a) identical, (b) non-identical substituted. R and R' can be any type of substituent groups such as alkyl, alkoxy or alkoxymethyl. 60

Figure 3.5 A diagrammatic representation of phthalocyanine categorisation..... 61

Figure 3.6 Schematic representation of an organic field-effect transistor. 62

Figure 3.7 Absorption coefficient of widely used materials compared to the standard AM 1.5 terrestrial solar spectrum. It shows that the absorption peak of phthalocyanine coincides with the maximum region of photon flux, taken from [23]. 64

Figure 3.8 (a) schematic representation of a bilayer structure organic solar cell; (b) band diagram of a bilayer structure organic solar cell. The created excitons are dissociated at the interface between the electron donor and acceptor. 65

Figure 3.9 Illustration of active frequency region for various applications. 68

Figure 3.10 LB film: schematic formation of PbS NPs in (a) monolayer and (b) multilayer of fatty acid LB film by exposure of Pb-arachidate LB film to H_2S gas. 73

Figure 3.11 Illustrative representation of nanocomposite preparation routes (a) wet-chemical method (b) solid state method. 75

Figure 3.12 Schematic representation of the organometallic synthetic procedure of PbS nanoparticles. The nanoparticles are capped with ligands consisting of a hydrocarbon chain and an end functional group dispersed in organic solvent. 75

Figure 3.13 Illustrative representation of gaseous deposition route for synthesising PbS nanocomposite. PbS cluster and organic vapour are deposited on the substrate simultaneously..... 77

Figure 3.14 High resolution image of PbS doped SiO_2-TiO_2 film. The indicated lattice spacing in the inset corresponds to 222 crystalline plane of PbS nanoparticle taken from [120]. 80

Figure 3.15 The calculation of β, full-width at half maximum, from the Bragg peak. 86

Figure 3.16 Different possible energy band diagrams of hybrid nanocomposites. (b,e) correspond to type I composites in which both energy levels (HOMO and LUMO) of one components lie inside the other one. The remaining cases (a,c,d,f) correspond to type II [122]..... 89

Figure 3.17 Illustration of basic processes taking place in organic/inorganic nanocomposite solar cells: (1) photogeneration of excitons in nanoparticles, (2) exciton diffusion, (3) exciton dissociated into separated charges at the interface and (4) transport of the separated charges to the opposite electrodes. 90

Figure 3.18 Photocurrent spectral responses and absorption spectra of MEH-PPV/PbS nanocomposite. The absorption peaks are tuned to 955(black), 1200 (red) and 1355 nm (blue) by changing the size of PbS QDs, taken from [81]. 91

Figure 3.19 Illustrative representation of carriers path between two electrodes in a nanocomposite..... 94

Figure 3.20 (a) The structure of memory device based on CdSe(ZnS)/PVK nanocomposite sandwiched between ITO and Al electrode; (b) the band

diagram of the device; (c) the bistable behaviour of the device under positive bias applied to ITO. The empty and filled rectangles in the plot show the on and off-state respectively and the solid line shows the recovered off-state after applying -2 V pulse, taken from [148]. 96

Figure 4.1 Chemical structures of 1-4-8-11-15-18-22-25-octa-hexyl lead phthalocyanine (C_6PbPc). 99

Figure 4.2 Chemical structures of 1-4-8-11-15-18-22-25-octahexylphthalocyanine metal-free (C_6H_2Pc) molecules. 100

Figure 4.3 Illustrative representation of static spin coating procedure. 103

Figure 4.4 Thin film of (a) C_6PbPc ;(b) C_6PbPc after exposure to H_2S gas, i.e. C_6H_2Pc/PbS nanocomposite; and (c) C_6H_2Pc, all prepared in the laboratory. 103

Figure 4.5 Illustrative representation of H_2S gas treatment set-up. 104

Figure 4.6 Illustrative concept of Bragg's law. 106

Figure 4.7 Illustration of the Beer Lambert law. I_0 is the incident light and I is the transmitted light. 109

Figure 4.8 Fabrication procedure of the sandwich structure device. 112

Figure 5.1 X-Ray diffraction pattern of (a) C_6H_2Pc/PbS nanocomposite, (b) pure C_6H_2Pc and (c) pure C_6PbPc. The observed Bragg's peaks correspond to PbS crystal planes have been marked by red lines. 118

Figure 5.2 TEM images of the C_6H_2Pc/PbS nanocomposite. The darker phases are the PbS quantum dots. 120

Figure 5.3 The selected-area diffraction pattern of (a) C_6H_2Pc/PbS nanocomposite, the two bright concentric circuits are related to 200 and 220 crystal planes of PbS, and (b) pure C_6H_2Pc. 121

Figure 6.1 The optical absorption spectrum of C_6H_2Pc/PbS nanocomposite. 124

Figure 6.2 Illustrative representation of a nanocomposite absorbance. The source light with the intensity of I_0 first passing through the matrix may result in partially absorbing the source light and reducing the intensity to I_1. The light with intensity of I_1 then further reduces to I by going through the nanoparticles. The total absorbance of the nanocomposite is thus expressed by $A_{NC} = -\log(I/I_0)$. 125

Figure 6.3 The absorption spectra of pure C_6H_2Pc film and C_6H_2Pc/PbS nanocomposite. The spectra of both materials were reproducible. 127

Figure 6.4 Optical absorbance spectra of: (a) C_6H_2Pc/PbS nanocomposite; (b) pure C_6H_2Pc scaled down by a factor of 0.85; (c) C_6PbPc film; and (d) the result of subtraction of curve (b) from curve (a). 129

Figure 6.5 Absorbance spectrum of ~4 nm PbS QDs in polymer (PVA), taken from [6]. The first excitonic peak occurs at about 580 nm. 129

Figure 6.6 The subtracted absorbance spectrum of the nanocomposite from pure C_6H_2Pc, Curve (d) in Figure 6.4. The peak around 600 nm is attributed to the first excitonic peak of the PbS QDs. The inset shows the estimated band gap energy of the produced PbS QDs using the absorption tail and Tauc's law. 131

Figure 6.7 Illustrative representation of the quantum confinement effect and the estimated increase in the band gap of the produced PbS QDs. The frontier energy levels of PbS QDs shift equally with respect to those of the bulk. 133

Figure 7.1 Steady-state electrical characteristic of sandwich structure devices at voltage sweeping from -2 V to +2 V. 135

Figure 7.2 Steady-state electrical characteristic of sandwich structure devices on log-log scale. The dashed lines show the unity slope of the ohmic regions. 135

Figure 7.3 Energy level diagram of C_6H_2Pc/PbS nanocomposite sandwiched between ITO and Al electrodes. Formation of ohmic contacts for holes

has been determined for both ITO and Al junctions, although based on MS theory a hole barrier is expected for Al electrode. 137

Figure 7.4 Temperature-dependence of (a) pure C_6H_2Pc and (b) C_6H_2Pc/PbS nanocomposite conductivity based on the Arrhenius plot. Two distinct regions are observable in the plots indicating the dominance of different conduction processes in different temperature regions. The activation energy at each region is determined from the slope of the fitted straight lines (dashed line) on the graphs. The experiment has been repeated five times and the average at each temperature is shown by an asterisk and deviation from average by an error-bar. 140

Figure 7.5 Plot of $\mathrm{Ln}(\sigma_{DC})$ versus $F^{1/2}$ corresponding to C_6H_2Pc device. The dashed lines show the linear-dependence of the graph at regions with high field effect. In the case of the Poole-Frenkel mechanism, the slopes of these lines determine the value of the field lowering coefficient of the Poole-Frenkel mechanism. 143

Figure 7.6 *J-F* characteristic of C_6H_2Pc device in log scale. The slopes of the fitted straight lines increase by lowering temperature. 145

Figure 7.7 Plot of exponent *l* vs. reciprocal temperature for C_6H_2Pc. The characteristic temperature, T_0, corresponding to exponential trap distribution is determined from the slope of the fitted line. The experiment has been repeated five times and the average at each temperature is shown by an asterisk and deviation from average by an error-bar. 145

Figure 7.8 *J-F* characteristic of C_6H_2Pc/PbS device in log scale. The slopes of the fitted straight lines increase by lowering temperature. 147

Figure 7.9 Plot of exponent *l* vs. reciprocal temperature for C_6H_2Pc/PbS device. The characteristic temperature, T_0, corresponding to exponential trap distribution is determined from the slope of the fitted line. The experiment has been repeated five times and the average at each

temperature is shown by an asterisk and deviation from average by an error-bar. 147

Figure 7.10 Plot of Ln (σ_{DC}) versus $F^{1/2}$ corresponding to C_6H_2Pc/PbS device. The dashed lines show the linear-dependence of the graph at regions with high field effect. The field lowering coefficient of the Poole-Frenkel mechanism can be calculated from the slope of these lines. 148

Figure 8.1 Frequency dispersion of (a) C_6H_2Pc and (b) C_6H_2Pc/PbS device conductivity at different temperatures. 152

Figure 8.2 Comparing the DC conductivity with the total conductivity of (a) C_6H_2Pc and (b) C_6H_2Pc/PbS device. The total conductivity is the summation of both AC and DC conductivity. The obtained conductivity of both materials was reproducible. 153

Figure 8.3 AC equivalent circuit of the devices. R_b, C_b and R_c representing, respectively, the bulk resistance, bulk capacitance and lead resistance. 155

Figure 8.4 (a) The real part of admittance of C_6H_2Pc device. (b) The imaginary part of admittance of C_6H_2Pc device; the inset is a scaled view of the plot and has the same axis labels. (Continued) 157

Figure 8.5 (a) The real part of admittance of C_6H_2Pc/PbS device. (Continued) ... 158

Figure 8.6 AC conductivity of (a) C_6H_2Pc and (b) C_6H_2Pc/PbS after correcting the effect of lead resistance. The frequency response of the devices is influenced by the lead resistance mainly at frequencies higher than 10^4 Hz at room temperature which shifts to lower frequency by decreasing temperature. 163

Figure 8.7 Fitting the CBH model to the experimental data of C_6H_2Pc device presenting by (a) temperature-dependence of the AC conductivity (b) temperature-dependence of exponent *s*. 164

Figure 8.8 Fitting the CBH model to the experimental data of C_6H_2Pc/PbS device presenting by (a) temperature-dependence of the AC conductivity (b) temperature-dependence of exponent *s*. 165

Figure 8.9 Frequency dispersion of dielectric constant of (a) C_6H_2Pc and (b) C_6H_2Pc/PbS device..... 168

Figure 9.1 The bistable electrical behaviour of C_6H_2Pc/PbS nanocomposite sandwiched between ITO and Al electrodes. The arrows show the direction of sweeping voltage; note that the device was already switched to high-conduction states, so the loop starts from high-conduction state. The high-conduction state can be retained by removing the power.... 175

List of Tables

Table 3.1 Summary of some of the reported syntheses of PbS nanocomposites. 78

Table 4.1 Detailed information of the materials used in this study: precursors of the nanocomposite and substituted metal-free phthalocyanine. 99

Table 5.1 Bragg's peaks corresponding to the PbS crystal planes in H_2S-treated sample. 117

Table 5.2 The calculation of PbS QDs size using the Scherrer equation. *D* is the average diameter of QDs. 118

Table 5.3 The calculated lattice spacing based on the diffraction pattern. 121

Table 5.4 Parameters regarding the distribution of the PbS QDs in the nanocomposite. 123

Table 7.1 Conductivity of C_6H_2Pc and C_6H_2Pc/PbS nanocomposite at different temperatures. 140

Table 8.1 Slope of the AC conductivity graph of C_6H_2Pc device in both frequency regions. The error of the listed values is not more than 2%. 154

Table 8.2 Slope of the AC conductivity graph of C_6H_2Pc/PbS device in both frequency regions. The error of the listed values is not more than 2%. 154

Table 8.3 Equivalent circuit parameters of C_6H_2Pc device. 160

Table 8.4 Equivalent circuit parameters of C_6H_2Pc/PbS device. 160

Table 8.5 Parameters applied for fitting the CBH model to the AC conductivity of the materials. 166

Acronym

AC	Alternating current
Al	Aluminium
C_6H_{13}	Hexyl
C_6H_{14}	Hexane
C_6H_2Pc	1-4-8-11-15-18-22-25-octahexylphthalocyanine metal-free
$C_6H_5CH_3$	Toluene
C_6PbPc	1-4-8-11-15-18-22-25-octahexylphthalocyaninato lead
C_7H_8	Toluene
CBH	Correlated barrier hopping
CdS	Cadmium sulphide
CdSe	Cadmium selenide
CdTe	Cadmium telluride
CH_4	Methane
CN-PPP	Poly(2-(6-cyano-6'-methylheptyloxy)- 1,4- phenylene)
CO	Carbon monoxide
CO_2	Carbon dioxide
CoPc	Cobalt phthalocyanine
CuPc	Copper phthalocyanine
DC	Direct current
E-MAA	Ethylene-15% methacrylic acid copolymer
eV	Electron volt
FePc	Iron phthalocyanine
FWHM	Full-width at half maximum
GaAs	Gallium arsenide
H_2Pc	Metal-free phthalocyanine
H_2S	Hydrogen sulphide
HCL	Hydrogen chloride
HOMO	Highest occupied molecular orbital
InSb	Indium antimonide
ITO	Indium tin oxide
LB	Langmuir-Blodgett
LUMO	Lowest unoccupied molecular orbital

MDMO-PPV	poly (2-methoxy-5-(3,7-dimethyloctyloxy))-1,4-phenylenevinylene)
MEH-PPV	Poly (2-methoxy-5-(2'-ethyl-hexyloxy)-p-phenylene vinylene)
MgPc	Magnesium phthalocyanine
MPc	Metallophthalocyanine
MS	Mott-Schottky
NaOH	Saturated sodium hydroxide
NH_3	Ammonia
NiPc	Nickel phthalocyanine
NO_x	Nitrogen oxide
OFET	Organic field-effect transistors
OLED	Organic light-emitting diodes
Ormocer	Organically modified ceramic
Ormosil	Organically modified silicates
P_3HT	Poly(3-hexylthiophene)
PB	Poly(1-Butene)
PbPc	Lead phthalocyanine
PbS	Lead sulphide
Pc	Phthalocyanine
PCBM	1-(3-methoxycarbonyl) propyl-1-phenyl[6,6]C_{61}.
PD	Poly (1-decene)
PE	Polyethylene
PEO	Poly(ethylene oxide)
PF	Poole-Frenkel
PMMA	Poly(methyl-methacrylate)
PS	Polystyrene
PVA	Poly(vinyl-alcohol)
PVK	Poly(N-vinylcarbazole)
PVP	Poly(vinyl-pyrrolidone)
P3HT	poly(3-hexylthiophene-2,5-diyl
QD	Quantum dot
QMT	Quantum-mechanical tunnelling
rpm	Revolutions per minute
SADP	Selected area diffraction pattern
SAM	Self-assembled monolayer
SCLC	Space-charge limited current

SEM	Scanning electron microscope
Si	Silicon
SiO_2	Silicon dioxide
SnPc	Tin phthalocyanine
SO_2	Sulphur dioxide
STM	Scanning tunnelling microscope
TEM	Transmission electron microscopy
TiO_2	Titanium dioxide
TioPc	Titanyl phthalocyanine
TPB	Tetraphenylbenzidine
UV	Ultraviolet
UV-Vis	Ultraviolet-visible
VL	Vacuum level
XPS	X-ray photoelectron spectroscopy
XRD	X-ray diffraction
ZnO	Zinc oxide
ZnS	Zinc sulphide

List of Symbols

a	Coefficient of the universal power-law
$a_{e,h}$	Bohr radius of holes or electrons
A	Optical absorbance
A	Effective area of the device (m^2)
c	Concentration of the absorbing material
C	A constant in Tauc's law
d	Thickness of the film (m)
d	Light path length (m)
d	Lattice spacing in crystals (m)
D	Diameter of a nanoparticle (m)
e	Electrical charge of an electron (eV)
E_c	Conduction band energy (eV)
E_F	Fermi level energy (eV)
E_g	Band gap energy (eV)
$E_g^{particle}$	Band gap energy of particles (eV)
E_g^{bulk}	Band gap energy of bulk PbS (eV)
E_t	Energy level of trap (eV)
E_v	Valence band energy (eV)
f	Frequency (Hz)
F	Electric field (V/m)
$h\upsilon$	Photon energy (J)
I	Electric current (A)
I	Intensity of transmitted light
I_0	Intensity of incident light
I_1	Intensity of the light after passing through the matrix
J	Current density (A/m^2)
J_0	Current density at low field (A/m^2)
k	Boltzmann constant (eV/K)
k	Geometric factor of the transmission electron microscope

l	X-ray wavelength (nm)
l	Camera length of the transmission electron microscope (m)
m	Effective mass (kg)
m_0	Real mass of an electron (kg)
m_e	Effective mass of an electron (kg)
m_h	Effective mass of a hole (kg)
M^{QD}	Molecular weight of QDs ($g.mol^{-1}$)
M^{Pc}	Molecular weight of C_6H_2Pc ($g.mol^{-1}$)
n^{QD}	Concentration of nanoparticles (m^{-3})
N	Carrier concentration (m^{-3})
$N(E_f)$	Density of states at the Fermi level (m^{-3})
N_0	Trap concentration at the valence band (m^{-3})
N_i	Intrinsic charge density (m^{-3})
N_v	Density of states at the valence band edge (m^{-3})
N_t	Concentration of traps in the energy level of E_t (m^{-3})
N^{NC}	Charge density of nanocomposite (m^{-3})
q	Electrical charge of an electron (eV)
r	Distance between the charge and the ionised state (m)
$\tilde{r}$	Distance between centres of two neighbouring particles (m)
R	Radius of the particles (m)
R_ω	Hopping/tunnelling distance (m)
s	Exponent of the universal power-law
T	Absolute temperature (K)
T_0	Characteristic temperature corresponds to exponential trap distribution (K)
V	Voltage (V)
V_{bi}	Built-in potential (eV)
w	Mass fraction of the PbS QDs (wt %)
W	Reduced barrier high (eV)
W_m	Maximum barrier high, i.e. the energy required to remove the electron from a site completely, (eV)

x	Volume fraction of the nanoparticles
α	Absorption coefficient
α	Spatial extent of the localised state wavefunction
β	Half-width of the Bragg peak
β_{PF}	Field lowering coefficient of the PF mechanism
ε	Dielectric constant (F/m)
ε_0	Permittivity of free space (F/m)
ε_a	Molar absorptivity (m^2/mol)
$\varepsilon_{\infty}^{PbS}$	Optical dielectric constant of lead sulphide (F/m)
Δ	Vacuum level shift (eV)
ΔE	Activation energy (eV)
θ	Incident angle (rad)
λ	Wavelength of the X-ray beam (nm)
λ	Wavelength of the electron beam (nm)
μ	Mobility of charges (m^2/(V.s))
μ^M	Mobility of charges in the matrix (m^2/(V.s))
μ^{NC}	Mobility of charges in the nanocomposite (m^2/(V.s))
μ^{NPs}	Mobility of charges in nanoparticles (m^2/(V.s))
ρ^{QD}	Density of PbS ($kg.m^{-3}$)
ρ^{Pc}	Density of C_6H_2Pc ($kg.m^{-3}$)
σ	Conductivity (S/m)
σ'	Real part of conductivity (S/m)
σ''	Imaginary part of conductivity (S/m)
σ_{DC}	DC conductivity (S/m)
σ_{AC}	AC conductivity (S/m)
σ'_{AC}	Real part of AC conductivity (S/m)
σ_0	Pre-exponential factor of conductivity (S/m)
σ_{DC}^{NC}	DC conductivity of the nanocomposite (S/m)
σ_{DC}^{Pc}	DC conductivity of C_6H_2Pc (S/m)

τ	Relaxation time (s)
τ_0	Inverse of optic phonon frequency (s)
ϕ	Potential barrier (eV)
ϕ_0	Ionisation energy (eV)
Φ_B	Schottky barrier height (eV)
Φ_m	Work function of metal (eV)
Φ_s	Work function of semiconductor (eV)
ω	Angular frequency (rad/s)
ϑ	Ratio of free to trapped carriers
$\hbar$	Reduced Planck constant (Js)

Acknowledgments

I would like to express my gratitude to my supervisor, Professor A. K. Ray for his valuable guidance, patience, enthusiasm and his critical comments. He provided an exciting, stimulating and open research environment at the department, which encouraged me to pursue my research eagerly. It has been a great honour for me to work with him and learn from him. I appreciate his vast knowledge and skill in many areas. I would like to thank the members of examining committee, Professor S. Kasap and Professors M. Edirisinghe for spending their valuable time on my dissertation. Special thanks go to Professor W. Gillin and Dr T. Kreouzis from the Physics department for their valuable supports during my experimentation.

Many thanks to Dr D. Mills, Dr Rory Wilson, Dr Z. Luklinska, Dr N. Chaure and Dr S. Chaure for their generous supports and guidance during my PhD programme.

I would also like to thank all my friends and colleagues at Queen Mary University of London, particularly Elnaz, Raheleh, Zainab, Marjan and Carlos.

Special thanks to my mum and dad for all the supports they provided me through my entire life and also my lovely sisters, Sara and Salma, for their encouragement. In particular, I must acknowledge my husband, Soheil, for his endless love, support, encouragement and patience. Without his support and encouragement, I could never have got this far.

CHAPTER 1

Introduction

Silicon-based devices have been employed in numerous electronic and optoelectronic devices since early 1900s. There have always been demands to find alternative materials with adjustable properties. The discovery of semiconducting behaviour of organic materials grew tendency towards replacing silicon with organic materials, especially by developing the nanoscience and feasibility of fabricating devices in nanoscale. Organic semiconductors have several advantages over conventional silicon; they are light weight, flexible, mainly soluble in organic solvent and able to be employed in devices by low-cost solution-processed techniques in a large-area production [1]. They are chemically diverse and their properties can be tailored by adding various substituents. However, the main problem of organic semiconductors is their low electrical conduction. This characteristic arises from the lack of high density of intrinsic carriers and also low charge mobility. The charge carriers in organic semiconductors can be increased by adding dopants to these materials, although this process is not as easy as it is in conventional semiconductors [2]. The mobility can be enhanced by controlling the growth condition of an organic film to improve its crystal structure, although it is still far from the high mobility of silicon

compounds [1]. Many efforts have been made to enhance the electrical properties of organic semiconductors to make them practically exploitable where light weight, low-cost, large areas and mechanically flexible devices are required.

Recently, the inclusion of inorganic nanoparticles into organic compounds has attracted growing interest [3]. Nanoparticles are nanocrystals with typically higher carrier transporting ability compared to organic semiconductors, and can be conducting particles such as gold, silver or semiconductors as small as quantum dots. The organic/inorganic nanocomposites have several advantages. By inclusion a high concentration of nanoparticle into an organic matrix, a continuous pathway for carries with higher mobility can be constructed inside the host matrix which increases the conductivity by orders of magnitude [4]. Organic/inorganic nanocomposites with high mobility pathways for both holes and electrons are viable candidates for organic electronic and optoelectronic devices such as photovoltaic devices [4]. In addition, quantum dots (QDs) with nanoscale dimensions have unique characteristics. The special feature of them is the capability to tune their band gap energy and consequently their optical and electrical properties by controlling their size. Combining them with an organic matrix provides a route to exploit the QDs in cost-effective plastic devices. Moreover, the combination of moieties paves the way to achieve the properties that none of the components can provide on its own. These properties are mainly arising from the existence of large interfacial area between two phases in a nanocomposite. By an appropriate selection of components, nanocomposites with specific physical [5], optical [6] and electrical [7] properties can be elaborately tailored.

In spite of all the advantages, constructing a homogeneous nanocomposite with well-distributed nanoparticles is still a challenging issue. Nanoparticles, in particular

quantum dots, have large surface potential energy and tend to join together in order to reduce their surface energy. Major efforts have been made to prevent nanoparticles from aggregation using effective stabilisers or capping agents. Therefore various sets of materials with different preparation routes are utilised to synthesise a nanocomposite.

In this research, a unique organic/inorganic nanocomposite of lead sulphide quantum dots embedded in substituted metal-free phthalocyanine has been prepared and characterised. The formation of PbS QDs in different matrix has been already reported, but the inclusion of PbS QDs in phthalocyanine compounds has been reported for the first time by Nabok and Ray in 2004 [8] and this work is built upon their preliminary research. This nanocomposite is constructed by a solid-state method with a two-step procedure: (1) fabricating the solution-processed thin film of substituted lead phthalocyanine; (2) exposure the film to hydrogen sulphide (H_2S) atmosphere. The simple and low-cost preparation route of this nanocomposite is mainly due to special features of non-peripherally octa-hexyl lead phthalocyanine (C_6PbPc), the precursor of this nanocomposite. Unsubstituted phthalocyanines have usually poor solubility in organic solvents, but C_6PbPc is substituted by long hexyl chains which makes it highly soluble in common organic solvents, and thus capable for deposition by solution-processed techniques. The other feature of this lipophilic lead phthalocyanine is having a degree of lead lability leading to easily release the central lead ions and formation of lead sulphide quantum dots by exposure to hydrogen sulphide gas. The rigid environment of the solid film prevents the aggregation of lead sulphide quantum dots, and thus there is no need to add any capping agents or surfactants to the composite.

This nanocomposite has been produced in the form of thin films, applicable to electronic and optoelectronic devices. Both the components, i.e. phthalocyanine and PbS QDs, are well-known for their optical features, and combining them can expand their applications in organic optoelectronic devices. But the main question is how the inclusion of PbS QDs in phthalocyanine affects the electrical property? And is there any improvement in the electrical conduction of the nanocomposite compared to that of the pure phthalocyanine? These questions are also addressed in this research. The device structure used to study the electrical property of the nanocomposite is a sandwich structure using indium tin oxide (ITO) and aluminium (Al) as electrodes. The employed electrodes are the ones usually applied in optoelectronic devices. ITO is a transparent electrode enables light to transfer to/from the active material, and is also able to be deposited on a flexible substrate which makes it favourable in fabricating flexible plastic devices. In addition, it acts as a hole-injecting electrode owing to the formation of ohmic contacts with most of the p-type organic semiconductors. Al is typically used as an electron-injecting electrode for organic semiconductors, although it acts as hole-injecting electrodes for the materials used in this study.

This thesis is comprised of the physical and electrical study on the constructed nanocomposite. It is initiated with the analysis of the nanocomposite by different means and confirming the formation of PbS QDs, and then follows by investigating the electrical property of the nanocomposite and the influence of PbS QDs on the electrical conduction of the nanocomposite. The aims and objectives of this study are summarised below:

- Preparing lead sulphide quantum dots embedded in the phthalocyanine matrix.
- Characterisation of the nanocomposite confirming successful formation of the PbS QDs.
- Study the optical absorption characteristic of the nanocomposite and investigate the quantum confinement effect in the PbS QDs.
- Study the steady-state electrical property as well as frequency response of the thin nanocomposite films sandwiched between two different electrodes.
- Study the possible influences of the PbS QDs on the dark electrical conduction of the nanocomposite in comparison with the pure matrix.

Outline of the thesis

Chapter 2 provides the background knowledge which is a prerequisite for this study. It contains the fundamental knowledge about the organic semiconducting materials and also low-dimensional semiconductors, i.e. quantum dots. The principle theories used to interpret the electrical behaviour of the nanocomposite are presented in this chapter.

Chapter 3 contains a literature review regarding preparations, properties and applications of nanocomposites, with main focus on the nanocomposites containing lead sulphide nanoparticles. The common characterisation techniques applied to analyse nanocomposites, and the methods widely used to calculate the size of nanoparticles are also included. Some parts of this chapter dedicate to introduce the special features and properties of phthalocyanines and lead sulphide quantum dots.

Chapter 4 presents the experimental methodologies employed in this research. It is initiated with the preparation procedure of the nanocomposite. The employed experimental techniques are then presented in two main sections corresponding to the physical and electrical characterisations.

Chapter 5 consists of the results obtained from the characterisation techniques, TEM and XRD, along with the analyses and discussions. The size of PbS nanoparticles is found by two different means providing a satisfactory evidence that they are quantum dots. The compositional features of the produced nanocomposite, such as volume fraction and concentration of PbS QDs, are mentioned at the end.

Chapter 6 presents the optical absorption spectrum of the nanocomposite and PbS QDs. The quantum confinement effect which is the main feature of quantum dots is also examined. The size of modified band gap and subsequently the frontier energy levels of the PbS QDs are determined. The shift of the PbS QDs' band gap is probed to estimate the size of the PbS QDs using the effective mass approximation model.

Chapter 7 presents the steady-state electrical behaviour of the nanocomposite films sandwiched between aluminium and indium tin oxide. The temperature- and field-dependence of the electrical conduction of the devices are evaluated in order to determine the dominant conduction mechanism in the nanocomposite. The electrical behaviour of the spun films of metal-free phthalocyanine in the identical device structure is also presented for the sake of comparison.

Chapter 8 addresses the frequency response of the nanocomposite conductance. The alternating field is applied to the thin nanocomposite films sandwiched between aluminium and indium tin oxide. By employing cryogenic measurement, the dominant AC conduction mechanism is found. Prior to the AC analysis, the effect of lead resistance is corrected.

Chapter 9 presents the concluding remarks of this study and the outline of the future work.

CHAPTER 2

Background

2.1 Electronic structure of materials

A molecule forms from bonding a group of atoms together. An overlap and interaction between atomic orbitals yields the formation of two types of the molecular orbitals simultaneously, bonding and anti-bonding. Bonding orbitals, such as σ-bond and π-bond, have higher energy (farther from vacuum level) compared to the original atomic orbitals, while the anti-bonding orbitals, such as σ^*-bond and π^*-bond, have lower energy than the original atom. The anti-bonding orbitals are mostly empty in the ground state of a molecule and will be filled by excitation of electrons from bonding orbitals. Two important concepts in the molecular scale are HOMO and LUMO which stand for the highest occupied molecular orbitals and lowest unoccupied molecular orbitals, respectively. The HOMO level is basically the highest bonding orbitals while the LUMO level is the lowest anti-bonding orbitals.

A bulk crystal is made of a number of molecules. If the interaction between the molecular orbitals of adjacent molecules is sufficiently strong, the molecular orbitals

overlap and the bands of energy are formed within the bulk. Due to a large number of molecules in a bulk, the energy gap between the molecular orbitals becomes so small resulting in the construction of nearly continuous energy bands rather than the discrete energy levels, as shown in Figure 2.1. Examples of strong interaction between molecules are covalent and ionic bond. The interaction between the HOMO levels of neighbouring molecules forms the valence band and similarly the overlap of the LUMO levels forms the conduction band. The energy gap between the conduction and valence bands is known as band gap energy. In the case of weak interactions between molecular orbitals, such as van der Waals bond, there is no or very narrow constructed band within the whole bulk and thus the structure of energy levels are mostly the same as the molecular orbitals; therefore such a bulk called molecular crystal.

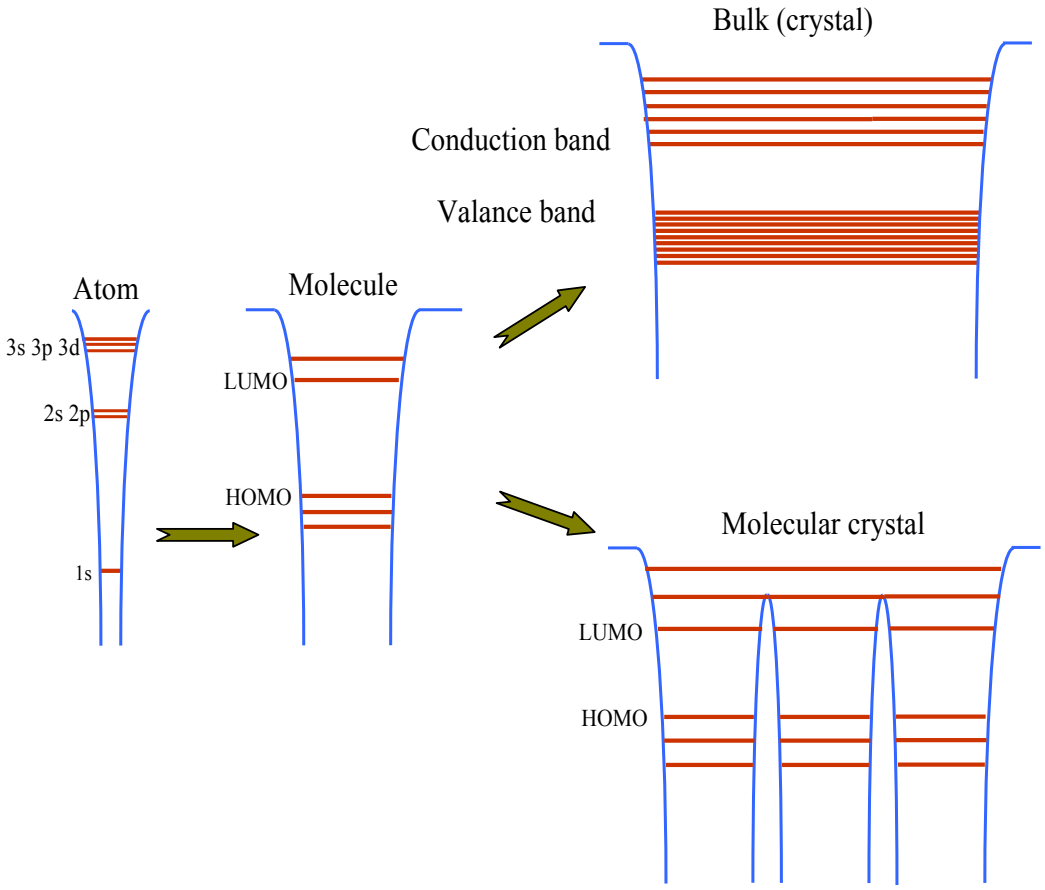

Figure 2.1 Electronic structures of atom, molecule and bulk [9].

The band gap energy is among the fundamental importance of the properties of materials and plays a vital role in most of their behaviours, such as intrinsic conductivity and optical transition. Any change in the gap may considerably alter the material's physics and chemistry. Accordingly, materials are categorised into three main groups based on their band gap energy: conductors, semiconductors and insulators. In conductors, the conduction band is partially filled and electrons can freely move. The current, thereby, flows easily in the presence of an external electric field. There is no band gap for conductors. In insulators, the valence band is fully occupied by electrons whereas the conduction band is empty. The band gap energy is much higher than thermal energy and almost no electron can be found in the conduction band and consequently no current can flow. In semiconductors, the valence band is completely filled; however the band gap energy is small enough so that the thermal excitation can transfer electrons to the conduction band and leave holes in the valence band. By applying an electric field, both electrons and holes can participate in current flowing. A comparative energy band structure of these three materials is shown in Figure 2.2.

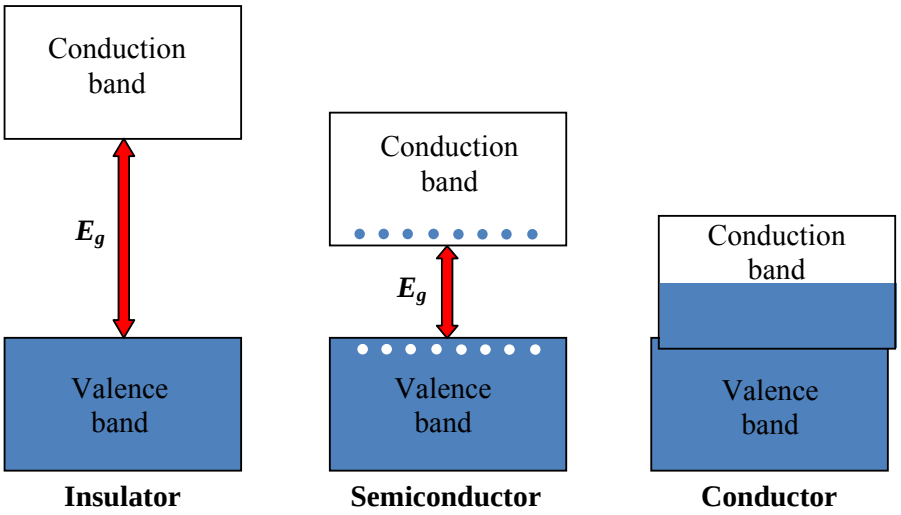

Figure 2.2 A comparative energy band structure of insulators, semiconductors and conductors.

2.2 Low-dimensional semiconductors: Quantum dots

As the size of bulk semiconductors shrinks to less than a few nanometers, most of the physical, optical and electrical properties are no longer similar to the bulk scale, although they exhibit bulk-like crystal structure. For instance the colour of gold quantum dots is red, and the wavelength of light emitted from a light emitting diode alters when the size of emitter centres is reduced to QDs size. These differences arise from the change in the electronic structure of these low-dimensional semiconductors, known as quantum dots (QDs), compared to the bulk. Quantum dots are regarded as artificial atoms since they are man-made objects with atom-like electronic band structures. By decreasing the size of bulk semiconductors, the gap between the energy levels increases, hence they are no longer treated as continuous but discrete levels. This effect is also known as quantum confinement since the size of QDs is too small which confines the motion of excitons (electron-hole pairs) inside the QDs. The confinement effect is the main characteristic of systems with confined dimensions and it provides the possibility to modify the band gap energy by varying the size of QDs; the smaller the size of a particular QD, the bigger its band gap energy [10]. In fact, by tuning the band gap of QDs, the properties of QDs are manipulated. As an example, the colour of emitted lights from a light emitting diode can be tuned by controlling the size of QDs, as graphically shown in Figure 2.3.

The main criterion to distinguish between bulk and QDs is the size of exciton Bohr radius [11]. Exciton Bohr radius is a physical distance between the electron and hole of an exciton in a bulk semiconductor. It is in the order of a few nanometres differing from one material to another. A particle is considered a quantum dot if its dimensions get smaller than its exciton Bohr radius. When the size of a semiconductor is getting lower than the physical distance between electrons and holes, these carriers are

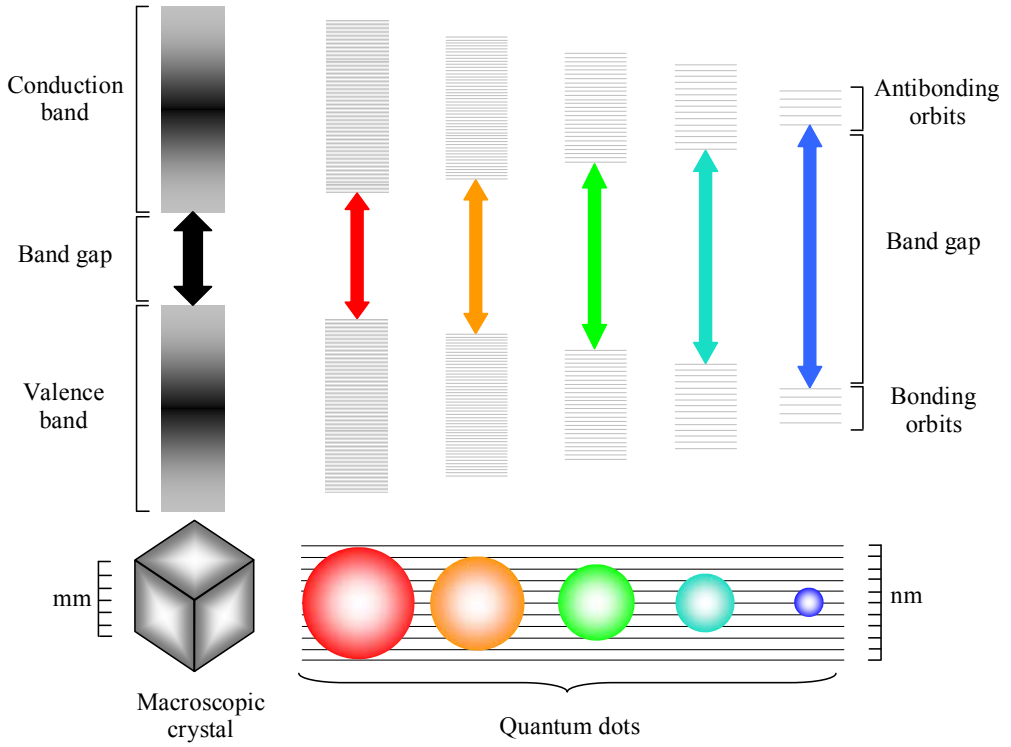

Figure 2.3 The size-dependence of band gap energy in quantum dots. QDs are able to emit light with different colours depending on their size.

confined leading to introduction of a confinement energy which is dominant over the Coulomb interaction energy between them [12]. Such confinement effects discretise the energy level and modify the band gap.

2.3 Organic semiconductors

In the middle of 20th century (1954) it was found that organic materials can conduct charge and be considered a new class of semiconductors [9]. They have attracted interests in device fabrications due to light weight, flexibility and possibility to be deposited by low-cost solution-processed techniques [9]. Besides, the diversity of organic semiconductors gives scientists a wide selection of compounds suitable for specific applications. Organic semiconductors, except some polymers, are molecular

crystals and this is one of the main differences between organic and inorganic semiconductors. The reason is arising from the weak van der Waals bonds between organic molecules, which cause the intramolecular force to become stronger than the intermolecular force. The weak interaction between energy levels of neighbouring molecules causes almost no energy band constructed within the crystal. Therefore the concepts of HOMO and LUMO are defined for a molecular crystal, analogous to the valence and conduction bands in inorganic semiconductors; see Figure 2.1.

Initially the application of organic semiconductors in electronic and optoelectronic devices could not attract interests due to low efficiency. However, the development of nanoscience and molecular electronics has opened new doors to fabricate efficient organic devices [13].

2.3.1 Electronic structure

All the electrical and optical properties of organic semiconductors can be explained by their specific electronic structure. In conjugated organic compounds (alternating sequence of single and double bonds in a molecule) when carbon atoms become close to each other, the neighbouring p_z orbitals overlap and form π-bond and π*-antibond. The π-bond is weak and can establish a delocalised electron density above and below the plane of carbon atoms, see Figure 2.4. The π-electrons locate in HOMO level and need a few electron volts (eV) energy to be excited to π*-orbital, i.e. LUMO, and participate in the charge transport.

2.3.2 Charge transport

In conductors and inorganic semiconductors, charge transport occurs in delocalised states within the whole crystal, i.e. band conduction mechanism. But in organic semiconductors the weak intermolecular coupling can hardly form a delocalised band

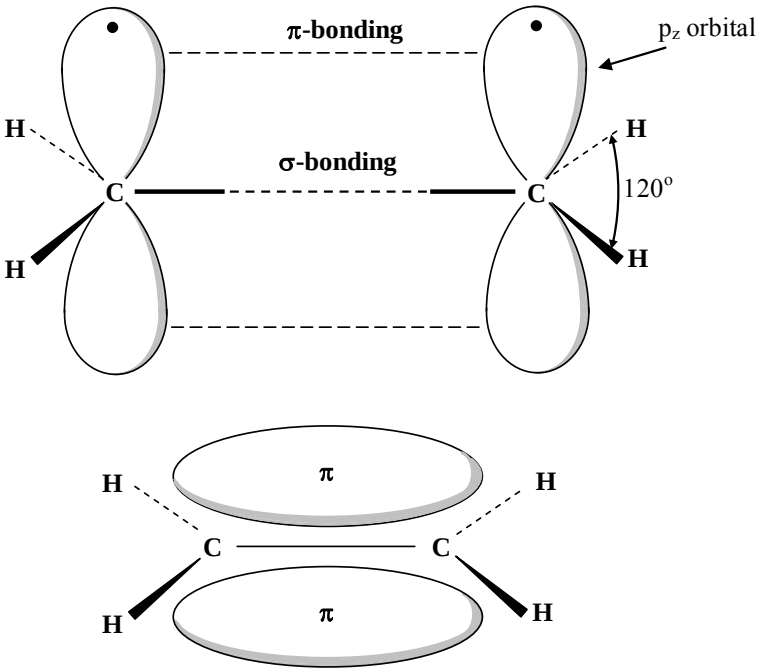

Figure 2.4 π-electrons formed delocalised electron density above and below the plane of an ethylene molecule.

within the whole crystal. The delocalised π-orbital in each molecule contains weak π-electrons which can hop between the molecules in the presence of an electric field and creates electrical current [14]. It should be noted that in highly ordered and purified molecular crystals, a narrow bandwidth may be formed, typically a few 10 meV wide [15]. This fact indicates that the mobility in organic semiconductors strongly depends on their crystal structure and purity. Generally the current density, J, through a material is expressed by Ohm's law

$$J = eN\mu F \tag{2.1}$$

where e is the electrical charge of an electron, N is the carrier concentration, μ is the mobility of charge and F is the applied electric field. The comparison of N and μ in organic and inorganic semiconductors can reveal the difference between these semiconductors in terms of conductivity. Mobility in organic semiconductors is low owing to the hopping charge transport mechanism. However, it can be improved by controlling the preparation and growing conditions of organic materials in order to have highly ordered and purified crystals. Nowadays the highest mobility values in organic thin films are comparable to amorphous silicon (Si) which is still much less than crystalline Si [16, 17]. The intrinsic charge density (N_i) in organic semiconductors is much lower than that of inorganic ones, e.g. N_i is in the range of 10^9-10^{13} m^{-3} for an organic semiconductor, whereas N_i is about 10^{16} m^{-3} for silicon with a band energy of 1.12 eV [1, 2]. The number of carriers can be increased by charge injection from contacts, photogeneration carriers and/or adventitious or purposely added dopant.

Despite the relative low conductivity of organic semiconductors, these materials are still in favour due to their advantages in plastic physics. The applications of organic materials in fabrication of several organic electronic and optoelectronic have been reviewed [18, 19, 20, 21, 22, 23].

2.4 Metal-organic semiconductor junction

Metal-semiconductor contacts are of great importance since they are present in every semiconductor device. When a metal is brought into contact with a semiconductor, their Fermi levels are aligned at equilibrium due to the difference in work function of metals and semiconductors. Work function is an important parameter that determines the minimum energy required to remove one electron from a material [24]. Proper

contact and interface between the metal and organic semiconductor plays a significant role in the performance and efficiency of organic-based electronic devices such as organic light emitting diodes, organic transistors and organic solar cells [25]. The charge injection and charge flow in devices are highly affected by the interface [13-15]. An efficient electron (hole) injection will occur when the Fermi level of a metal is almost at the same level of the LUMO (HOMO) level of an organic semiconductor, otherwise the charges should overcome the difference between these energy levels which limits the current considerably. Accordingly, two different types of contacts are defined: Schottky and ohmic, as explained below.

2.4.1 Schottky contact

Schottky contact refers to a metal-semiconductor contact when there is a potential barrier between the metal and semiconductor. This barrier restricts carriers passing through the interface, i.e. blocks current flowing from metal to semiconductor. A theoretical model, known as the Mott-Schottky model, is commonly used to describe metal-semiconductor junctions although it was found not to be followed by organic semiconductor junctions [26].

2.4.1.1 Mott-Schottky model

According to the Mott-Schottky (MS) model, when a metal with the work function of Φ_m is brought into contact with a semiconductor having the work function of Φ_s, the charge transfer occurs to align the Fermi levels in equilibrium; electrons move from the higher Fermi level to the lower Fermi level until the Fermi levels are aligned [24]. A contact is called Schottky if Fermi levels alignment is provided by the majority carriers transferring from the semiconductor to metal. Figure 2.5 shows a typical Schottky contact for an n-type semiconductor.

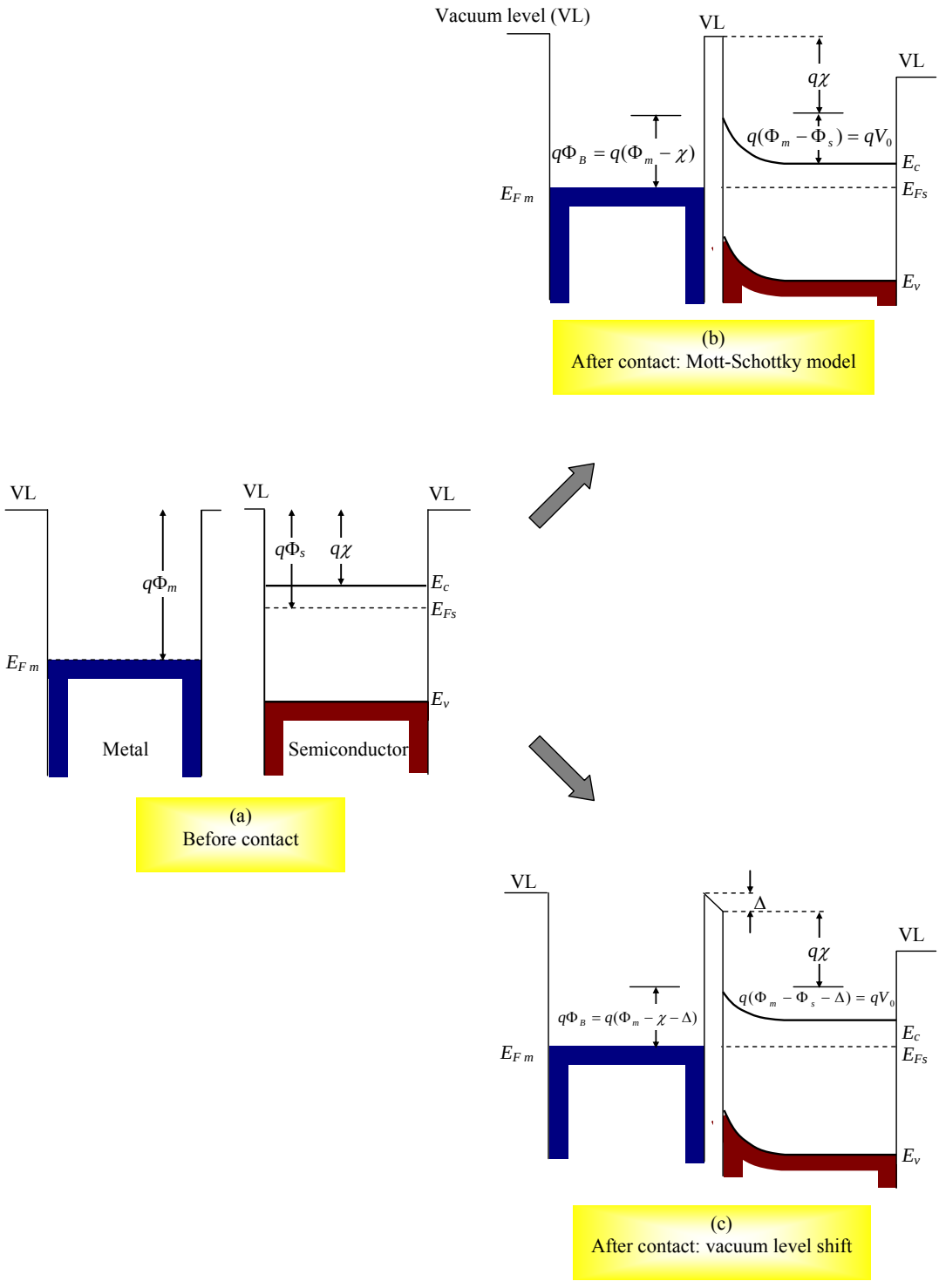

Figure 2.5 A typical Schottky contact for an n-type semiconductor. Energy diagram (a) before contact; (b) after contact: Mott-Schottky model; (c) after contact: vacuum level shift where E_{Fm} and E_{Fs} are the Fermi level energy of the metal and semiconductor respectively, E_c and E_v are the conduction and valence bands of the semiconductor, Φ_m is the work function of the metal, Φ_s is the work function of the semiconductor, Φ_B is the Schottky barrier height and χ is electron affinity.

The charge configuration at the metal-semiconductor junction produces an internal electric field which prevents further charge diffusion from the semiconductor to metal. This field which is known as contact potential or built-in potential, V_{bi}, is not uniform and has the maximum value at the interface, giving rise to bend the band energy at the interface. In fact the band bending shows the variation of semiconductor energy levels as a function of distance from the interface. The potential energy required for charges to move from the metal to semiconductor is called Schottky barrier height Φ_B. The current-voltage (*I*-*V*) characteristic at a Schottky barrier is an exponential function of Φ_B and the applied voltage. The amount of current depends on the direction of applied voltage, forward or reverse bias, as illustratively shown in Figure 2.6. In the forward bias, majority carriers move from semiconductor to metal and the built-in potential gradually decreases by increasing the voltage leading to increase the current. However the current is very low in the reverse bias as the carriers move from metal to semiconductor and must overcome the Schottky barrier height.

2.4.1.2 Vacuum level shift

The junction property of most organic-metal contacts does not follow the Mott-Schottky model due to the possible formation of a dipole interface layer which induces vacuum level shift (Δ) at the interface [26, 1, 25]. The interfacial dipole arising from the rearrangement of the electronic charges at the interface results in an abrupt change in the work function of semiconductors at the interface (or surface potential) compared to the MS model [26]. The abrupt change in the work function is graphically expressed by the shift of the vacuum level at the interface, which means there is no common vacuum level, anymore, at the interface between metal and

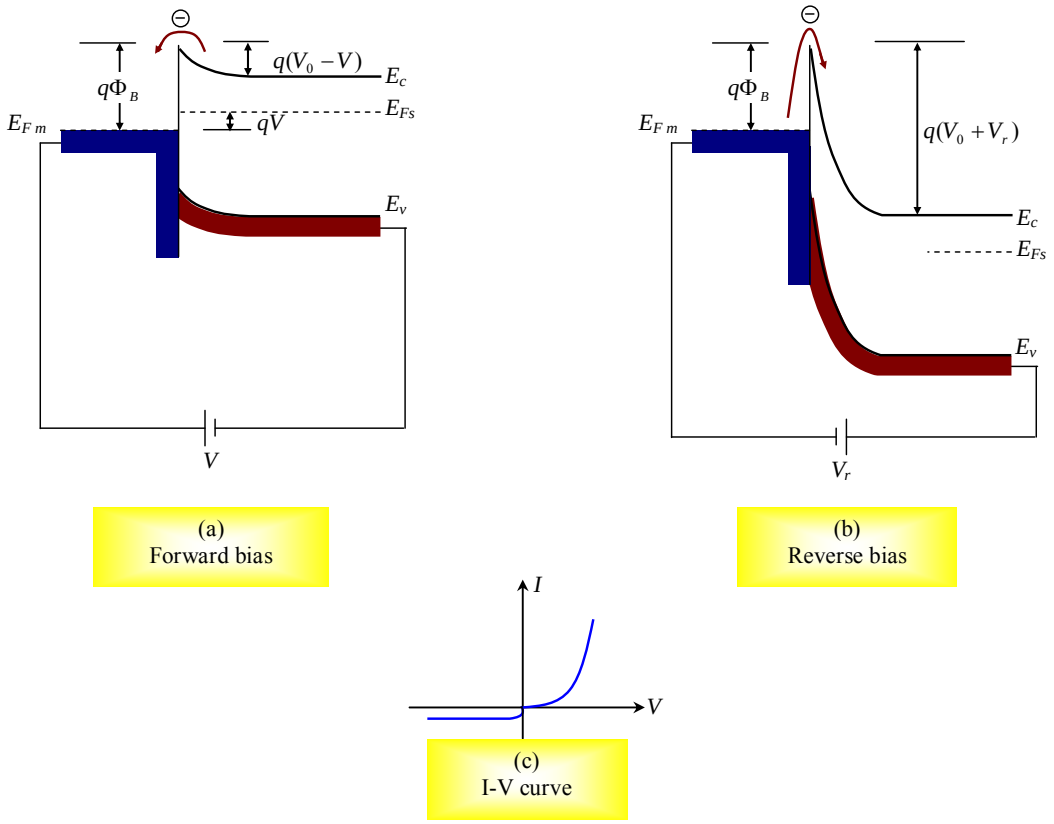

Figure 2.6 The effect of applying an external voltage across a Schottky contact. The current increases exponentially in the forward bias while it has a very low amount in the reverse bias.

semiconductor. Figure 2.5 shows a comparison between the MS model and the vacuum shift level model. The existence of the vacuum level shift leads to the modification of the barrier height estimated from the MS model by the amount of Δ. The mechanism of dipole layer formation is still unexplained, however a number of possible factors were proposed such as charge transfer between the metal and organic semiconductor, chemical reactions as well as the presence of permanent dipoles at the interface in the case of some organic materials [26]. Due to this fact, there is still no theoretical method proposed to predict the amount of Δ before making a contact between a metal and an organic semiconductor and consequently there is no way other than empirical observations to determine the charge injection barrier height at metal-organic junctions.

2.4.2 Ohmic contact

A contact is ohmic when the Schottky barrier height is zero or negative, however in some cases there exists a small barrier which can be easily overcome by a low voltage. In such a contact, the majority carriers transfer from the metal to the semiconductor in order to align the Fermi level [24]. The *I-V* characteristic follows Ohm's law in both biasing directions and the current is mainly restricted by the bulk resistance, since the contact resistance is negligible [27]. Figure 2.7 shows a typical ohmic contact for an n-type semiconductor. Apart from Schottky diodes and other rectifying devices, ohmic contacts are preferable in most devices due to their lower power consumption compared to Schottky contacts. However, fabricating ohmic contacts is not straightforward in organic semiconductors because of the formation of interfacial dipoles and also lack of high work function metals. Organic semiconductors are mostly p-type with HOMO level of around 5 eV. Therefore, theoretically, a high work function metal (≥ 5 eV) is required to make an ohmic contact [28].

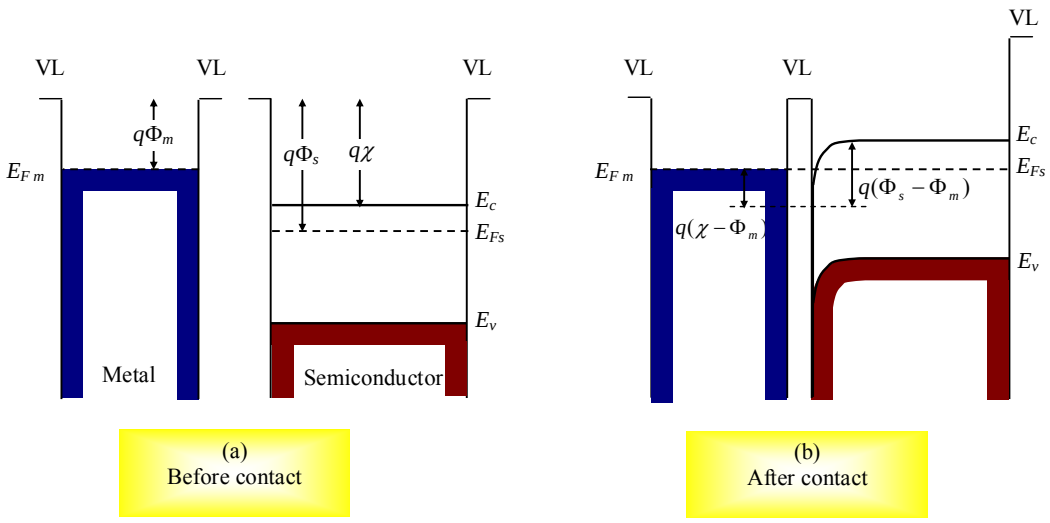

Figure 2.7 A typical ohmic contact for an n-type semiconductor.

2.5 Conduction mechanisms in thin insulating films

An electrical conduction follows Ohm's law in thin films when an ohmic contact forms at the electrode junction. Typically this linear-dependence between the current density and electric field (*J*-*F*) transforms to a superlinear behaviour at high fields, usually more than 10^6-10^7 Vm^{-1} [29]. The electrical behaviour of thin films inevitability involves the high-field conduction process due to very low thickness of films. Applying a potential difference of even 1 V across a 100 nm thickness film can generate a field as high as 10^7 Vm^{-1}. Besides, in insulators and organic semiconductors with high resistance, it is necessary to apply high field to the film in order to obtain measurable currents. Depends on the materials, different phenomena can be responsible for superlinear conduction behaviour including formation of space-charge which results in space-charge limited current, and ionisation of traps which describes by the Poole-Frenkel mechanism. These mechanisms are generally categorised in the bulk-limited conduction mechanism group in which the conduction process is only influenced by the bulk characteristic and not by the electrodes. The counterpart group is contact-limited conduction mechanisms which describe the conduction process in the presence of blocking contacts. It should be noted that the high-field electrical behaviour of a thin film may not be described by a single conduction mechanism as different phenomena can contribute to the conduction process simultaneously [29].

The fundamental relations of the common bulk-limited conduction mechanisms are described below, as a prerequisite to this investigation.

2.5.1 Space-charge limited current

By increasing the field, the number of charges injecting into the bulk increases

leading to formation of space-charge mainly at the interface. The formed space-charge creates an internal field in the opposite direction of the applied field and prevents more charges to be injected into the bulk and thus limits the current. The current density that is limited by formation of space-charge is called space-charge limited current (SCLC). This phenomenon generally occurs in low conductive materials, e.g. insulators. The space-charge is basically formed when the density of injected charges becomes dominant over the density of thermally generated carriers in the bulk. Accordingly, the SCLC is typically observed in devices with ohmic contacts with no restriction on charge injection.

By considering a non-uniform field in the bulk and applying the Poisson equation, the SCLC equation is written as [30]

$$J = \frac{9}{8}\varepsilon\varepsilon_0\mu\frac{V^2}{d^3} \tag{2.2}$$

where ε is the dielectric constant of the material, ε_0 is the permittivity of free space and d is the thickness of the film. This equation was originally derived by Mott and Gurney in 1948 [30].

However, in 1955 Rose proposed that the presence of traps reduces the space-charge limited current since the injected charges will fill the traps first [31]. The SCLC mechanism in the presence of single-layer trap is given by [31]

$$J = \frac{9}{8}\varepsilon\varepsilon_0\mu\vartheta\frac{V^2}{d^3} \tag{2.3}$$

where ϑ is the ratio of free to trapped carriers defines by

$$\vartheta = \frac{N_v}{N_t}\exp\left(-\frac{E_t}{kT}\right) \tag{2.4}$$

where N_v is the effective density of states at the valence band edge, N_t is concentration of traps in the energy level of E_t, k is the Boltzmann constant and T is

the absolute temperature.

The ratio ϑ is temperature-dependent and reduces the current density compared to trap-free SCLC. In the presence of traps, the space-charge, which limits the conduction, is stored in the traps. When all the traps are filled, the current density increases sharply and reaches to the trap-free SCLC, Equation (2.2).

Lampert then extended the SCLC theory for the case in which traps distribute exponentially in the forbidden gap, see Figure 2.8. The density of traps per unit energy at an energy *E* above the valence band edge (in the case of hole traps) can be defined by [31]

$$N_t(E) = N_0 \exp\left(-\frac{E}{kT_0}\right) \tag{2.5}$$

where N_0 is the trap concentration at the valence band and T_o is called characteristic temperature corresponding to the trap distribution. The SCLC with exponential trap distribution is then expressed as [32]

$$J = eN_v\mu\left(\frac{\varepsilon\varepsilon_0}{eN_0kT_0}\right)^l \frac{V^{l+1}}{d^{2l+1}} \tag{2.6}$$

There is, therefore, a power-law dependence of $J \propto V^{l+1}$ where l is temperature-dependent and defined by $l = T_o/T$.

The current density sharply switches from ohmic behaviour to the SCLC in the case of single-level trap while the transition is more gradual in the case of exponential trap distribution [33].

It should be noted that all the mentioned SCLC equations are for the case of single carrier injection.

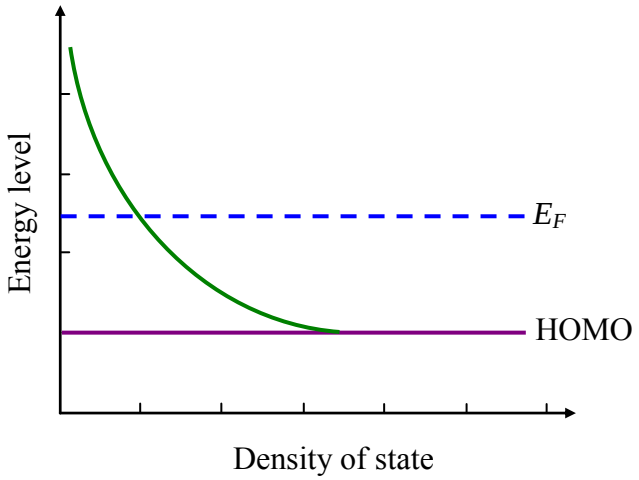

Figure 2.8 Illustrative representation of the exponentially distributed traps within the forbidden gap.

2.5.2 Poole-Frenkel

In insulators and wide band gap semiconductors the thermal energy is basically not sufficient to excite large density of carriers form the valence band to the conduction band. In such cases, the low current density is observed mainly corresponds to the carriers provided by thermal ionisation of localised states lying energetically within the band gap of the materials. The Poole-Frenkel (PF) mechanism describes lowering the ionisation energy in the presence of electric field, when the ionisation potential barrier follows a Coulombic form, as illustrates in Figure 2.9.

According to the definition of the PF mechanism, neutral traps cannot manifest the Poole-Frenkel effect. To experience the Poole-Frenkel effects, traps should be charged states, i.e. they are charged when empty and uncharged when filled by carriers [34]. The charged traps have a Coulombic-type barrier; removing a carrier from a filled trap puts the carrier in the Coulombic potential of the ionised trap.

The potential barrier for removing a carrier from a Coulombic potential well is defined by

$$\phi(r) = \phi_0 - \frac{e^2}{4\varepsilon\varepsilon_0 \pi r}. \tag{2.7}$$

where ϕ_0 is the ionisation energy, e is the electric charge of an electron, ε is the high-frequency dielectric constant, r is the distance between the charge and the ionised state. By applying an electric field (F), the potential barrier is lowered in the direction of field and expressed by

$$\phi(r) = \phi_0 - \frac{e^2}{4\varepsilon\varepsilon_0 \pi r} - eFr \tag{2.8}$$

The maximum value of $\phi(r)$ is $\phi_0 - \beta_{PF} F^{1/2}$ at $r_m = \left(4\pi\varepsilon_0 \varepsilon F / e\right)^{-1/2}$, where β_{PF} called field lowering coefficient and defined by

$$\beta_{PF} = \left(\frac{e^3}{\varepsilon\varepsilon_0 \pi}\right)^{1/2} \tag{2.9}$$

The Poole-Frenkel equation is then defined by

$$J = J_0 \exp\left(\frac{\beta_{PF} F^{1/2}}{2kT}\right) \tag{2.10}$$

where $J_0 = \sigma_0 F$ is the current density at low field (Ohm's law).

In 1962, Mead has suggested that in the case of thin insulator films with almost universally presence of traps distribution, Equation (2.10) is modified as [35]

$$J = J_0 \exp\left(\frac{\beta_{PF} F^{1/2}}{kT}\right) \tag{2.11}$$

The theoretical equation of the PF mechanism is very similar to Schottky emission theory which is one of the well-known contact-limited mechanisms, although they are principally two different phenomena. Distinguishing between these mechanisms is not straightforward if the type of contact is unknown. The electrical characteristic of a device should be independent of bias polarity, electrode materials, device area and film thickness, at a given field, in the case of the PF effect [36].

The above relation only considers the reduction of Coulombic barrier in the direction of filed. In 1968, Hartke [37] modified the PF mechanism to a three-dimensional case in which the potential barrier is defined by

$$\phi(\vec{r}) = \phi_0 - \frac{e^2}{4\varepsilon\varepsilon_0 \pi r} - e\vec{F}\cdot\vec{r} \tag{2.12}$$

which can be written by

$$\phi(\vec{r}) = \phi_0 - \frac{e^2}{4\varepsilon\varepsilon_0 \pi r} - eFr\cos\theta \tag{2.13}$$

where θ is the angle between $\vec{F}$ and $\vec{r}$. The maximum potential barrier is then found to be $\phi_0 - \beta_{PF}(F\cos\theta)^{1/2}$ at $r_m = \left(4\pi\varepsilon_0\varepsilon F\cos\theta/e\right)^{-1/2}$ where β_{PF} has been expressed in equation (2.9). By integrating over θ in the forward hemisphere ($0 \le \theta \le \pi/2$) the emission probability is expressed by

$$\frac{P(F)}{P(0)} = \left[1 + (\alpha - 1)\exp(\alpha)\right]/\alpha^2 + \tfrac{1}{2} \tag{2.14}$$

where $\alpha = \beta_{PF}\sqrt{F}/kT$. The relation between emission and conductivity is expressed as $\sigma = \overline{A}[P(F)]^{1/m}$ where m is a value between 1 and 2 and $\overline{A}$ is a constant.

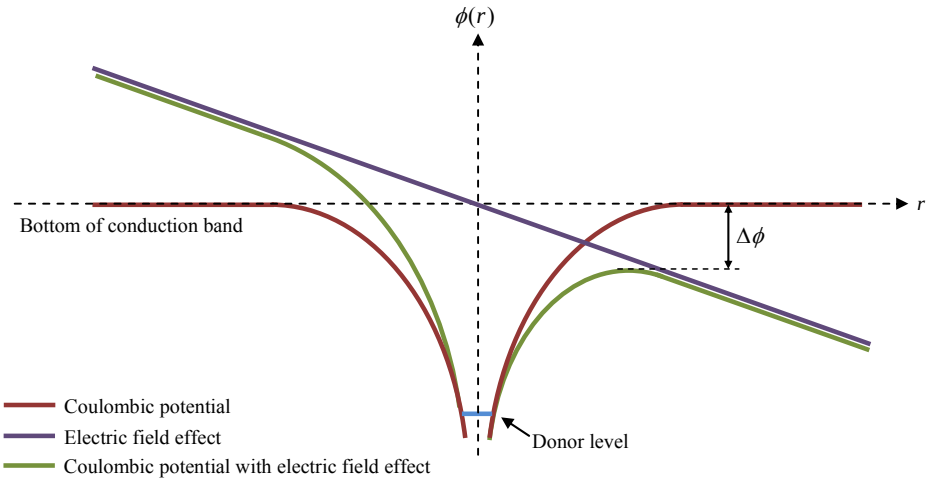

Figure 2.9 Illustrative representation of the electron potential energy due to Coulombic potential and electric field. The amount of field lowering, $\Delta\phi = \beta_{PF}F^{1/2}$.

2.6 Alternating-current conduction

The conductivity of materials may alter in response to an alternating external electric field. The alternating current (AC) conductivity is basically composed of real and imaginary parts:

$$\sigma = \sigma' + i\sigma'' \tag{2.15}$$

The real part is related to the resistive property of a material while the imaginary part corresponds to the capacitive property. In this section, the frequency response of the real part and the related theories are presented. For the sake of brevity the real part of complex AC conductivity is simply called AC conductivity and shown by σ_{AC}.

The AC conductivity in crystalline systems is typically frequency-independent up to about 1 THz, and at frequencies higher than 1 THz it follows the relation [38]:

$$\sigma_{AC}(\omega) = \frac{Ne^2}{m}\frac{\tau}{1+\omega^2\tau^2} \tag{2.16}$$

where N is the concentration of charge carriers, e is the charge of an electron, m is the effective mass, τ is the relaxation time and $\omega = 2\pi f$ where f is frequency. Crystalline systems generally have band-conduction process and the free carriers in the bands have very short relaxation time around 10^{-13} s. Hence, the contribution of free carriers in AC conduction does not depend on frequency at $\omega << 10^{13}$.

However, in disorder systems with lack of band-type conduction, the AC conductivity is frequency-dependent, universally observed to follow the power-law equation [39]:

$$\sigma_{ac}(\omega, T) = a(T)\omega^{s(\omega,T)} \tag{2.17}$$

where a is a temperature-dependent coefficient and $0 < s < 1$ is a temperature-dependent exponent. The power-law frequency-dependence is mostly observed in the frequency range from ~ 1 Hz to 10 GHz where the quantum and phonon effects

become dominant [40]. This behaviour is a characteristic phenomenon observed mainly in systems with highly disordered, amorphous or glassy structures. The universal power-law could be theoretically ascribed to relaxation caused by motion of charge carriers between localised states via either hopping or quantum tunnelling process. In fact, the frequency-dependence of the conductivity is referred to distribution of relaxation time rather than a single value, which can be well explained by hopping or tunnelling phenomenon. Accordingly, two main possible microscopic charge transport mechanisms could be defined for power-law frequency-dependence [41]:

(I) Classical hopping of carriers between pair of sites over potential barrier separating them, known as correlated barrier hopping (CBH).

(II) Phonon-assisted quantum-mechanical tunnelling (QMT) of carriers through a barrier separating two sites with distance of R.

Although both of these mechanisms follow the power-law frequency-dependence, equation (2.17), the temperature- and frequency-dependence of the exponent $s(\omega,T)$ in the CBH differs from that of the QMT and this point makes them distinguishable.

2.6.1 Correlated barrier hopping

In the CBH model, the relaxation is considered to be by hopping of charges between localised states. In this mechanism, the hopping barrier potential is correlated to the distance separating two sites, *R*, by considering the Coulombic interaction between them. The Coulombic potential reduces the barrier height [41]:

$$W = W_m - \frac{e^2}{\pi\varepsilon\varepsilon_0 R} \tag{2.18}$$

where W is the reduced barrier high, W_m is the maximum barrier high (the energy required to remove the electron from a site completely) and ε is the optical dielectric

constant of the material. Figure 2.10 shows the illustration of the lowering of the hopping barrier height for two neighbouring sites. The most probable hopping distance can be found at a frequency where $\omega\tau = 1$ and is expressed by [41]

$$R_{\omega} = \frac{e^2}{\pi\varepsilon\varepsilon_0\left(W_m + kT\ln(\omega\tau_0)\right)} \tag{2.19}$$

where τ_0 is the inverse of the optic phonon frequency mainly considered to be 10^{-13} s. This value represents the most probable hopping distance which a single carrier jumps at the frequency of ω. Equation (2.19) predicts that by increasing the frequency the R_{ω} decreases, although it is negligible if $W_m >> kT\ln(\omega\tau_0)$. The AC conductivity in the CBH model in the case of materials with narrow band is approximately given by [41]

$$\sigma_{AC} = \frac{\pi^3}{24} N^2 \varepsilon\ \varepsilon_0 \omega R_{\omega}^6 \tag{2.20}$$

where N is the density of states contributing to AC conductivity. According to Equation (2.20), the AC conductivity can be expressed in the form of power-law relation (as in (2.17)) where the exponent *s* is defined by

$$s(\omega,T) = 1 - \frac{6kT}{W_m + kT\ln(\omega\tau_0)} \tag{2.21}$$

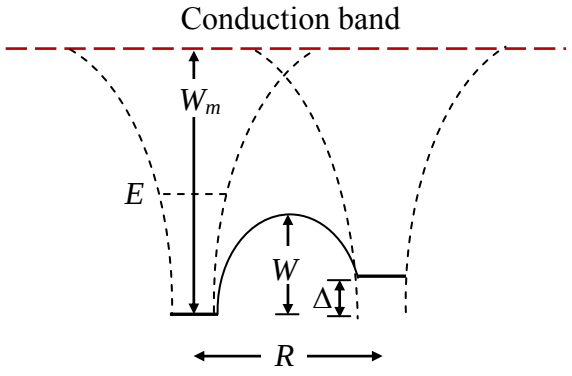

Figure 2.10 Illustration of the lowering of the hopping barrier height for two neighbouring sites in CBH model.

2.6.2 Quantum-mechanical tunnelling

In the QMT model, the charge relaxation is considered to be by direct tunnelling between two localised states. The AC conductivity in the QMT model in the simple case of single charge tunnelling between states is expressed by [41]

$$\sigma_{AC} = \frac{\pi^2}{12}\frac{e^2 kT}{\alpha} N^2(E_f)\,\omega R_\omega^4 \tag{2.22}$$

where α is the spatial extent of the localised state wavefunction, $N(E_f)$ is the density of states at the Fermi level and R_ω is the characteristic tunnelling distance at a given frequency written by

$$R_\omega = \frac{1}{2\alpha}\ln\left(\frac{1}{\omega\tau_0}\right) \tag{2.23}$$

To write the AC conduction in the power-law form in the QMT model, the exponent s is defined by

$$s_{QMT}(\omega,T) = 1 + \frac{4}{\ln(\omega\tau_0)} \tag{2.24}$$

As evident from the equation, the exponent *s* is not temperature-dependent in this model. This fact is basically used to distinguish between which of the CBH and the QMT models is followed by the experimental results.

CHAPTER 3

Literature Review

3.1 Introduction to Phthalocyanines

Phthalocyanines (Pcs) are organic components containing nitrogen, hydrogen and carbon atoms. For a long time, they have been used as pigments in inks and colouring for texture and plastics [42], however by the discovery of their semiconducting behaviour [43], they have intensively been studied for applications in organic electronic and optoelectronic devices such as solar cells, light emitting diodes, field effect transistors and gas sensors [44, 45, 46].

Phthalocyanines are well-known for their thermal and chemical stability. Strong acids or strong bases usually do not have effects on Pcs [45]. They are thermally stable (up to 673 K [47]), and can be sublimed without decomposition [48]. This feature makes phthalocyanines suitable for thin film deposition by evaporation techniques. However, considerable efforts have been made to synthesise soluble phthalocyanines applicable for solution-processed deposition techniques [49]. The remarkable feature of Pcs is their versatility; the physical, electrical and optical properties of Pcs can be tailored by replacement of their central atoms with more

than 70 different metal ions and also incorporation of variety of substituents to the molecules [44].

3.1.1 Chemical structure

A phthalocyanine is a two-dimensional planar macrocycle compound consisting of four isoindole units which are offering an 18 π-electron aromatic cloud delocalised over a Pc ring. Generally, they can be categorised into two main groups: metal-free phthalocyanine (H_2Pc) and metallophthalocyanine (MPc). In a metallophthalocyanine, the central atom is a metallic atom such as zinc, cobalt, iron and lead whilst in a metal-free phthalocyanine, hydrogen is accommodated in the centre. Typical structures of metal-free phthalocyanine and metallophthalocyanine are depicted in Figure 3.1. Phthalocyanine compounds have typically disk-like shape and can easily stack through π–π interaction between neighbouring molecules and form one-dimensional rod-like assemblies. However, the geometric shape of Pc ring may be altered in the case of large central metal ions such as Pb or Sn; in lead phthalocyanine (PbPc) or tin phthalocyanine (SnPc), the central metal is too big to be accommodated completely in the cavity of Pc ring and thus lies above it and creates a shuttlecock shape as illustrated in Figure 3.2 [50].

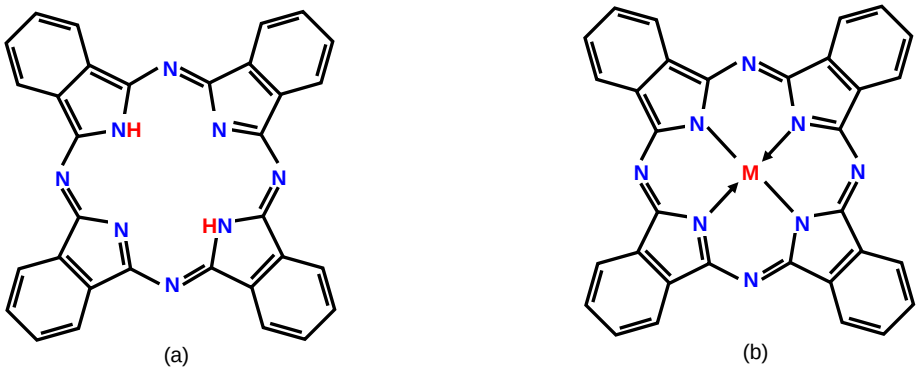

Figure 3.1 Typical structures of unsubstituted phthalocyanines, (a) metal-free phthalocyanine, (b) metallophthalocyanine (M stands for metal ion).

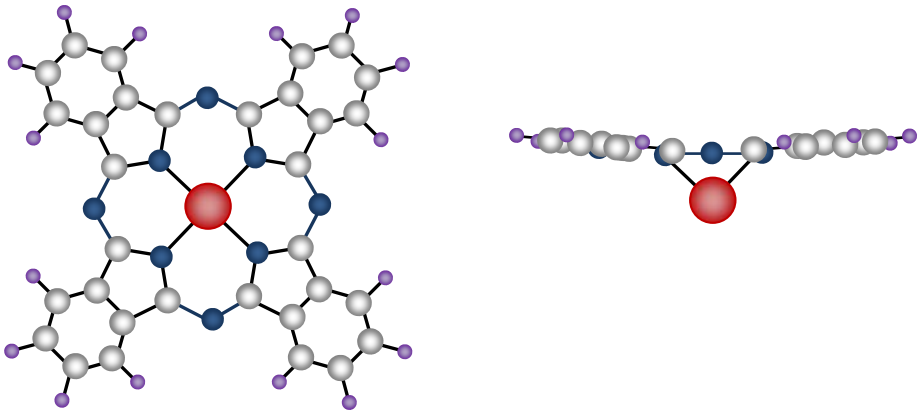

Figure 3.2 Shuttlecock shape of metalophthalocyanines with large central atom such as Pb.

3.1.2 Derivatives

The surrounding hydrogen atoms in the isoindole rings of a Pc molecule can be replaced with different organic or inorganic groups. The ring numbering of a Pc molecule is shown in Figure 3.3. The derivatives of Pcs are typically named initiating with the position of the substituent on the ring and then type of the substituent groups; for instance, 1,4,8,11,15,18,22,25 octa-alkyl-phthalocyanine is referred to a metal-free phthalocyanine substituted by eight alkyl groups sited on 1,4,8,11,15,18,22,25 positions [51]. If all substituent chains are identical and occupying similar positions in each isoindole, it is called identically substituted phthalocyanine (see Figure 3.4(a)); otherwise, it is known as non-identically substituted phthalocyanine (see Figure 3.4(b)). Figure 3.5 shows the diagrammatic representation of this classification. Some of the common substituent groups are alkyl, alkoxy or alkoxymethyl groups [52, 51].

Incorporation of substituents has significant impacts on the physical and electrical properties of phthalocyanine compounds. For instance, the molecular orientation of Pcs is significantly affected by the substituents altering their molecule-molecule

interactions and thus their crystal structure [53]. Such a structural change has a direct effect on the electrical conduction of Pcs. In addition, the solubility of Pcs in organic solvents can be improved by attaching substituents, making them suitable for low-cost solution-processed deposition techniques [49].

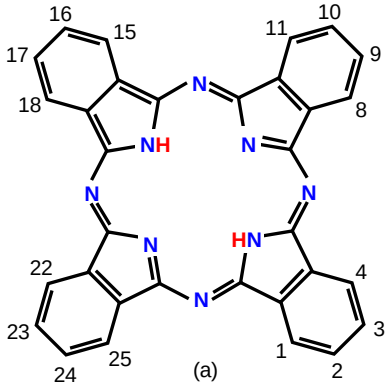

Figure 3.3 Ring numbering of a Pc molecule.

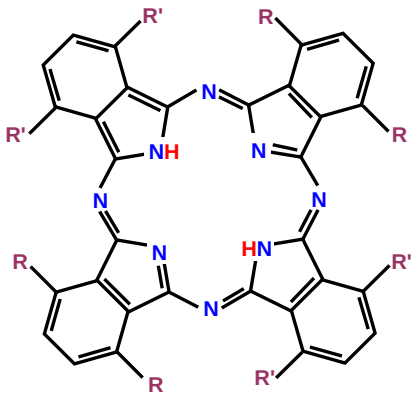

Figure 3.4 Example of chemical structures of substituted metal-free phthalocyanines, (a) identical, (b) non-identical substituted. R and R' can be any type of substituent groups such as alkyl, alkoxy or alkoxymethyl.

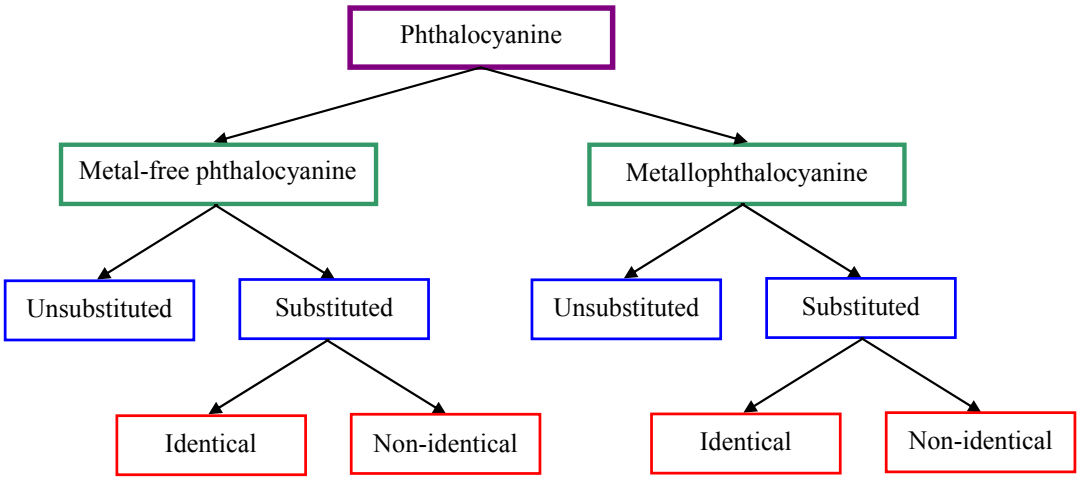

Figure 3.5 A diagrammatic representation of phthalocyanine categorisation.

3.1.3 Electrical properties and applications

The semiconducting behaviour of Pcs was discovered in 1948 [43]. They are typically p-type semiconductors with low intrinsic carrier density owning to the relatively high band gap energy, usually in the range of ~2 eV [44]. The conductivity of Pcs typically falls in the range of 10^{-12} Scm^{-1}, although considerable efforts have been made to enhance the Pcs conductivity by controlling the films growth to improve their crystalline structure and lower the density of traps, and also by adding dopant [44]. A few number of Pcs, however, behave as intrinsic semiconductors, e.g. lutetium phthalocyanine with conductivity of 6×10^{-5} Scm^{-1} (in single crystalline structure) owning to its low band gap energy [54]. The conducting property of Pcs is arising from the π-orbitals of carbon atoms that form delocalised states within the Pcs' molecules. The overlapping between π-orbitals of neighbouring molecules, π–π interaction, in a crystal structure has a vital role in the carriers mobility. The intermolecular interaction between Pcs molecules is a weak van der Waals bond which minimises the chance of band construction within the bulk and consequently reduces the mobility of carriers.

The application of Pcs as an active semiconducting layer of organic field-effect transistors (OFET) has broadly been reported. OFETs are 3-terminal devices in which the conductivity of the channel between source and drain can be controlled by the applied gate voltage across a thin dielectric. Figure 3.6 illustrates the structure of a field-effect transistor. Different types of Pcs have been studied for OFET applications among them nickel phthalocyanine (NiPc) [55], lutetium bisphthalocyanine [56], copper phthalocyanine (CuPc) [57, 58, 59, 60] and cobalt phthalocyanine (CoPc) [59]. The range of reported field-effect mobility for Pcs-based OFET is 10^{-5} to 10 $cm^2V^{-1}s^{-1}$, that is highly dependent on the central metal ion and substituent chain [61]. This range is close to commercial inorganic amorphous silicon transistors. To the best of author's knowledge, the highest reported mobility so far is 10 $cm^2V^{-1}s^{-1}$, corresponding to titanyl phthalocyanine (TioPc)-based OFET [61]. It was suggested that the high mobility of TioPc is attributed to its ultra-close π - stacking crystal structure.

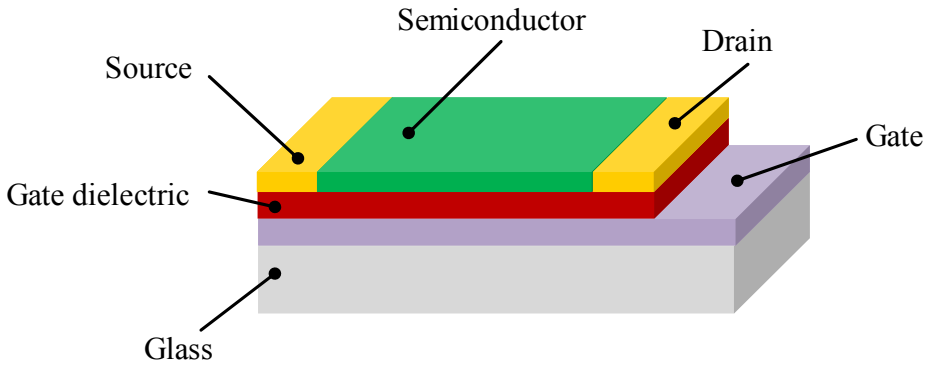

Figure 3.6 Schematic representation of an organic field-effect transistor.

3.1.4 Optical properties and applications

Phthalocyanines have been utilised as pigment since long time ago [42]. The intense colour of Pcs is arising from their strong absorption in the visible region [46]. Phthalocyanine compounds have strong photon absorption, typically with two main absorption peaks: Q-band (600-800 nm) and soret band (300-400 nm) [53]. Depending on the central metal ions and the type of substituents, the absorption peaks are shifted to either lower or higher energy and the Q-band may split [44, 46]. For instance, comparing to metal-free phthalocyanine with Q-band at about 665 nm [62], lithium phthalocyanine, magnesium phthalocyanine, lead phthalocyanine and zinc phthalocyanine show red-shift Q-bands around 670 nm, while iron phthalocyanine, cobalt phthalocyanine and ruthenium phthalocyanine exhibit blue-shift Q-band between 630 and 650 nm [44, 46]. The red-shifted Q-band observed in phthalocyanines substituted with alkoxy group is an example of substituent effects on absorption characteristic of Pcs [62].

The high absorption coefficient of Pcs ($>10^5$ [23]) as well as their wide and tuneable absorbing region makes them favourable for optoelectronic devices. One of the growing applications of Pcs is in organic photovoltaic devices (solar cells) [44, 46]. Solar cells are based on high-tech approach to convert sunlight energy to electricity. The maximum solar photon flux occurs at around 700 nm. So the most efficient light harvesting can be achieved by devices based on materials absorbing around this region. Phthalocyanine compounds with ultraviolet/blue and red/near infrared absorption feature are among the best candidates for efficient photon harvesting. Figure 3.7 shows the mismatch between the terrestrial solar spectrum and the absorption spectrum of some organic semiconductors compared with

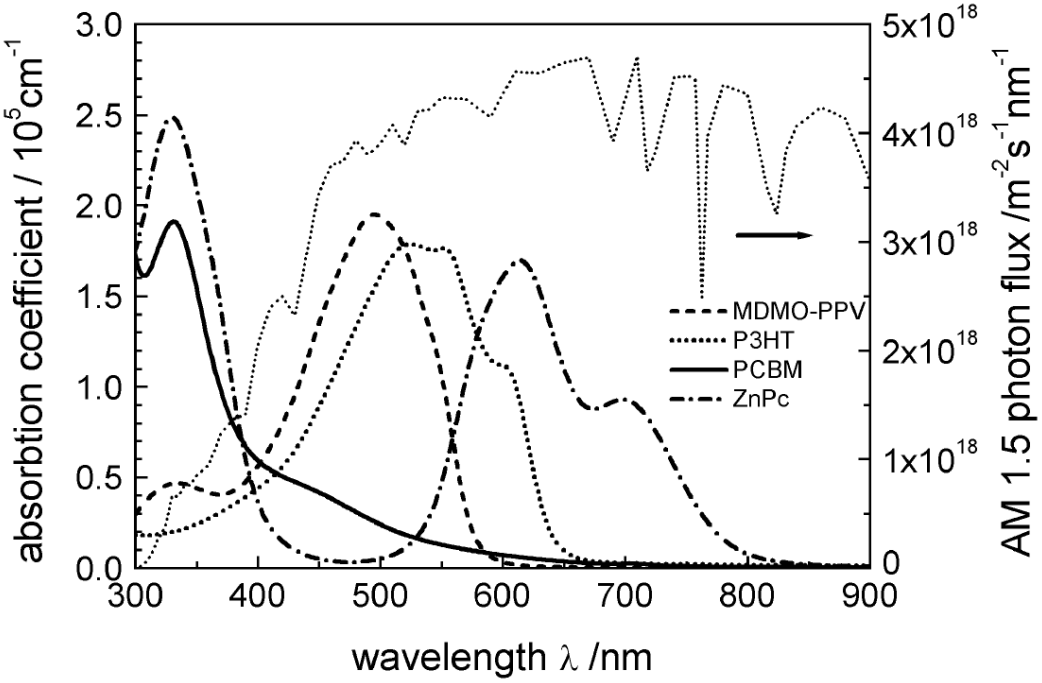

Figure 3.7 Absorption coefficient of widely used materials compared to the standard AM 1.5 terrestrial solar spectrum. It shows that the absorption peak of phthalocyanine coincides with the maximum region of photon flux, taken from [23].

phthalocyanines, taken from [23]. This ability along with excellent stability and semiconducting behaviour of Pcs put them among the most intensively studied photoactive layers for organic solar cells [44].

Solar cell devices typically have bilayer structures, one act as donor and the other as acceptor [63]. In these devices, excitons (electron-hole pairs) are first generated by absorbing photons at the photoactive layer and then dissociated to holes and electrons at the interface of phases. The mismatch between the energy levels of the donor and acceptor results in a build-in electrical potential at their interface which assists to break the excitons and generates free carriers, as illustrated in Figure 3.8. The generated carriers (holes and electrons) then move towards the corresponding electrodes. Phthalocyanine compounds are typically used as an electron donor

blending together with an acceptor such as fullerenes, in solar cells [64, 65, 66, 44]. The efficiency of up to %5 has been reported for heterostructure solar cell devices based on CuPc (donor) and C_{60} fullerenes (acceptor) [67, 68]. Terao *et al.* investigated the efficiency of organic solar cells based on Pcs/C_{60} fullerenes and shows the devices efficiency follows the sequence of CuPc > ZnPc > H_2Pc > NiPc > CoPc > FePc [69].

It is worth noting that although organic solar cells have advantages of light weight, flexibility and low-cost fabrication, but their efficiency (< %5) is still lower than that of conventional silicon solar cells (%10-%20), mainly due to low mobility of organic compounds [23].

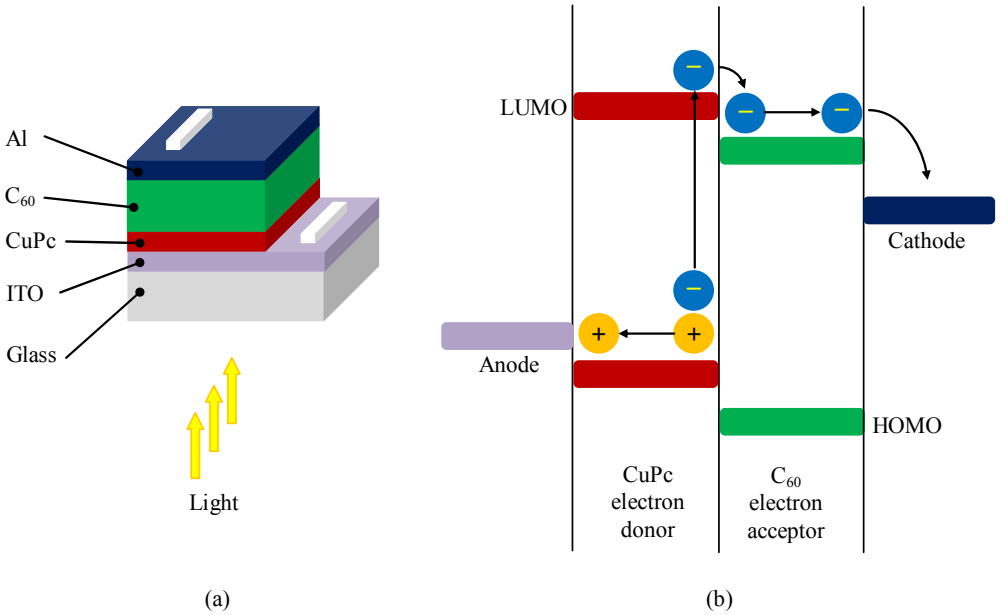

Figure 3.8 (a) schematic representation of a bilayer structure organic solar cell; (b) band diagram of a bilayer structure organic solar cell. The created excitons are dissociated at the interface between the electron donor and acceptor.

3.1.5 Gas sensitivity

Some types of phthalocyanine molecules have exhibited sensitivity to ambient gases such as nitrogen and hydrogen and have thereby a potential application for gas detector devices [45]. The almost partial oxidisation/reduction of Pcs molecules by absorbing the specific gas results in the variation of Pcs' resistance [70]. Phthalocyanines have shown sensitivity to gases such as NO_x [71], HCL [71] and NH_3 [72], whereas no sensitivity has been observed for CO, CO_2, CH_4, C_6H_{14}, C_7H_8, SO_2 and H_2S [72]. The sensitivity of Pcs is strongly affected by the nature of the central metal ion and also crystal structure [72]. Nieuwenhiuzen *et al.* reported the sensitivity to detect NO_x depends on the central metal ions which is in the sequence of NiPc < MgPc < FePc < H_2Pc < PbPc < CuPc < CoPc, while the sequence is MgPc < NiPc < CuPc < FePc << PbPc for the sensitivity to NH_3 detection [72].

3.1.6 Bistable electrical behaviour

There are some reports regarding the bistable electrical behaviour of Pcs sandwiched between two electrodes. The bistable behaviour is a fundamental requirement in memory devices. In such devices, there are two different conduction states based on the magnitude of the applied field, i.e. the conductivity suddenly increases by a few orders of magnitude at the specific amount of field. This switching behaviour can be either reversible or irreversible. The active layer of Pc-based memory devices is usually made of Pcs in contact with other moieties such as Rose Bangle [73]. However, recently the bistable behaviour of sandwich structure devices using a single layer of Pcs has also been reported [74].

3.1.7 Frequency response

Another important characteristic mainly observed in Pcs is the frequency-dependent conductivity in response to external alternating electric fields. Phthalocyanine compounds generally exhibit the universal power-law frequency response, $\sigma_{AC} \propto \omega^s$, in which the AC conductivity increases by increasing frequency [75, 50]. This behaviour specifies that the charge transport in Pcs is dominantly based on localised carriers rather than free-band carriers. In crystalline films, the power-law dependence is mainly reported at low temperatures and high frequencies [76]. The typical value of exponent *s* is below unity, although the higher values are also reported, especially at high frequencies [75]. Among the theoretical models proposed to describe this phenomenon, the CBH model is well-fitted to the Pcs' results indicating that the hopping of charge carriers between neighbouring Pcs molecules is responsible for AC conduction rather than direct tunnelling [75].

3.2 The importance of lead sulphide quantum dots

Lead sulphide (PbS) is an IV-VI semiconductor with band gap of 0.41 eV and exciton Bohr radius of 18 nm [77]. This inorganic component has a rock-salt cubic structure and is one of the important compounds of lead known as galena. It was usually used as black pigment, but currently it is mostly employed as an infrared-active semiconductor for optoelectronic device applications.

By emerging the field of nanotechnology, PbS QDs have attracted the attention due to their strong confinement effect. The large exciton Bohr radius of PbS makes it an excellent candidate for studying the quantum confinement effect as it is relatively easy to make PbS particles smaller than 18 nm. It is practically difficult to reach to

QD size in semiconductors with low exciton Bohr radius, such as CdSe with exciton Bohr radius of 4 nm [78] and CdS with exciton Bohr radius of 5.8 nm [79]. Besides, most II-VI and III-V semiconductors have large hole masses and the strong quantum confinement cannot be easily achieved for holes [80]. For example, InSb has an exciton Bohr radius of 54 nm, but the Bohr radius of hole is only 2 nm inhibiting the strong confinement of holes.

The bulk PbS has a small band gap and optically applicable in near infrared region (around 3500 nm), but strong quantum confinement in PbS QDs allows to tune the band gap energy and thus their applications in a wide spectral region from infrared to visible [81, 82, 83, 84]. In fact, by increasing the size of PbS QDs from about 4 nm to near 20 nm, the energy gap decreases from about 2 to 0.41 eV in PbS, leading to adjust the optical properties of PbS QDs for different applications in the corresponding region. Figure 3.9 presents a diagram that shows the active frequency region for different applications [81].

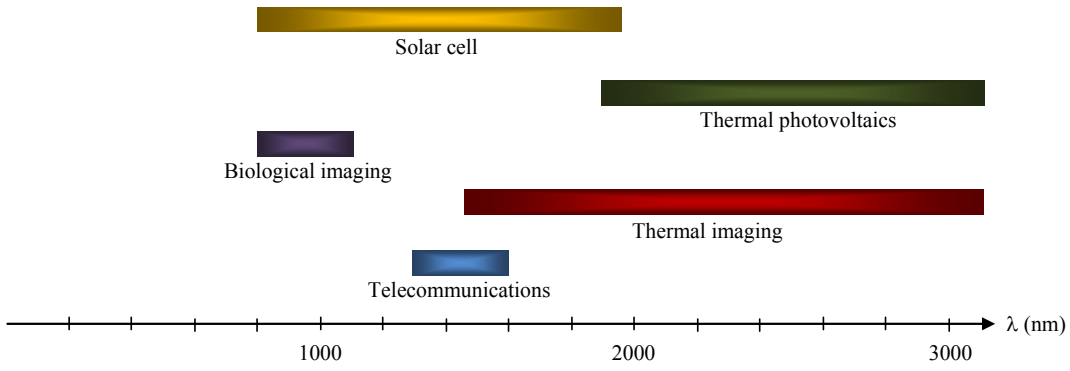

Figure 3.9 Illustration of active frequency region for various applications.

PbS QDs have also demonstrated multiple-exciton generation, in which more than one exciton is generated per each absorbed photon. Typically when a photon with energy higher than the band gap energy hits a bulk, a part of its energy is used to excite an electron and the rest is dissipated by another form of energy such as heat. But in nanoscale size, the light with energy more than twice of the band gap can generate two excitons, and so on [81]. Moreover, the long lifetime of exciton, about 1 μs, has been observed in PbS QDs [85]. Comparing to other quantum dots, such as CdSe with exciton lifetime about 10 ns, the lifetime of excited states in PbS QDs is long enough to allow the excited states to be swapped to the interface and dissociate there before recombination. These phenomena directly enhance the efficiency of photovoltaic devices [86].

Optical nonlinearity is another important property of lead sulphide, and is stronger in PbS QDs by several orders of magnitude compared to the bulk PbS due to the strong confinement effects [87]. In comparison with other semiconductors, the third-order nonlinear optical response of PbS nanocrystals is expected to be 1000 times higher than that of CdSe and 30 times higher than that of GaAs [80]. Materials with third-order nonlinear optical behaviour are applicable in telecommunication and fast optical switching devices. PbS QDs with a superior nonlinear optical ability is among the candidates for such devices as it has intensively been reported in the literature [88, 89, 87]. The nonlinear optical property of QDs is highly affected by their surface condition which can be tailored by a combination of QDs and different matrices [90].

Due to the confinement effect in PbS QDs, their HOMO and LUMO energy levels are shifted to respectively higher and lower energy. The shifted energy levels of PbS QDs typically form a desirable mismatch with the energy levels of p-type organic

matrices and improve the efficiency of the devices. For instance, the high efficiency of a photoconductor is achieved when the generated holes move toward p-type matrix, i.e. the HOMO level of the matrix is favourable for holes, and the generated electrons go to QDs, i.e. the LUMO level of PbS is preferable for electrons. The PbS QDs is appropriate choice for combination with organic matrices due to higher HOMO level (> 4.96 eV) compared to that of p-type organic matrices (mainly around 5 eV) [81].

In order to incorporate QDs for device applications, they should be normally stabilised in an appropriate matrix. So the main applications of PbS QDs have been summarised in the nanocomposite section.

3.3 Nanocomposites

Nanocomposites are multiphase solid materials with at least one component in the range of nanoscale. The components can be crystalline, polycrystalline or amorphous with the nature of organic and/or inorganic [91]. Combining various kinds of components provides a way to tailor new materials with specific properties and applications. Not only the components are important in the final property of nanocomposites, but also the inner interface between them has a significant influence on the overall performance of the materials, so new properties can also be expected from the combined phases. Among the nanocomposites, organic/inorganic nanocomposites have attracted growing interest [3]. In such nanocomposites, typically the host matrices are organic compounds and the nanoscale phases are inorganic usually as small as quantum dots. The incorporation of inorganic quantum dots with an organic matrix not only improves the optical and electrical properties of

the organic devices [3], but also enables scientists to exploit the property of QDs while getting advantages of light weight, mechanically flexible and low-cost organic devices [3]. There are unlimited sets of combined materials with specific properties. In the following sections, the common preparation routes, characterisation techniques and applications of nanocomposites are presented, with emphasis on the nanocomposites containing PbS QDs.

3.3.1 Preparation methods

The combination of nanoparticles with other materials is not as easy as mixing two components together. Nanoparticles inherently tend to aggregate/grow in order to reduce their surface energy. Therefore, the main challenge in construction of a nanocomposite is to control the surface energy of nanoscale components in order to have monodispersed particles as well as a homogeneous composite with controlled nanoparticles' size and shape. Surface energy is arising from the unsatisfied dangling bonds at the surface. The disruption of intermolecular bonds during surface creation in solid or liquid results in an excess of energy at the surface. This energy creates a force to attract other molecules from surrounding media in order to compensate the disrupted bonds. The high volume/surface ratio in low dimensional systems, e.g. nanoparticles, yields a significant increase in the amount of surface energy and causes them to aggregate and continue growing to a bulk size.

Numerous precursors and stabilising matrices with different preparation methods have been used to constitute PbS nanocomposites as some of them are presented below.

3.3.1.1 Solid state method

Chemical solid state methods are well-known synthetic routes in which the PbS nanoparticles grow inside a solid matrix via a chemical reaction between Pb^{++} ion and sulphur precursors (very often H_2S gas). Typically the rigid environment of solid matrices acts as size limiter and prevents nanoparticles from aggregation. Different kinds of solid media, organic and inorganic, have been used as a host matrix for PbS nanoparticles. Zeolites are among the old ones that used for the first time by Wang and Herron in 1987 [92]. The Pb^{++} ions are initially exchanged into the cages of zeolite and then exposed to H_2S gas to form PbS nanoparticles. The porous and rigid environment of zeolite restricts the aggregation of particles and leads to formation of extremely small particles ranging from 0.3 to 1.3 nm, depending on the type of zeolite and its pores size. Besides zeolites, other porous matrices such as silica [93] and alumina membrane [94] have also been used as a template to grow nanoscale PbS particles.

Polymer films are more flexible environments than zeolites and allow bigger PbS particles to grow [95]. One of the possible precursors in this group is ionomer with Pb^{++} ions [77, 96, 97]. The ionic groups in ionomer molecules can join together and form ionic domains as small as a few nanometres in size and are phase separated from the polymer matrix. Having exposed the ionomer to H_2S gas, PbS clusters are formed inside the ionic domains and consequently a PbS/polymer nanocomposite is constructed, which can be either in the form of a film [77] or a solution [96]. By subsequent heat treatment, it is possible to produce larger particles as heating mobilises the particles and causes more agglomeration.

Formation of nanoparticles in a Langmuir-Blodgett (LB) film of fatty acids has also

attracted interests [98, 99, 100, 101]. The NPs are well restricted by special structure of LB films. An LB film consists of alternated stacking of hydrophilic and hydrophobic layers as depicted in Figure 3.10. When the hydrophilic head group has a metal ion-binding ability, the highly ordered head groups restrict the amount and arrangement of metal ions precursor, providing a condition to construct size-confined particles. Moreover, the hydrophobic organic layers lie between hydrophilic layers and prevent trans-layer reactions.

The nanocomposite with an LB film structure has first been reported in 1986 contained cadmium sulphide (CdS) nanoparticles and then developed for other nanoparticles [102]. The PbS nanocomposite has been constructed by exposing a mono or multilayer LB film of fatty acid salt (contain Pb^{++}) to H_2S gas to form PbS nanoparticles between layers of corresponding LB fatty acid [101].

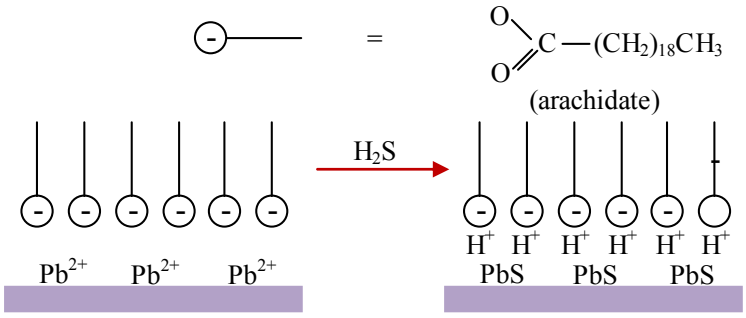

(a) Monolayer preparation

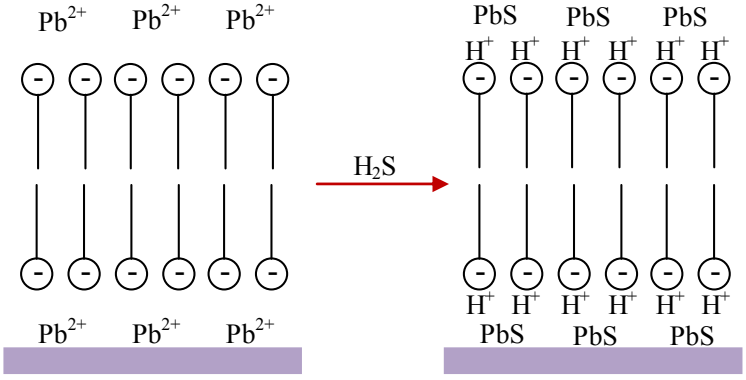

(b) Multilayer preparation

Figure 3.10 LB film: schematic formation of PbS NPs in (a) monolayer and (b) multilayer of fatty acid LB film by exposure of Pb-arachidate LB film to H_2S gas.

3.3.1.2 Wet-chemical method

Wet-chemical colloidal methods are also common routes to synthesise nanocomposites. In this approach, a reaction between a lead precursor (usually a lead salt such as lead acetate [103]) and a sulphur precursor (e.g. H_2S [103]) takes place in a solution in the presence of suitable capping agents and/or stabilisers. Comparing to the solid state methods in which nanocomposites are constructed by growing nanoparticles inside a solid media, in wet-chemical methods a solution consisting of nanoparticles and a matrix is first prepared and then transformed to a solid nanocomposite film by any kinds of film deposition techniques, as graphically illustrated in Figure 3.11. Various PbS nanocomposites have been synthesised so far using this method [103, 104, 105, 80, 106, 107, 108]. The high surface energy of nanoparticles is a critical issue in colloidal methods and needs to be controlled to yield a homogeneous nanocomposite with monodispersed particles. Hence, the methods usually involve capping the nanoparticles surface with surfactant agents and stabilisers to reduce the surface energy of particles. One of the common capping agents for PbS nanoparticles are organic ligands [105, 80, 109]. Organic ligands are normally hydrocarbon chains terminated by a functional group such as oleic acid [105, 80], octadecylamine [109], dodecylamine [109] and octylamine [109]. The organically capped PbS nanocrystals are soluble in organic solvent and can be mixed with any polymer solution to produce polymer/PbS nanocomposites such as poly (2-methoxy-5-(2'-ethyl-hexyloxy)-p-phenylene vinylene) (MEH-PPV)/PbS [110, 109]. Figure 3.12 represents the schematic representation of the organically capped-PbS nanocrystals. The size of particles was controlled by (a) capping ligand concentration, (b) injection temperature and injection time, and (c) the growth temperature and growth time. The capping ligands and their length have the main

role in the interface property of PbS NPs and host matrices that directly influence the electroluminescence and photovoltaic properties of nanocomposites.

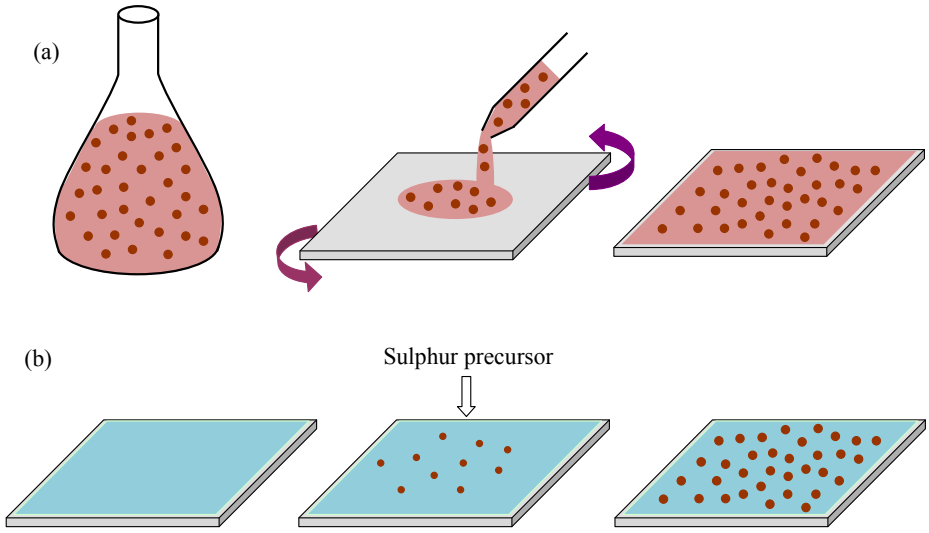

Figure 3.11 Illustrative representation of nanocomposite preparation routes (a) wet-chemical method (b) solid state method.

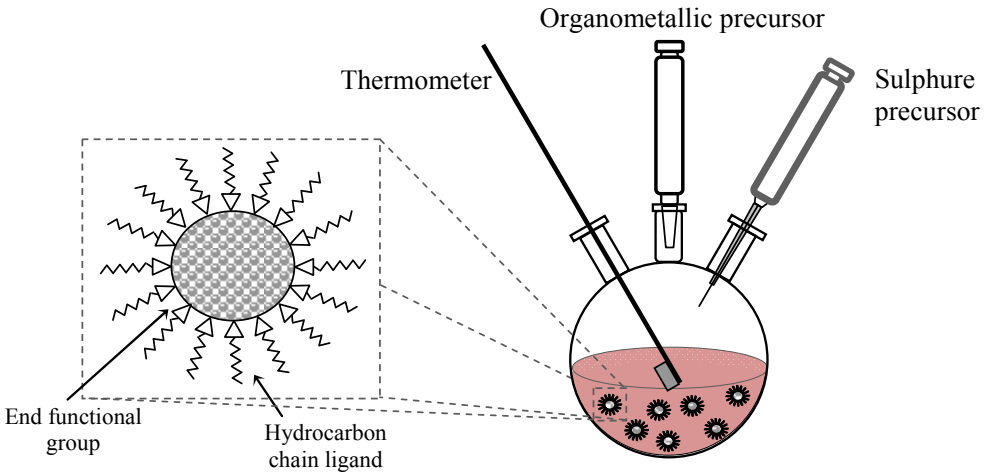

Figure 3.12 Schematic representation of the organometallic synthetic procedure of PbS nanoparticles. The nanoparticles are capped with ligands consisting of a hydrocarbon chain and an end functional group dispersed in organic solvent.

Due to the high impacts of surfactant agents on the properties of nanocomposites, a series of efforts has been made to avoid such an insulating layer in synthetic methods. Watt *et al*. proposed a simple approach to synthesise MEH-PPV/PbS nanocomposites in which MEH-PPV could itself reduce the surface energy of nanoparticles and act as the size-limiting reagent, therefore no further capping agent is required [106]. This colloidal method was carried out by injecting a sulphur precursor into a heated MEH-PPV solution containing a lead reactant. Since that time, several PbS nanocomposites have been made by this method, using different polymers including polystyrene, polyethylene, poly(1-butene) and poly(1-decene) [90, 107].

One of the widely-used chemical solution methods to synthesise nanocomposites is sol-gel. This technique is favourable as it is performed at lower temperatures than conventional chemical methods and can offer homogeneous distribution of nanoparticles. This process is based on different approaches. One approach is to mix the independent solution of matrix and constructed PbS nanoparticles together to produce a sol and then convert it to homogeneous gel by heat treatment [104]. PbS nanocrystals embedded in amorphous zirconia has been synthesised by another approach in which a sol containing all the precursors for matrix (zirconia) and PbS nanoparticle was prepared and then the nanoparticles are formed during the gel process followed by heat treatment [111]. The method was extended later by adding two other sol solutions to the previous sol solution to synthesise PbS nanoparticles in zirconia-silica-urethane matrix [112]. The amorphous nanocomposites made by sol-gel methods can be easily shaped as films or bulk.

3.3.1.3 Gaseous deposition method

Gaseous deposition is another technique to synthesise PbS nanocrystals in an organic matrix [107]. In the gaseous deposition technique, the lead vapour is produced by magnetron sputtering of a metallic lead target and then reacted with H_2S gas to form lead sulphide vapour. After that the vapour passes through a water-cooled aggregation zone, leading to PbS cluster formation and subsequent deposition on the substrate where the vapour of organic oligomer, such as sexithiophene (6T), (as a matrix) is simultaneously depositing. The illustrative representation of the procedure of this method is presented in Figure 3.13. Some of the features of this method are (a) flexibility in selection of organic matrix, (b) controlling the size of nanoparticles by changing the rate of flowing gas or length of aggregation zone, independent of organic matrix and (c) tuning particle density without affecting their size.

Table 3.1 summarises some of the reported syntheses of PbS nanocomposites.

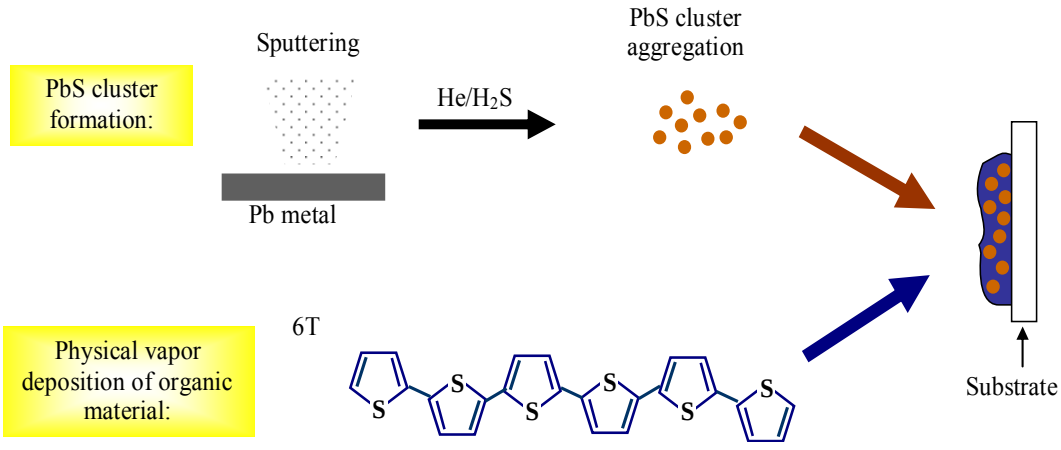

Figure 3.13 Illustrative representation of gaseous deposition route for synthesising PbS nanocomposite. PbS cluster and organic vapour are deposited on the substrate simultaneously.

Table 3.1 Summary of some of the reported syntheses of PbS nanocomposites.

Ref	Year	Name of matrix	Synthesis method	Particle size	Characterisation technique
[92]	1987	Zeolite	Solid state	0.3-1.3 nm	Reflectance spectroscopy
[77]	1987	E-MAA[7] polymer	Solid state	Varying from 1.3 nm to bulk size	UV-Vis XRD
[103]	1994	PEO[13] polymer	Colloidal solution	4-80 nm	XRD TEM
[101]	1995	Stearic acid (fatty acid)	Solid state (LB film)	Variable	UV-Vis XPS
[104]	1997	Silica gel	Colloidal solution	2.6-4 nm	UV-Vis
[113]	1999	Zirconia-ormosil[6]	Colloidal solution (sol-gel)	Variable with average of 4.8 nm	UV-Vis XRD TEM
[96]	1999	p(MMA-co-MAA) polymer	Solid state and Colloidal solution	1-10 nm	UV-Vis XRD TEM
[114]	2000	Ormocer[5]	Solid state (Ormocer with sol-gel)	11-14 nm	UV-Vis XRD TEM
[108]	2000	PVA[1] polymer PVP[2] polymer PS[9] polymer PMMA[4] polymer	Colloidal solution	4-12 nm	UV-Vis XRD TEM
[115]	2002	11-Mercaptoundecanoic acid	Solid state (SAM[3] film)	3.2 ± 0.4 nm	XPS
[116]	2002	Zirconia	Colloidal Solution (sol-gel)	4-9 nm	UV-Vis TEM
[112]	2003	Zirconia-Silica-Urethane	Colloidal solution (sol-gel)	4-8 nm	UV-Vis TEM
[8]	2004	Phthalocyanine	Solid state		UV-Vis XPS Raman

Ref	Year	Name of matrix	Synthesis method	Particle size	Characterisation technique
[106]	2004	MEH-PPV[8] polymer	Colloidal solution	4 nm ($\pm$ 2)	TEM SADP
[94]	2007	Alumina membrane	Solid state	-----	XRD TEM SADP Raman
[107]	2008	Sexithiophene oligomer	Gaseous deposition	~3 nm	Uv-Vis XPS TEM
[107]	2008	PS polymer	Colloidal solution	~3 nm	TEM
[90]	2008	PD[10] polymer PB[11] polymer PE[12] polymer	Colloidal solution	4.6 nm 5.6 nm 9 nm	UV-Vis TEM

[1]PVA : Poly(vinyl-alcohol)
[2]PVP : Poly(vinyl-pyrrolidone)
[3]SAM : Self-assembled monolayer
[4]PMMA : Poly(methyl-methacrylate)
[5]Ormocer : Organically modified ceramic
[6]Ormosil : Organically modified silicates
[7]E-MAA : ethylene-15% methacrylic acid copolymer
[8]MEH-PPV : poly (2-methoxy-5-(2'-ethyl-hexyloxy)-p-phenylene vinylene)
[9]PS : Polystyrene
[10]PD : Poly(1-decene)
[11]PB : Poly(1-Butene)
[12]PE : Polyethylene
[13]PEO : Poly(ethylene oxide)

3.3.2 Characterisation techniques

There are several powerful techniques utilised to characterise the nanocomposite materials. Some of these techniques serve to determine the chemical structure of components and confirm the synthesis of expected composite and some others are employed to verify the formation of nanoscale particles. There are also some techniques that can be used for both purposes. The commonly used techniques for characterisation of nanocomposite have been presented below.

3.3.2.1 Transmission electron microscopy

Transmission electron microscopy (TEM) is an imaging technique which can provide a direct image of a sample with high magnification. This technique has extensively been employed to determine the shape, dispersion and also size distribution of nanoparticles [94, 96, 108, 117, 107, 118, 103]. In high-resolution images, the lattice spacing of nanocrystals is clearly observable, and the distance between planes can be measured [119, 118, 120]. The other advantage of this technique is providing a diffraction pattern which serves information about the crystal structure of the components, and also assists to identify the components using reference database [106, 117, 118]. An example of TEM image corresponding to PbS doped SiO_2-TiO_2 film is shown in Figure 3.14 [120].

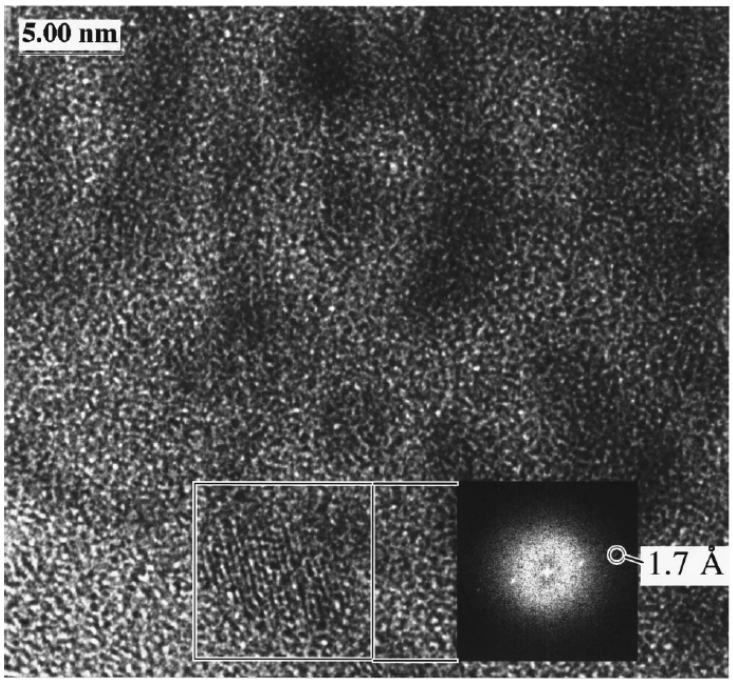

Figure 3.14 High resolution image of PbS doped SiO_2-TiO_2 film. The indicated lattice spacing in the inset corresponds to 222 crystalline plane of PbS nanoparticle taken from [120].

The most critical part of TEM technique is the preparation of specimens which should be thin enough (a few tens of nanometre thick) to be electron transparent. For solid nanocomposites, scratched fragments of the nanocomposite are typically placed (sometimes first dispersed in a solvent) on top of a very small (usually 3 mm diameter) copper-coated grid substrate [120].

3.3.2.2 X-ray diffraction

The crystal structure of nanocomposite components can be studied by X-ray diffraction (XRD). Several types of nanocomposites with PbS nanoparticles have been characterised by this technique so far [94, 77, 96, 108, 117]. Since the crystal parameters of a material are unique, this technique is frequently employed to identify the nanocomposite components. Moreover, the ability to calculate the size of nanocrystals makes the technique more attractive. The size of nanocrystal can be estimated from the line broadening of the diffraction peaks using the Scherrer equation, as will be explain later. The PbS with a cubic crystal structure has the main Bragg's peaks at 2θ equal to 26, 30, 43 and 51 degrees corresponding to 111, 200, 220 and 311 crystal planes, respectively (see Appendix 1).

3.3.2.3 Optical absorption spectroscopy

Optical absorption spectroscopy is one of the widespread characterisation techniques applied to nanocomposites. Not only it reveals the regions where the components are absorbing, but it also offers a powerful and straightforward method to observe the quantum confinement effects in QDs which is the main evidence of QDs formation. The quantum confinement effect causes an increase in the band gap energy of QDs and subsequently shifts the onset of absorption energy to a higher energy. The

observation of so-called blue-shift in the absorption spectrum of PbS QDs is commonly reported [77, 96, 98, 99, 121, 101, 108, 107]. The onset of bulk PbS absorption spectrum is about 3200 nm [77], which shifts to visible or near infrared regions in the case of PbS QDs, depending on the QDs size. The excitonic peak may be too broad or even not visible in the absorption spectra of PbS QDs due to various reasons such as broad size distribution of the QDs and/or lack of precision of thin film absorption measurement [122]. The appearance of more than one excitonic peak in PbS QDs spectrum has also been reported [123]. The optical absorption spectroscopy technique can be used to estimate the size of QDs based on the amount of increase in the band gap energy; a well-known theoretical model used for this purpose is presented in the later sections.

3.3.2.4 Raman spectroscopy

Raman spectroscopy belongs to a group of molecular vibrational spectroscopy and serves to analyse the chemical structure of molecules. The vibrational energy level of a molecule is related to its chemical bond, the Raman spectrum can therefore be used to identify components of a nanocomposite. However, the asymmetric broadening and shift of the optical phonon Raman line are expected for the nanoscale particles [124]. There are several reports of employing this technique to characterise nanocomposite components, especially identifying nanoparticles through their vibrational mode [94, 125, 8]. Although the application of Raman spectroscopy has been reported to confirm the formation of PbS nanoparticles, this technique is less attractive since the PbS is relatively weak Raman scatterer at room temperature [126].

3.3.2.5 X-ray photoelectron spectroscopy

X-ray photoelectron spectroscopy (XPS) is an experimental-based tool serves to examine the chemical compositions and electronic state of the surface of a sample. The sample is bombarded with X-rays which penetrate (a few nanometres) into the top layer of the sample and the binding energy of excited electrons is measured. Each element has a specific characteristic binding energy associated with its atomic orbital. Having the binding energies, the element used in the composite can be determined. This technique can be employed to characterise nanocomposites as widely reported in the literature [121, 101, 107, 98, 8].

3.3.3 Calculation of particle size

One of the best approaches to prove the successful formation of quantum dots in a composite is calculating the size of nanoparticles and verifying they are smaller than the exciton Bohr radius. In addition, monitoring the particle size is essential to study the effect of size reduction in nanocomposite properties, especially when they are quantum dots and subjected to the quantum confinement effect. Besides a few techniques, such as TEM, which enable scientists to measure the particle size directly through a magnified image, there are a number of techniques, e.g. UV-Vis and XRD, which serve as a probe to calculate the size of sufficiently small particles through the effect of size reduction on the output data. A number of commonly used methods to calculate the particle size have been explained below.

3.3.3.1 Effective mass approximation

One of the main methods to determine the size of a quantum dot is based on the quantum confinement effect which clearly appears by a blue-shift in the optical absorption onset. A number of models have been proposed to theoretically describe the quantum confinement effect [78, 122]. One of these models is the effective mass approximation that is commonly applied since 1981 [12]. The model is based on the combination of the effective mass assumption and particle-in-a-box solution. When the size of nanoparticles becomes lower than the exciton Bohr radius, the conduction electrons and holes cannot freely move anymore, and get confined in limited dimensions of the nanoparticles' volume. This phenomenon is similar to the well-known particle-in-a-box problem in which a particle is confined in limited dimensions of a box, and results in discrete energy levels of the system, see Appendix 2. By considering holes and electrons as two independent particles confined in a box, and also assuming that the mass of electrons and holes is reduced to an effective mass in a crystal, the first excited state of QDs can be written as [10], [12]

$$E_g^{Particle} - E_g^{bulk} = \frac{\hbar^2 \pi^2}{2R^2}\left(\frac{1}{m_e} + \frac{1}{m_h}\right) - \frac{1.8e^2}{\varepsilon R} + \text{polarisation term} \qquad (3.1)$$

where $E_g^{Particle}$ and E_g^{bulk} are band gap energy of particles and bulk respectively, m_e and m_h are electron and hole effective masses respectively, $\hbar$ is the reduced Planck constant, ε is optical dielectric constant and R is the radius of the particles. The first term in the right hand side of Equation (3.1) is the kinetic energy of the electrons and holes in the first excited state, the second term is related to the Coulomb interaction between electron-hole pair, and the third term is the polarisation energy which is generally small and negligible. In small band gap materials with high optical

dielectric constant materials (e.g. PbS), the Coulomb energy is very small and can be ignored too [10]. This model is broadly used to estimate the size of quantum dots through the amount of increase in the band gap energy of QDs [8, 98, 116, 127].

3.3.3.2 Scherrer equation

In 1918 Scherrer discovered that the size of crystallites contributes to broaden the Bragg peak in the X-ray diffraction spectrum. The well-known equation of Scherrer which expresses the relation between the size of nanoparticles and the width of the Bragg peak is [128]:

$$D = \frac{k\,l}{\beta \cos\theta} \tag{3.2}$$

where D is the diameter of nanoparticles, k is the geometric factor which is usually assumed to be 0.9, l is the X-ray wavelength (1.542 $\mathring{A}$), β denotes the half-width of the Bragg peak and θ represents the Bragg angle. β is the width of the Bragg peak at half of the maximum intensity which known as full-width at half maximum (FWHM) and usually measured in radians. Figure 3.15 illustrates how β can be calculated from the Bragg peak. Besides the size contribution, there are other defects that may contribute to the line broadening of the Bragg peak, such as microstrains within a crystal grain, but they are insignificant compared to the strong factor of size in the nanoscale particles [128]. This method has widely been used to calculate the size of particles, e.g. PbS [117, 127, 77, 103], although it may not be reliable for particles smaller than 25 $\mathring{A}$ [77]. It should be noted that the calculated size by this method may not be always in close agreement with the size recorded by TEM

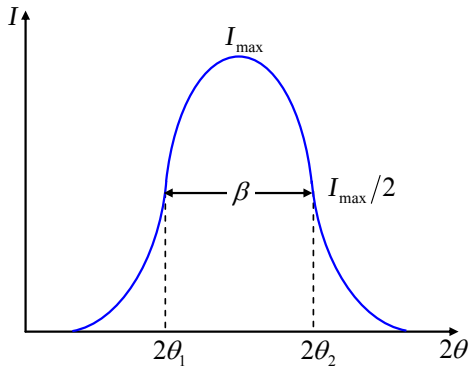

Figure 3.15 The calculation of β, full-width at half maximum, from the Bragg peak.

measurements. The reason is originated from a very broad size distribution, variation in shape or even partial amorphous structure in bigger nanoparticles [129].

3.3.4 Properties and applications

The properties of a nanocomposite depend on the constituent components and their inner interface. Some of the common optical and electrical properties and applications of organic/inorganic nanocomposites including PbS nanocomposites are discussed in the following sections.

3.3.4.1 Optoelectronic properties and applications

Organic/inorganic nanocomposites have broadly been studied for potential applications in optoelectronic devices such as photodetectors, solar cells, light emitting diodes and photodiodes [122, 81, 130]. Due to the tuneable band gap of QDs, they are able to emit and absorb light in a wide range of wavelength. In fact, the inclusion of QDs provides a route to fabricate optoelectronic devices working in wide spectral range while there is no need for changing the constituent components.

Electroluminescence: One of the main optoelectronic properties of organic/inorganic nanocomposites is electroluminescence. Electroluminescence is radiation from a system by electrical pumping, and widely observed in nanocomposites such as polyaniline/CdTe [131], polypyrrole/CdTe [132], Poly(p-phenylene vinylene)/CdSe [133], polylaurylmethacrylate/CdS(ZnS) [134] and TPB/ZnS [135]. The organic/inorganic nanocomposites with electroluminescence ability are mainly applicable in organic light-emitting diodes (OLED). An OLED device typically consists of two contact electrodes, acting as cathode and anode, in the opposite sides of an active material. By applying voltage across an OLED with a nanocomposite as an active material, electrons and holes are injected to the nanocomposite from anode and cathode, respectively. The injected charges are mainly captured inside the QDs and recombine there to generate excitons (electron-hole pairs). The generated excitons then decay radiatively to emit light. Tuning the colour of the emitted light by controlling the size of QDs is the main advantages of nanocomposites-based OLEDs, as observed for instance in polylaurylmethacrylate/CdSe by tuning colour between bluish green to red colour [134] and MEH-PPV/indium arsenide by tuning emitted wavelength between 1 to 1.3 μn [136].

Nanocomposites contained PbS quantum dots are interested due to the ability to emit light in a wide range from infrared to visible regions, depending on the size of PbS particle [137, 110]. However, the low efficiency of such devices is still a main barrier to commercialise them. An external quantum efficiency (the ratio of photons extracted to electrons injected) of 1.2% has been reported for infrared electroluminescent devices based on MEH-PPV/PbS and CN-PPP/PbS nanocomposites [110]. The external quantum efficiency in inorganic light emitting

diodes and lasers is in the range of 10% to 60% [109].

One of the important factors in electroluminescence efficiency is the mismatch between the energy levels of QDs and the matrix, i.e. the position of HOMO and LUMO levels of QDs with respect to the host matrix. Different possible energy band diagrams of nanocomposites have been presented in Figure 3.16 [122]. The optimum band diagram for efficient electroluminescence is type I (b) where QDs' band gap completely lies inside the host material. In this case, the QDs act as potential wells for both electrons and holes, and capture them to subsequently create excitons inside QDs [122]. The presence of an insulating layer, e.g. capping agent, inhibits the charge transferring from the matrix into the QDs. A study on MEV-PPV/PbS nanocomposites with different surface-capping ligands shows that the ligand with shorter chain excitons can enhance the excitation transfer efficiency by a factor of 3 [109]. The excitation transfer efficiency is defined as the number of excitons transferred to the nanoparticles divided by the total number of excitons generated in the matrix.

Photoconduction: The nanocomposites can also be used as photosensitive materials converting photon energy to electrical energy by absorbing light. Such a property is mainly applicable in solar cells, photodetectors and photodiodes. The observation of photoconductivity in a QD doped polymer, polyvinylcarbazole/CdS QDs, has first been reported by Wang and Herron in 1992 [138]. This work opened a new window for applications of photosensitive organic/inorganic nanocomposites in optoelectronic devices. Various nanocomposites-based solar cells have been studied including MEH-PPV/CdS [4], poly(2-methoxy-5-(3',7'-dimethyl-octyloxy)-p-phenylenevinylene)/CdSe [139] and poly(3-hexylthiophene)/ZnO [140], and demonstrated the devices can reach to power conversion efficiencies of up to 1.8%.

The photoconduction procedure in a solar cell has been illustratively shown in Figure 3.17. Generally the efficiency of photoconductive devices is the product of three factors:

1- Inherent ability of active materials to create excitons by absorbing photon energy.
2- Efficient dissociation of excitons to generate electron and hole carriers.
3- Presence of high mobility transporting pathway for photogenerated charges to reach the corresponding electrodes.

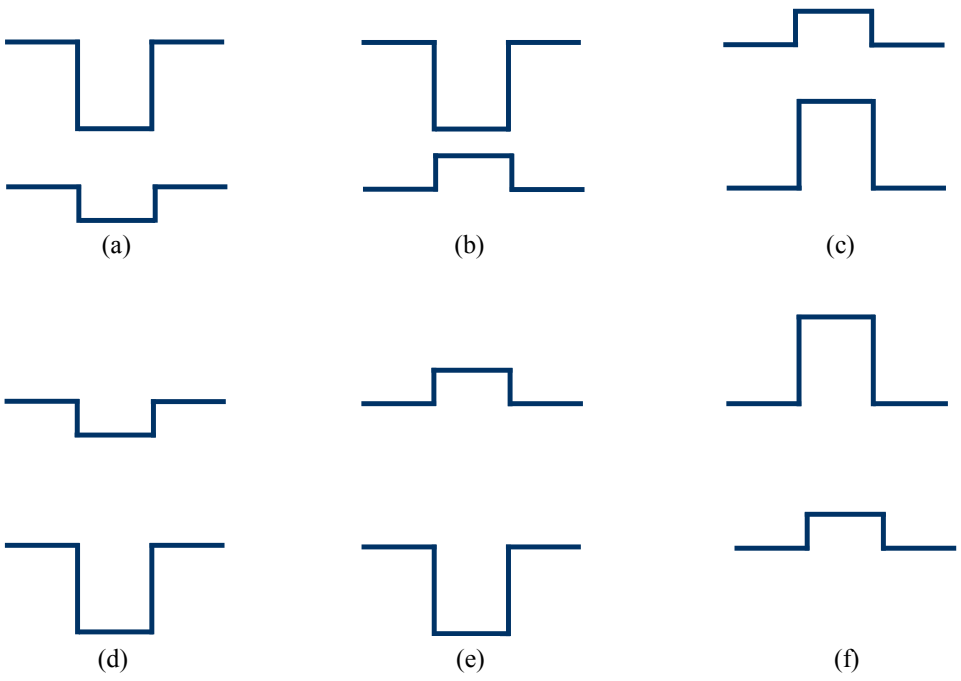

Figure 3.16 Different possible energy band diagrams of hybrid nanocomposites. (b,e) correspond to type I composites in which both energy levels (HOMO and LUMO) of one components lie inside the other one. The remaining cases (a,c,d,f) correspond to type II [122].

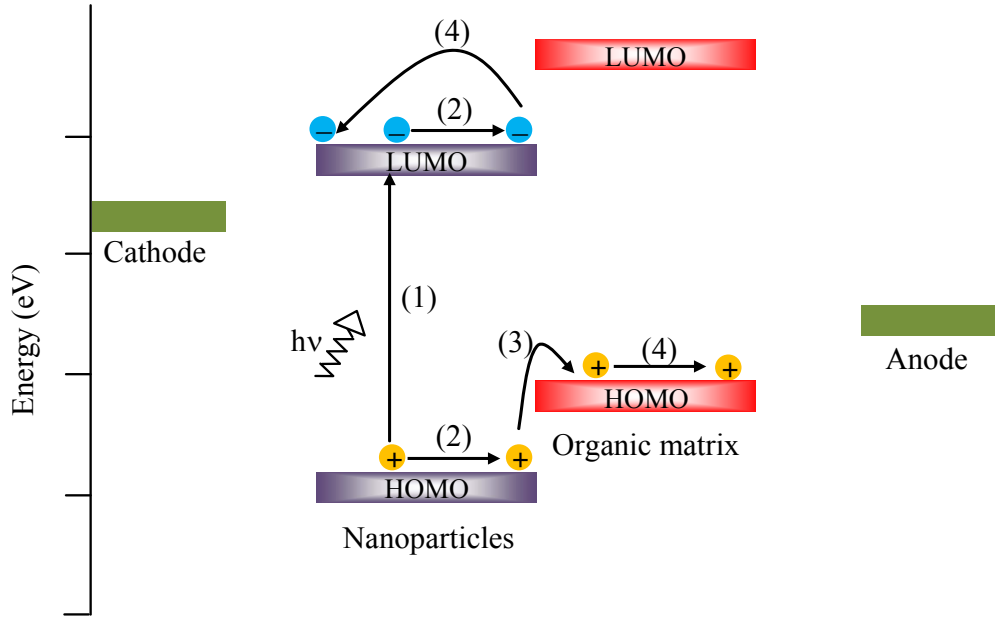

Figure 3.17 Illustration of basic processes taking place in organic/inorganic nanocomposite solar cells: (1) photogeneration of excitons in nanoparticles, (2) exciton diffusion, (3) exciton dissociated into separated charges at the interface and (4) transport of the separated charges to the opposite electrodes.

In organic/inorganic nanocomposites typically both components, i.e. nanoparticles and host matrix, are light absorbing materials. Organic compounds, such as phthalocyanines and conjugated polymers, are capable to harvest light in the visible region, but inclusion of QDs with tuneable absorbing region can enhance the light harvesting even beyond the visible region [81, 83]. Figure 3.18 shows reported photocurrent spectral responses for MEH-PPV/PbS nanocomposite that are tuneable in the infrared region by controlling the size of PbS QDs [81].

Using nanocomposites as active photoconductive materials can also increase the rate of excitons dissociation [122]. A nanocomposite has a nanoscale heterojunction structure with a large effective interfacial area between two phases, arising from the

large surface/volume ratio of nanoparticles. The separation of charges occurs at the nanoparticle-matrix interface; therefore the availability of a large interfacial area in nanocomposites increases the rate of excitons dissociation, compared to bilayer structure devices. Moreover, the diffusion length of excitons is low in organic compounds (in the range of 5-15 nm [4]) so that excitons which are generated far from the phases interface have a small chance of dissociation [141]. In a nanocomposite where nanoparticles are dispersed inside the host matrix, the distance between the generated excitons and the phases interface should not exceed more than a few nanometres.

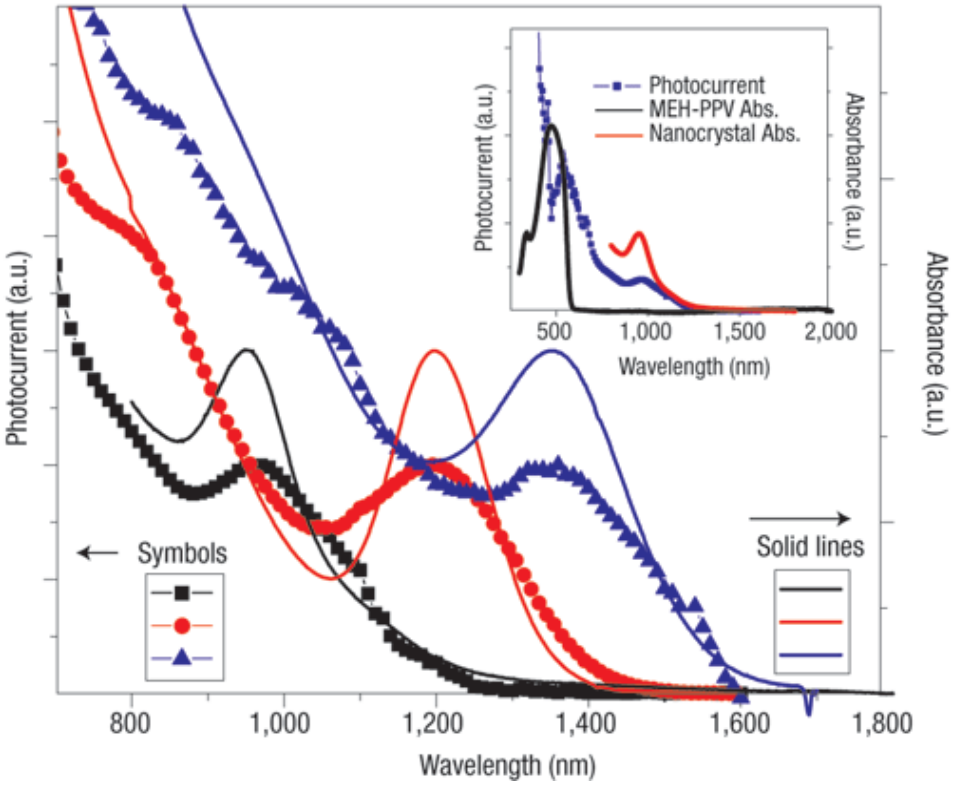

Figure 3.18 Photocurrent spectral responses and absorption spectra of MEH-PPV/PbS nanocomposite. The absorption peaks are tuned to 955(black), 1200 (red) and 1355 nm (blue) by changing the size of PbS QDs, taken from [81].

In spite of all advantages of nanocomposites as active optoelectronic materials, the low mobility of organic materials is still a major barrier to commercialise such devices. The generated holes and electrons must transport through the materials to reach to the opposite electrodes. The transport must be fast enough for the carriers to be removed from the device before nonradioactive recombination can occur at the interface between two phases. The holes typically transport within the host matrix (p-type semiconductors) and the electrons either get trapped inside the QDs or flow toward positively biased electrodes by tunnelling or hopping through adjacent QDs [81]. A good hole-mobility matrix as well as a continuous conductive network of QDs can significantly enhance the photocurrent [122, 4].

According to the above discussion, the optimal band diagram for efficient photoconduction ability in an organic/inorganic nanocomposite is type-II [(a) or (d)] shown in Figure 3.16 [142]. In this type of band diagram, HOMO level of the p-type matrix is more favourable for holes while LUMO level of the QDs is preferable for electrons. Therefore, by excitons dissociation, the photogenerated holes and electrons will preferably transfer to the host matrix and the QDs, respectively. It has been observed that the surrounding capping ligands around QDs have a significant impact on transferring generated charges between QDs and the host matrix. Considerable improvement in photoconductivity of MEH-PPV/PbS nanocomposite has been observed by controlling the interfacial barrier between the capping ligand and the core of PbS QDs using different ligands and also thermal annealing [83]. Similar study on PbS/P_3HT nanocomposites has reached the same results [143].

3.3.4.2 Electrical properties and applications

The incorporation of nanoparticles into an organic matrix may improve the charge transport in the nanocomposite. The electrical properties of a nanocomposite strongly depend on the concentration of nanoparticles. At high concentration of nanoparticles (exceeding 15-20% volume), a connected network can be formed inside the matrix by nanoparticles, creating a pathway for carriers to traverse the distance between two electrodes [63]. Since nanoparticles are mostly nanoscale crystallites and have higher mobility compared to organic matrices, the existence of such a pathway can generally increase the charge mobility and enhance the overall electrical conductivity of the nanocomposite [4, 122, 144]. Watt *et al*. [145] measured the mobility of MEH-PPV/PbS nanocomposite using the time of flight technique and reported that the inclusion of PbS nanoparticles increases both electron and hole mobility by orders of magnitude. It was believed that the charge transport in the examined MEH-PPV/PbS nanocomposite is through two conductive pathways: a polymer-nanocrystal donor-acceptor pathway and a purely PbS percolation pathway.

But, in nanocomposites with low concentration of nanoparticles, the particles act as isolated centres which are not close enough to make a continuous network [4, 144]. In such nanocomposites, both the matrix and nanoparticles may partially involve the charge transport. In the simplest approximation, the carriers may pass through both phases while traversing the distance between two electrodes, as graphically shown in Figure 3.19. In this case, the overall mobility of the nanocomposite can be analogues to summation of series resistance made of both nanoparticles and the matrix [146, 147]:

$$\frac{1}{\mu} = \frac{x}{\mu^{NPs}} + \frac{(1-x)}{\mu^{M}} \tag{3.3}$$

where μ^{NPs} and μ^{M} are the mobility of nanoparticles and matrix, respectively and x is the volume fraction of the nanoparticles. Since the mobility in nanocrystals is much higher than the matrix, the total conductivity of the nanocomposite increases compared to that of the pure matrix. It should be noted that such an increase in the mobility is only possible in the nanocomposites that the energy levels of the nanoparticles and the matrix are almost in the same range, otherwise carriers may need to overcome barriers between the phases that significantly reduce the mobility.

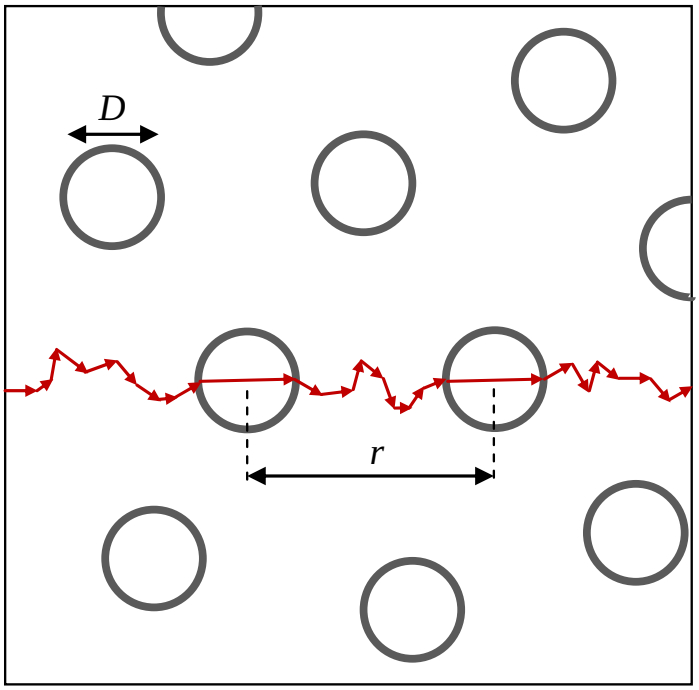

Figure 3.19 Illustrative representation of carriers path between two electrodes in a nanocomposite.

In nanocomposites containing capping agents around nanoparticles, the insulator layer surrounding nanoparticles typically creates a barrier between nanoparticles and host matrix and hampers the charge transfer to/from nanoparticles [4]. These

nanocomposites mainly show bistable conduction behaviour based on the trapping and detrapping of the injected charges and thus are good candidate for organic memory devices [148, 149, 150]. Figure 3.20 shows the bistable conduction behaviour of CdSe(ZnS) core-shell nanoparticles embedded in a conducting poly(N-vinylcarbazole) (PVK) [148]. By applying a positive bias to the nanocomposite of CdSe(ZnS)/PVK sandwiched between ITO and Al electrodes, the injected holes will be trapped inside the nanoparticles leading to low amount of current, called off-state. But, by exceeding from the threshold voltage in which all traps are almost filled, the current suddenly goes up, called on-state. It has been reported that the off-state can be recovered back by applying negative pulse of -2 V, shown by solid line in the figure. Increasing traps density enhances the on-off ratio of the device and consequently boosts the device performance.

The influence of nanoparticles on the structure of the matrix has also been suggested as a possible reason to either improve or reduce the conductivity of a nanocomposite, depending on the size and nature of nanoparticles, although it is still a subject of discussion [151]. The modified conductivity in nanocomposites of MEH-PPV containing nanoparticles such as TiO_2 and SiO_2 was claimed to be due to morphological change at the interface between nanocomposite and contact electrodes [152, 151], while the introduction of disordered in the polyonline/TiO_2 was believed to shorten the length of the polymer chain leading to reduction in nanocomposite conductivity [153].

The application of organic/inorganic nanocomposites as an active semiconducting layer of organic field effect transistors has been reported [154]. The hybrid

nanocomposites with high concentration of nanoparticles can be used as channel materials in OFETs since they may exhibit higher field-effect mobility. Such materials provide route to fabricate low-cost, light-weight and flexible transistors.

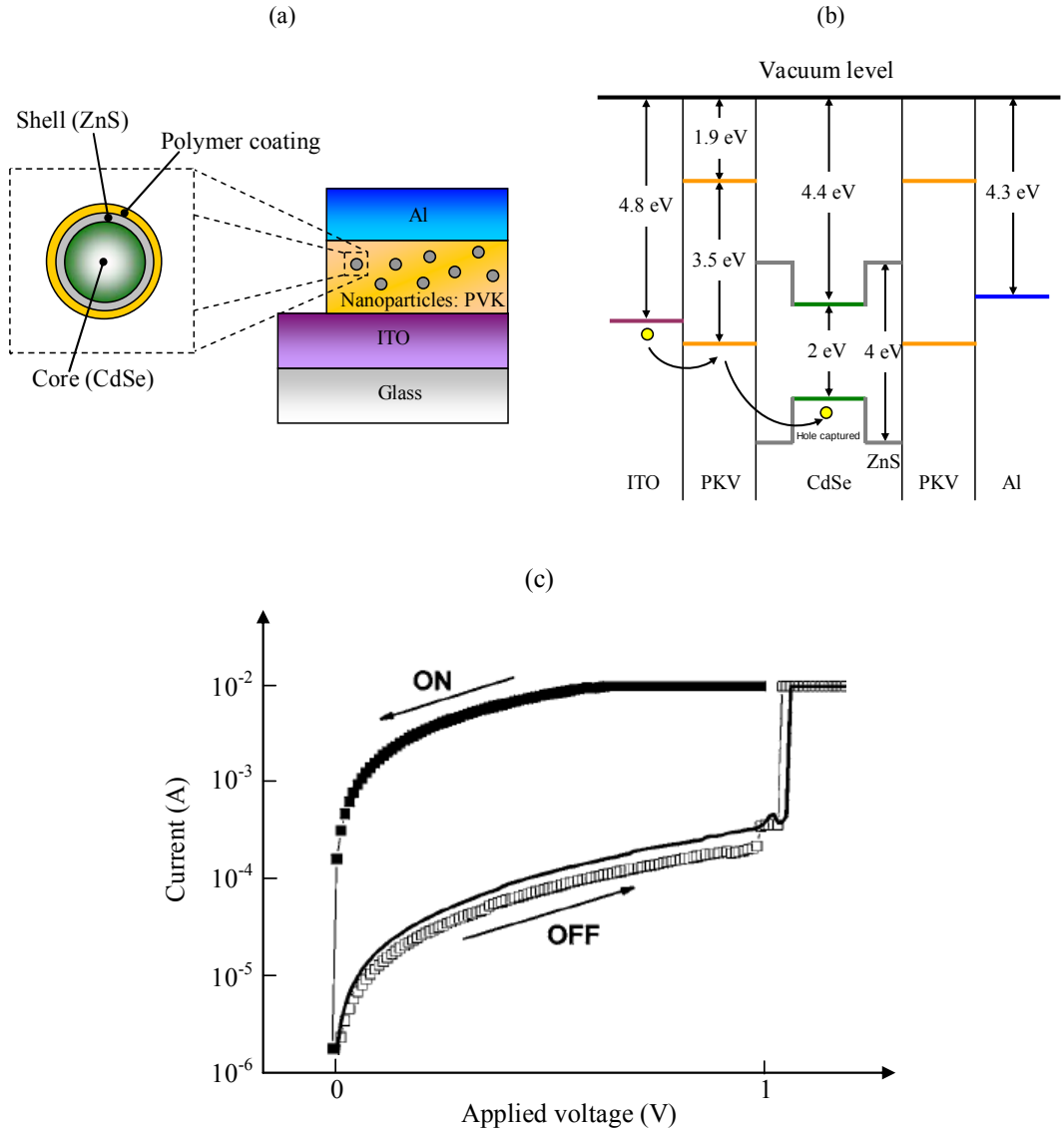

Figure 3.20 (a) The structure of memory device based on CdSe(ZnS)/PVK nanocomposite sandwiched between ITO and Al electrode; (b) the band diagram of the device; (c) the bistable behaviour of the device under positive bias applied to ITO. The empty and filled rectangles in the plot show the on and off-state respectively and the solid line shows the recovered off-state after applying -2 V pulse, taken from [148].

In addition, the organic/inorganic nanocomposites are good candidates for gate dielectric in OFETs. There are numerous reports regarding the increase in dielectric constant of nanocomposites by inclusion of high dielectric constant nanoparticles in the host matrix [155, 156]. One of the main applications of high dielectric constant materials is in the gate dielectric of OFETs [156]. The gate dielectric should have high dielectric constant to reduce the leakage current of the gate and thus enhance the transistor performance. This fact becomes crucially important when the device dimension shrinks to very low scale and the risk of leakage current increases significantly. Nanocomposite consisting of poly(methyl methacrylate-co-methacrylic acid) and titanium dioxide nanoparticles is an example of the nanocomposites with higher dielectric constant compared to the pure matrix [155]. Moreover, the nanocomposites in which nanoparticles act as traps, are also applicable as dielectric gate in transistors; nanoparticles trap the carriers and thus reduce the leakage current passing through the gate dielectric and subsequently improve the device performance [157, 158].

CHAPTER 4

Experimental Methods

4.1 Materials

This section introduces all the materials used in this study. Detailed information of each material has been listed in Table 4.1.

4.1.1 Nanocomposite

The precursor of this nanocomposite is a substituted lead phthalocyanine, 1-4-8-11-15-18-22-25-octa-hexyl lead phthalocyanine (called C_6PbPc hereafter), provided by research group in East Anglia University [159]. The provided C_6PbPc is in the powder form consists of tiny dark green needle-shape crystals. Figure 4.1 shows the chemical structure of C_6PbPc. Each C_6PbPc molecule is symmetrically substituted by eight chains of hexyl (C_6H_{13}). There are two special features of C_6PbPc compared to non-substituent lead phthalocyanines owing to the long substituent:

(i) C_6PbPc has some degrees of lead ion lability. The substituent chains change the geometry of the molecules resulting in the displacement of Pb^{2+}

ion from the centre of phthalocyanine ring and subsequently ease of loss of the Pb^{2+} ion [159]. This is the outstanding feature which facilitates the formation of lead sulphide through exposure to H_2S gas.

(ii) The long chain substituent increases the solubility of C_6PbPc and makes it suitable for solution-processed deposition techniques.

Table 4.1 Detailed information of the materials used in this study: precursors of the nanocomposite and substituted metal-free phthalocyanine.

Name	**Acronym**	**Molecular formula**	**Molar Mass (g/mol)**	**Supplier**	**Comment**
1-4-8-11-15-18-22-25-octa-hexyl lead phthalocyanine	C_6PbPc	$C_{80}H_{112}N_8Pb$	1393	[159]	Prepared by research group in East Anglia University
Toluene	$C_6H_5CH_3$		92.14	Sigma-Aldrich	Solvent
Hydrogen sulphide	H_2S		34.08	Sigma-Aldrich	Gas
1-4-8-11-15-18-22-25-octa-hexyl metal-free phthalocyanine	C_6H_2Pc	$C_{80}H_{114}N_8$	1187.83	[159]	Prepared by research group in East Anglia University

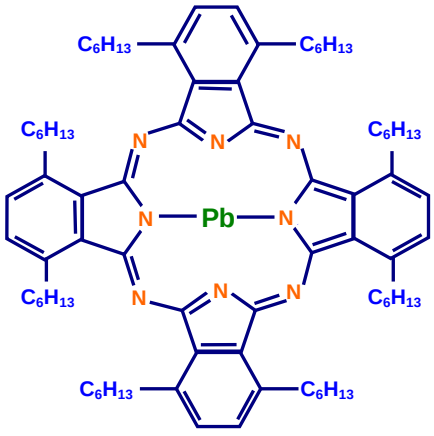

Figure 4.1 Chemical structures of 1-4-8-11-15-18-22-25-octa-hexyl lead phthalocyanine (C_6PbPc).

4.1.2 Metal-free phthalocyanine

Thin film of the pure host matrix, C_6H_2Pc, is also characterised in this study for the sake of comparison. C_6H_2Pc, 1-4-8-11-15-18-22-25-octahexylphthalocyanine metal-free phthalocyanine was provided by research group in East Anglia University [51]. Each C_6H_2Pc molecule is substituted similar to C_6PbPc; its chemical structure is depicted in Figure 4.2. It is in the powder form composed of tiny blue plates with a crystalline structure. Thin film of C_6H_2Pc was prepared similar to C_6PbPc, as will be presented in the later sections.

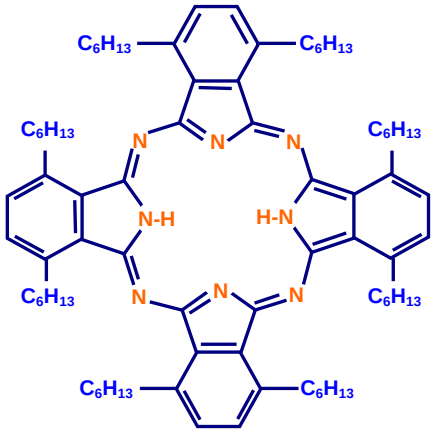

Figure 4.2 Chemical structures of 1-4-8-11-15-18-22-25-octahexylphthalocyanine metal-free (C_6H_2Pc) molecules.

4.2 Preparation of C_6H_2Pc/PbS nanocomposite

The formation of lead sulphide quantum dots in a phthalocyanine matrix has been reported for the first time by Nabok, Ray *et al.* [8]. The nanocomposite is constructed in the form of thin film through a simple procedure. The preparation processes are comprised of two main steps:

1- Fabricating the thin film of substituted lead phthalocyanine

2- Exposure of the film to hydrogen sulphide (H_2S) atmosphere in order to constitute the nanocomposite

The details of each step have been explained in the following sections.

4.2.1 Lead phthalocyanine film deposition

Thin film of C_6PbPc is deposited by the spin coating technique. The substrates are pieces of glass, ITO-coated glass, quartz and silicon wafer, each suitable for a specific experiment as will be explained in the corresponding sections. All of these substrates have been cut to small pieces of $10\,\text{mm} \times 10\,\text{mm}$ and cleaned properly prior to film deposition. Details of the substrates cleaning process and the film deposition are presented below.

4.2.1.1 Substrates cleaning

The cleaning process is simple but one of the important steps in the thin film technology. Any contamination would increase the level of impurity in the film and also affect the uniformity and homogeneity of the film. In order to properly clean substrates, the following processes were carried out in a class ISO 7 cleanroom. The cleaning procedure was the same for all types of the substrates.

1. 20 minutes sonication in the solution of distilled water and detergent.
2. 5 minutes sonication in distilled water (three times repeated).
3. 5 minutes sonication in acetone (two times repeated).
4. 5 minutes sonication in chloroform (two times repeated).

The cleaned substrates were then dried with nitrogen gas prior to film deposition.

4.2.1.2 C_6PbPc solution

The C_6PbPc is soluble in most organic solvents, however higher solubility has been observed in toluene solution. The solution of C_6PbPc in toluene with concentration of

10 mg/ml was prepared by dissolving C_6PbPc powder in toluene. The solution was prepared prior to the film deposition and kept in a dark bottle to avoid any possible degradation.

4.2.1.3 Spin coating

Thin film of C_6PbPc was produced using both spin coating and drop casting methods. The model KW-4A spin coater, from Chemat technology, Inc., is used for this purpose. The spin coating procedure, as illustratively shown in Figure 4.3, was performed by the following steps:

1. Deposition about 0.1 ml of the C_6PbPc solution on top of the cleaned substrates using microsyringe.
2. Rotating the substrate at the speed of 1000 rpm in order to disperse the solution all over the surface due to the centrifugal force.
3. The rotating continues for 20 seconds to partially evaporate the solvent.

The spun film was then kept in a dark, low vacuum and moisture-free desiccator for 18 hours to be completely dried. One of the features of the spin coating technique is the ability to optimise the thickness of films by the solution concentration and the speed of spinning. The more solution viscosity, the higher spinning speed is required to form a uniform thin film. The above procedure provides a uniform thin film with around 130 nm thickness.

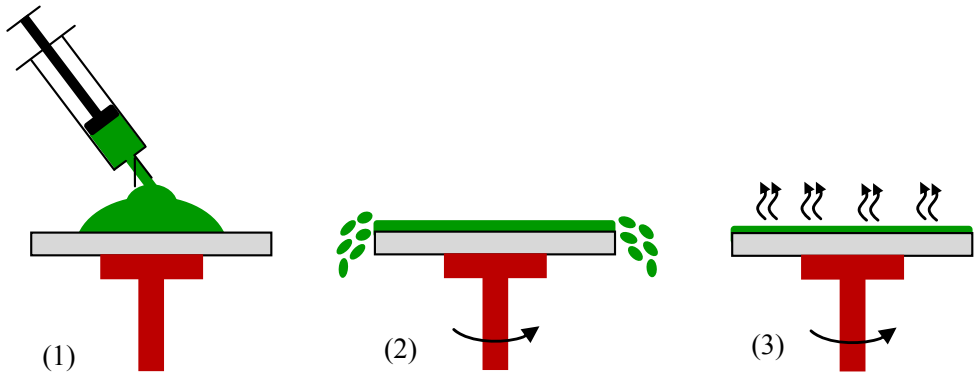

Figure 4.3 Illustrative representation of static spin coating procedure.

4.2.2 Exposure to H_2S atmosphere

The dried spun film of C_6PbPc was exposed to H_2S gas for about 24 hours. The lead ions are rather weakly bound to the phthalocyanine ring due to the geometrical structure of C_6PbPc. Exposure of C_6PbPc films to H_2S gas releases the bound Pb^{2+} ions from C_6PbPc molecules and transforms them into substituted metal-free phthalocyanine molecules (C_6H_2Pc) according to the following reaction [8]:

$$C_6PbPc + H_2S \rightarrow PbS + C_6H_2Pc \qquad (4.1)$$

This reaction leads to formation of PbS molecules and then small QDs by low level of aggregation between PbS molecules. Figure 4.4 displays photos of the fabricated C_6PbPc film before and after exposure to H_2S gas. The colour change is due to converting C_6PbPc to C_6H_2Pc and formation of dark PbS QDs.

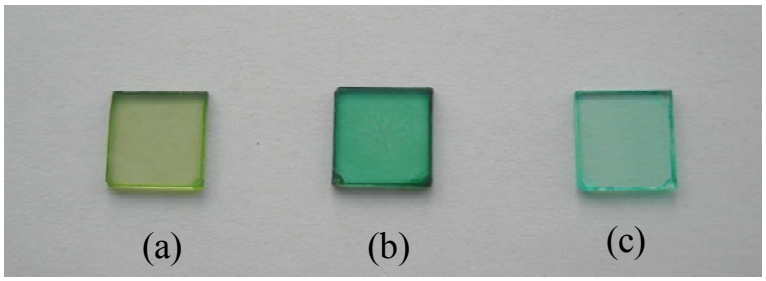

Figure 4.4 Thin film of (a) C_6PbPc ;(b) C_6PbPc after exposure to H_2S gas, i.e. C_6H_2Pc/PbS nanocomposite; and (c) C_6H_2Pc, all prepared in the laboratory.

4.2.2.1 H_2S treatment set-up

As H_2S gas is toxic with a strong odour, a specific setting, shown in Figure 4.5, is required to perform the experiment safely. H_2S gas is allowed to flow into the container and then passes through the saturated sodium hydroxide (NaOH) solution twice to reduce the toxicity of the H_2S gas and then exits the setting. H_2S gas reacts with NaOH resulting in two compounds, sodium hydrosulphide and the sodium sulphide, which both are soluble in water [160]. The inlet and outlet valves of the container and the gas cylinder valve are closed after 5 minutes which is enough time to fully fill the sealed container with H_2S gas. The C_6PbPc film is kept in the sealed container for 24 hours. For more safety and precaution, the setting must be placed under a fume cupboard.

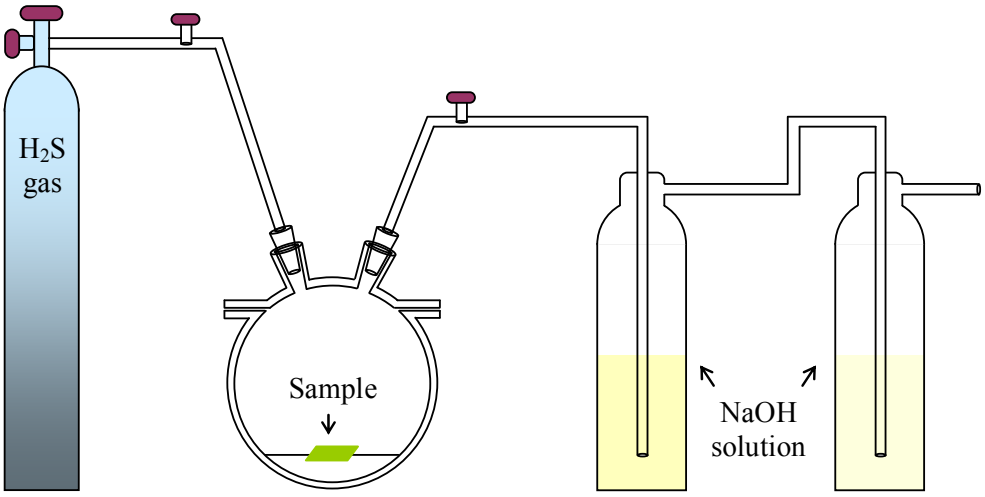

Figure 4.5 Illustrative representation of H_2S gas treatment set-up.

4.3 Physical characterisation

X-ray diffraction and transmission electron microscopy techniques are employed to verify the formation of PbS QDs. The optical absorption property of PbS QDs is also studied by the ultraviolet-visible spectroscopy technique. The specimen of each characterisation method should meet up specific criteria to yield the most accurate

results. So the preparation method and also the substrate used may differ for each characterisation technique. A brief explanation about the principle of these techniques, along with the specification of specimen for each technique is presented in this section.

4.3.1 X-ray diffraction

X-ray diffraction (XRD) is an analytical method to obtain information about the crystalline structure of materials. Each solid material has a unique crystal characteristic, so this technique can also be used to identify a material by comparing its spectrum with the standard database of known materials. The technique is based on the elastic scattering of incident X-ray beam from a crystalline structure. When an X-ray hits a crystal, it may be either transmitted or scattered by the electrons around atoms. As a crystal is a regular arrangement of atoms, the scattered X-rays are an array of regular waves in different direction that can interfere constructively or destructively. Only the constructive interference is favourable for the XRD technique and its intensity is measured by a detector as a function of the incident angle. The spacing between the crystal planes can be found by Bragg's law which is expressed by [128]

$$n\lambda = 2d \sin\theta \tag{4.2}$$

where λ is the wavelength of the X-ray beam, n is any integer number, d is the space between the scattering planes and θ is the incident angle. Figure 4.6 shows the illustrative concept of Bragg's law. In a single crystalline material there is only one sharp Bragg peak while in a polycrystalline material several Bragg peaks may be detected.

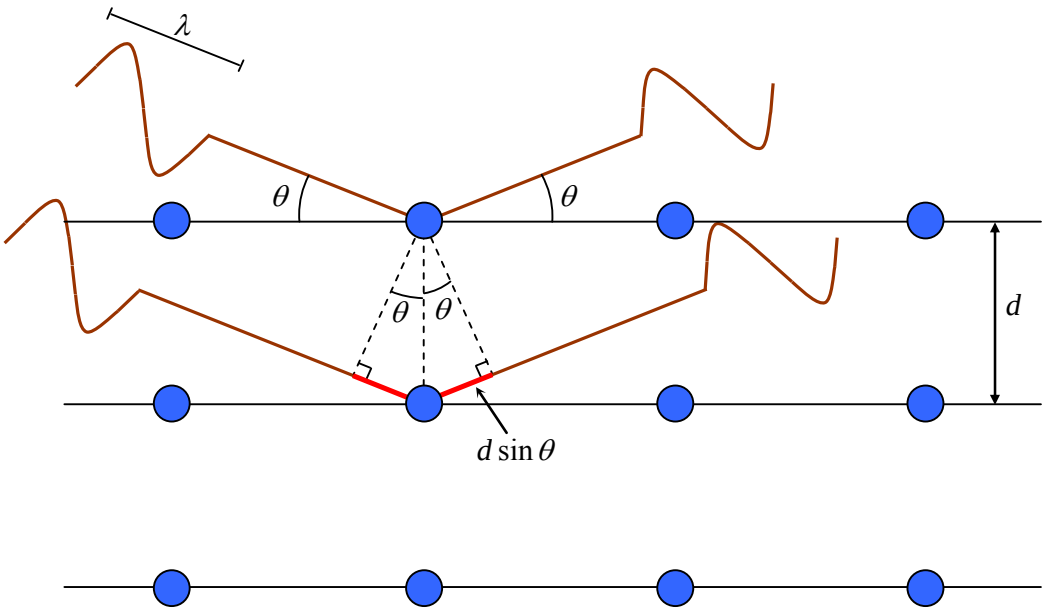

Figure 4.6 Illustrative concept of Bragg's law.

4.3.1.1 Specimen preparation

The specimen for the X-ray diffraction analysis must be thick in order to have enough diffracting volume to intensify diffracted beams and minimise the effects of substrate interference. Thereby, the drop casting technique was chosen to prepare a thick film. Silicon wafer was used as substrate for XRD specimens because it is typically a single crystalline material with a sharp Bragg peak which can be easily subtracted from the specimen diffraction spectrum in case of any possible substrate interference. About 0.2 ml of the C_6PbPc solution was deposited on top of a cleaned substrate and then placed in a dark, low vacuum and moisture-free desiccator for 24 hours to be fully dried. Then the nanocomposite was constructed by exposing the film to H_2S gas, as explained before. This method provided specimens with average thickness of 1 μm.

4.3.1.2 Equipment

In the current research, the X-Ray diffraction spectrum of the nanocomposite film is

obtained using Siemens D5000 X-Ray Diffractometer with the incident radiation wavelength of 1.54056 $\mathring{A}$. The grazing set-up was used for goniometer, in which a small angle of 2^o was set between the specimen and the incident beam while the detector is rotating by angle 2θ .

4.3.2 Transmission electron microscopy

Transmission electron microscopy (TEM) is an imaging technique which operates in the similar way as an optical microscope, but uses electron beam instead of light beam. High magnification of up to one million times is one of the main advantages of this microscope. In this technique, two sets of information can be achieved, a magnified image and a diffraction pattern. Utilising both sets, all knowledge about size, shape and arrangement of particles in the specimen as well as information about the structure of crystalline materials can be achieved. Diffraction pattern can provide information about the structure and lattice spacing of crystalline materials and can be used to identify an unknown material by comparison with the standard database of known materials. Considering the electrons as a series of waves, the formation of diffraction pattern has the same principle as X-ray diffraction. As the electron beams hit the specimen, they may either be transmitted or scattered. If the scattered electrons interfere constructively, they would create a series of bright spots on the viewing screen and generate a diffraction pattern. The pattern consists of a regular array of spots in the case of single-crystalline materials and a series of concentric rings formed by many spots closed together in the case of polycrystalline. The relationship between the radius of the rings, *r*, and the lattice spacing, *d*, for a small angle of diffraction is expressed by [128]

$$rd = l\lambda \tag{4.3}$$

where λ is the wavelength of the electron beam and l is the camera length. The term of $l\lambda$ is called camera constant.

4.3.2.1 Specimen preparation

The specimens for transmission electron microscopy should be thin enough (about a few tens of nanometre) to be electron transparent. In order to prepare such a thin film, the nanocomposite film was first constructed on top of a cleaned glass substrate, and then the prepared film was gently scratched to transform it to powder-like form. The fragments were dispersed in distilled water and then placed on top of a 3 mm diameter copper-coated grid. The specimen was ready to be located into the microscope when the water completely evaporated.

4.3.2.2 Equipment

In this study, the TEM results were obtained using Jeol Jem-2010 to confirm the formation of PbS nanoparticles as well as find the particle size. The instrument was calibrated prior to the measurement using an aluminium thin foil as a specimen with setting 80 cm camera length at 200 KV accelerating voltage.

4.3.3 Ultraviolet-Visible absorption spectroscopy

Materials can absorb the energy of light and convert it to other form of energy such as heat or transform the state of atoms from the ground state to the excited state. Due to this fact, the intensity of the incident light is reduced by passing through an absorbing material. The term absorbance, *A*, is defined as

$$A = -\log \frac{I}{I_0} \tag{4.4}$$

where I_0 and I are the intensity of incident and transmitted light, respectively, see Figure 4.7. The Beer-Lambert law expresses that the absorbance is directly proportional to the concentration of the absorbing material, c, and the light path length, d, written as [161]

$$A = c\varepsilon_a d = \alpha d \tag{4.5}$$

where ε_a and α is molar absorptivity and the absorption coefficient, respectively.

The ultraviolet-visible (UV-Vis) spectroscopy technique is employed to measure the absorbance of materials for a specific wavelength. The range of wavelengths used in this technique is in visible and adjacent region, i.e. near ultraviolet and infrared.

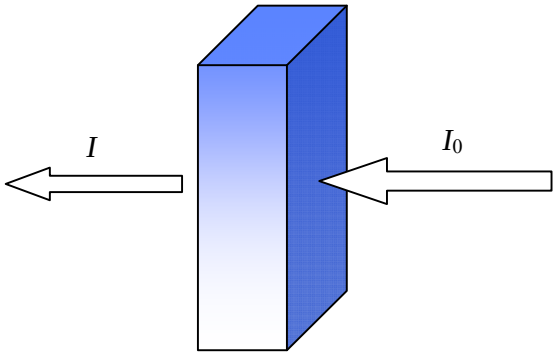

Figure 4.7 Illustration of the Beer Lambert law. I_0 is the incident light and I is the transmitted light.

4.3.3.1 Specimen preparation

Quartz is a non-absorbing material in the ultraviolet-visible region and thus suitable substrate for absorption spectroscopy measurement in this region. The optical absorption specimen was prepared by constructing the nanocomposite on top of the cleaned quartz substrates.

4.3.3.2 Equipment

In this study, Perkin Elmer lambda 950 Spectrometer was used to obtain the absorbance spectra of the films on top of the quartz substrates. The selected wavelength ranged between 350 and 900 nm with the speed of 10 nm per second. In order to avoid the effect of substrate absorbance, the absorbance of a clean quartz substrate has been measured simultaneously and subtracted from the film results.

4.4 Electrical characterisation

The electrical property of the nanocomposite is studied in the form of a sandwich structure device using indium-tin-oxide (ITO) and aluminium (Al) electrodes. All the electrical measurements are run in a dark condition to avoid any possible contribution of photoconductivity. In this section, first the fabrication of the sandwich structure device is described and then the instruments employed for the electrical study are introduced.

4.4.1 Sandwich structure of Al-C_6H_2Pc/PbS-ITO

The sandwich structure device is fabricated by constructing the nanocomposite thin film on top of a $10\,\text{mm} \times 10\,\text{mm}$ ITO-coated glass substrate with 30 Ω/sq resistance, and then Al electrode is evaporated on top of the film. The fabrication procedure is explained below and graphically shown in Figure 4.8.

4.4.1.1 Etching ITO

Before depositing the film, the ITO was lithographically patterned. This stage is necessary in nanoscale sandwich structure devices to avoid short circuiting between

top and bottom electrodes while the device is connected to the circuit. The stepwise procedure is:

1- ITO substrates were cleaned by the procedure explained before.

2- A thin layer of Shipley 1818 photo-resist was deposited on top of the cleaned ITO substrates by spin coating method. The substrates were then put in an oven for 15 minutes at 110 ^{o}C to be completely dried.

3- The photo-resist coated substrates were exposed to ultraviolet (UV) light through the mask in order to create the desired pattern on the ITO substrates. Through the UV light exposure, the parts of photo-resist layer that exposed to UV light become soluble in photo-resist developer.

4- The substrates were then submerged into developer, sodium-hydroxide solution, to remove the photo-resist layer from the desired parts, and then rinsed twice with distilled water. After this stage, the photo-resist layer only covered the required part of the ITO substrate.

5- The unwanted ITO was etched by immersing the substrates into ~50 ^{o}C solution of hydrochloric acid, nitric acid and distilled water (48%:2%:50%). By this step, the ITO substrate was patterned.

6- The remaining photo-resist layer was then removed by rinsing substrates into Acetone.

1. ITO-coated glass substrate

2. Substrate with spin coated photo-resist

3- Exposure to UV light while covered by mask

4. Developed photo-resist

5. Etched ITO

6. Patterned ITO Substrate

7. Prepared nanocomposite thin film

8. Deposited Al

9- Top view of the final device, with copper wire connected by silver paste

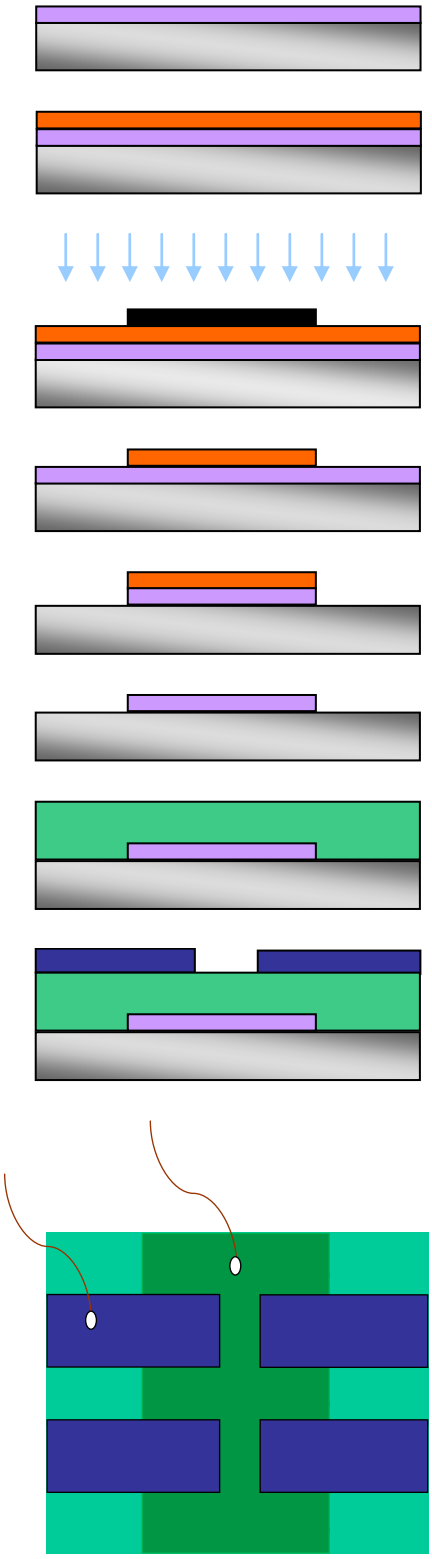

Figure 4.8 Fabrication procedure of the sandwich structure device.

4.4.1.2 Thin film deposition

The substrates might be contaminated during the ITO etching process, so the cleaning process was repeated again prior to film deposition. A thin film of the nanocomposite was constructed on top of the patterned ITO substrate by the procedure explained in the previous section.

4.4.1.3 Electrode deposition

At the final stage, the 60 nm thin aluminium electrode was deposited on top of the film by thermal evaporation technique. Thermal evaporation is a commonly used technique to deposit a thin layer of metals on top of organic films, and consists of two basic processes: evaporation of a source material and then condensation back the vapour on the substrate. More details about this technique can be found in [27]. A Kurt J. Lesker SPECTROS evaporation system was used for Al evaporation in this work. The substrate was loaded into the system while covering by a mask having four $3\,\text{mm} \times 3\,\text{mm}$ holes. The deposition was performed under high vacuum around 10^{-7} mBar, and the distance between the crucible containing aluminium and the substrate was set to be 200 mm. The deposition rate was $1\ \text{Å}\,\text{s}^{-1}$ for the first 10 nm Al film to minimise the rate of aluminium penetration inside the film, and then increased to $3\ \text{Å}\,\text{s}^{-1}$ for the rest of the process.

Therefore, four sandwich structure devices with the effective area of about 4.5 mm^2 were fabricated on each substrate, as shown in Figure 4.8. To connect the fabricated device to the measuring instrument, tiny copper wires were attached to the Al electrodes and ITO substrate using silver paste. The silver paste was placed on the part of Al electrodes where there was no overlap with ITO substrate. To reach to the

ITO substrate, a very small part of the nanocomposite film on top of the ITO substrate, away from Al electrodes, was removed by a cotton stick. Each device was mounted on top of the sample holder of a cryostat and connected to the corresponding pins using silver paste.

4.4.2 Employed equipments

4.4.2.1 Steady-state electrical measurement

The electrical measurement was carried out using Keithley 4200-SCS semiconductor characterisation system. The instrument was provided with a preamplifier which reduces the effects of noise in very low current measurement (in the range of pA). The voltage was swept in the range of ± 2 V with an increment of 0.05 V. In all measurement, the bias was applied to ITO with respect to Al.

4.4.2.2 Impedance spectroscopy

The frequency response of the nanocomposite conduction was obtained using Autolab Potentiostat PGSTAT30. The experiment was run by applying an AC signal with amplitude of 0.1 V by sweeping frequency from 100 Hz to 1 MHz at temperatures ranging from 100 K to 293 K. The instrument returns the real and imaginary parts of the admittance.

4.4.2.3 Cryogenic system

A continuous-flow cryostat, made by Oxford Instruments, was employed to measure the temperature-dependence of the electrical characteristic of the devices. The cryostat operated on the dynamic mode by circulating nitrogen gas around the device holder. During the experiment, the cryogen liquid continuously transferred from a

cryogen container to the cryostat through a transfer tube. The temperature was controlled using ITC503 temperature controller, made by Oxford Instruments, by which the temperature was measured via a temperature sensor near the device holder, while the rate of cryogen flow was controlled manually. The temperature range used in this study is between 100 K and 293 K.

4.4.2.4 Thickness measurement

Thickness of the films was measured using DekTak 3ST surface profiler. The profilometer measures the small surface variation using a stylus which moves horizontally across the surface to detect the surface variation presence on the film. To determine the film thickness, a few steps were created by scratching some parts of the film. Thickness of the spun nanocomposite film and C_6H_2Pc was found to be around 130 nm and 100 nm, respectively.

CHAPTER 5

Material Characterisation

5.1 X-ray diffraction

X-ray diffraction spectrum of the nanocomposite film on top of a silicon wafer is shown in Figure 5.1. The XRD spectra of pure C_6H_2Pc and C_6PbPc are also included to assist a correct analysis. The observed Bragg's peaks in the nanocomposite spectrum correspond to both components, C_6H_2Pc and PbS. The indicated peaks by green lines in Figure 5.1 (a) are related to C_6H_2Pc as they are similarly observed in the XRD spectrum of pure C_6H_2Pc, shown in Figure 5.1 (b). The appearance of several Bragg's peaks in the C_6H_2Pc spectrum is a signature of polycrystalline structure of drop cast C_6H_2Pc film. The observed peaks at 2θ of 25.96, 30.03 and 43.08 (all in degrees) in the nanocomposite spectrum are perfectly matched with the Bragg's peaks corresponding to 111, 200 and 220 crystal planes of PbS, according to the standard database of PbS crystals, presented in Appendix 1. The spacing between scattering planes, d, has been calculated using Bragg's law, Equation (4.2), and summarised in Table 5.1. This observation verifies the presence of PbS compound in the constructed nanocomposite. Generally, nanoparticles have a single crystal structure as they are too small to have more than one crystalline zone. The

observation of more than one Bragg's peak of PbS implies that all of the formed PbS nanocrystals may not be orientated at the same direction.

Some of the peaks in the nanocomposite spectrum (indicated by purple lines) are consistent with the peaks observed in the C_6PbPc spectrum shown in Figure 5.1 (c). They are related to C_6PbPc molecules which had no reaction with H_2S gas and remained intact in the nanocomposite film. The probable trace impurities in the thin film of nanocomposite can be considered as the possible source of the unknown observed peaks.

Table 5.1 Bragg's peaks corresponding to the PbS crystal planes in H_2S-treated sample.

No.	2θ (degrees) experiment	d (Å) experiment	2θ (degrees) database	d (Å) database	h	k	l
1	26.07	3.41	25.964	3.42	1	1	1
2	30.09	2.97	30.075	2.96	2	0	0
3	42.93	2.10	43.059	2.09	2	2	0

5.2 PbS QDs size

The well-known Scherrer equation (Equation (3.2)) has been applied to calculate the size of the PbS nanoparticles by measuring the width of their Bragg peaks. Using this equation, the average size of the particles has been estimated to be 5.9 nm, which is far less than 18 nm of exciton Bohr radius of PbS, confirming they are quantum dots. This observation is indicative of the capability of the formation of PbS particles as small as quantum dots by the method applied to prepare this nanocomposite. In fact, the rigid environment of the solid film of C_6H_2Pc can limit the aggregation of the PbS QDs and stop them forming larger particles. Table 5.2 shows the details of the particle size calculation.

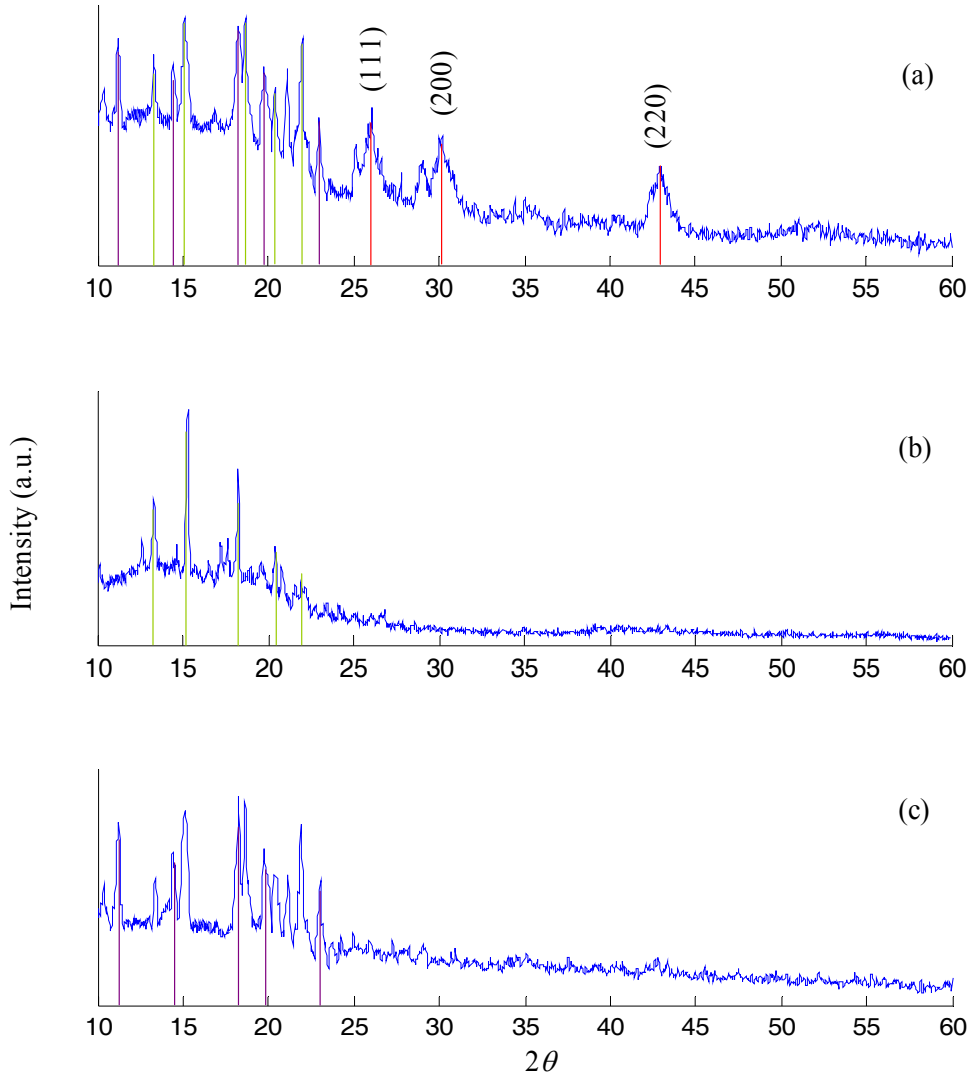

Figure 5.1 X-Ray diffraction pattern of (a) C_6H_2Pc/PbS nanocomposite, (b) pure C_6H_2Pc and (c) pure C_6PbPc. The observed Bragg's peaks correspond to PbS crystal planes have been marked by red lines.

Table 5.2 The calculation of PbS QDs size using the Scherrer equation. *D* is the average diameter of QDs.

No.	2θ (degrees)	β (radians)	*D* (nm)
1	26.07	0.022	6.00
2	30.09	0.023	5.81
3	42.93	0.021	5.87

5.3 Transmission electron microscopy

The bright-field TEM images of C_6H_2Pc/PbS nanocomposite have been depicted in Figure 5.2. The formation of nanoparticles, darker phase, with average diameter of 4.5 nm is clearly observed in the figure. The size of nanoparticles is in good agreement with that calculated by the Scherrer equation. The PbS QDs are roughly spherical in shape and dispersed separately from each other. The crystal lattices of the PbS QDs in different orientations are observable in the high resolution image indicating the produced QDs are single crystallites. The major lattice spacing measured through the lattice fringes in the image is about 2.9 Å corresponding to 200 crystal plane of PbS, according to standard database of bulk PbS presented in Appendix 1. In order to accurately identify the PbS compound through the crystal lattice parameters, the selected-area diffraction pattern of the nanocomposite has been obtained, as presented in Figure 5.3 (a). The two concentric circles with bright spots in the figure are indicative of two set of crystal planes. The spacing between each set of planes is calculated based on Equation (4.3) to be 2.90 and 2.00 Å which respectively correspond to 200 and 220 crystal planes of PbS. The calculated lattice spacing in comparison with PbS database has been summarised in Table 5.3. It should be noted that the TEM specimen is prepared from the dispersive fragments of the nanocomposite film. So, the diffraction pattern can be analogous to X-ray powder diffraction which is mainly utilised for materials identification rather than structural characterisation. This observation confirms the formation of PbS nanocrystals in the nanocomposite. No evidence of C_6H_2Pc crystal lattice is found in the diffraction pattern of the nanocomposite, probably due to amorphous-like diffraction pattern of C_6H_2Pc. The selected-area diffraction pattern of pure C_6H_2Pc, prepared by scratched fragments of the film, exhibits amorphous-like pattern, as shown in Figure 5.3 (b).

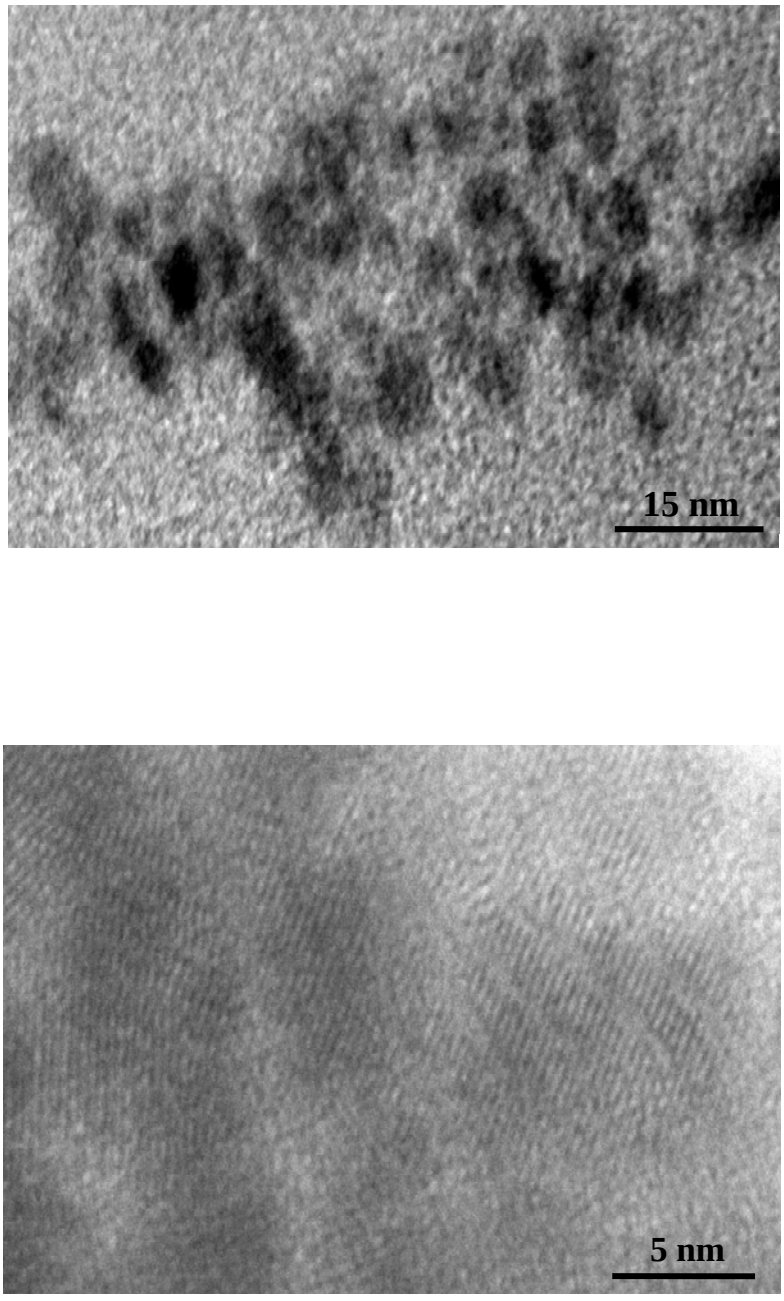

Figure 5.2 TEM images of the C_6H_2Pc/PbS nanocomposite. The darker phases are the PbS quantum dots.

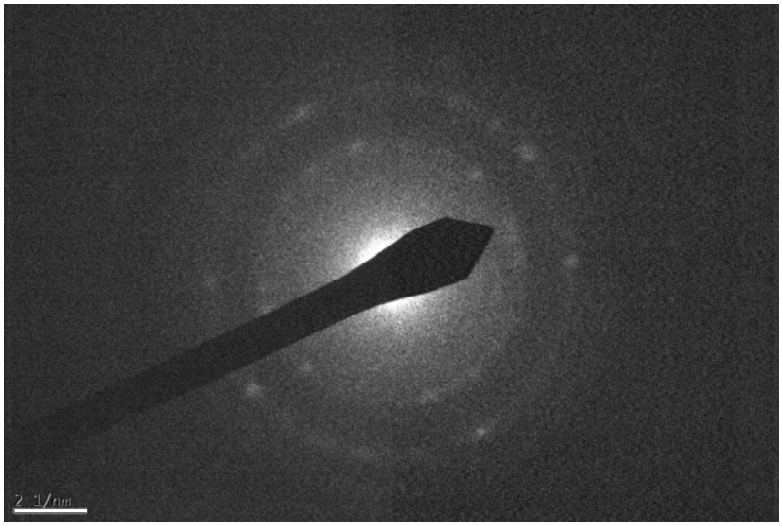

(a)

(b)

Figure 5.3 The selected-area diffraction pattern of (a) C_6H_2Pc/PbS nanocomposite, the two bright concentric circuits are related to 200 and 220 crystal planes of PbS, and (b) pure C_6H_2Pc.

Table 5.3 The calculated lattice spacing based on the diffraction pattern.

No.	Component	d (Å) experiment	d (Å) database	h	k	l
1	PbS	2.90	2.96	2	0	0
2	PbS	2.00	2.09	2	2	0

5.4 Compositional features

One of the special features of the constructed C_6H_2Pc/PbS nanocomposite is the mass fraction limitation of the PbS QDs. Unlike those nanocomposites in which the concentration of nanoparticles in the matrix is changeable, the concentration of the PbS QDs in this nanocomposite has an upper limit and cannot exceed from a fixed value. The reason is arising from the limited density of the Pb^{2+} precursors in the film. Each C_6PbPc molecule has only one Pb^{2+} ion at the centre of the phthalocyanine ring, which is released by exposure to H_2S gas and C_6H_2Pc is formed. Therefore, there is only one PbS molecule formed per each C_6H_2Pc molecule. A few number of the PbS molecules are then agglomerated and form one quantum dot. In an ideal situation where all of the C_6PbPc molecules are converted to C_6H_2Pc, the mass fraction of the PbS QDs, w, is calculated and found to be 17 wt % using $w = M^{QD}/\left(M^{QD} + M^{Pc}\right)$ where $M^{QD} = 239.27$ g.mol^{-1} and $M^{Pc} = 1187.83$ g.mol^{-1} are the molecular weights of PbS and C_6H_2Pc, respectively. Having known the density of PbS, $\rho^{QD} = 7.60$ g.cm^{-3} (Appendix 1), and C_6H_2Pc, $\rho^{Pc} = 1.121$ g.cm^{-3} [162], the volume fraction of the PbS QDs, x, is obtained to be 0.03 using the following expression [146]

$$x = \frac{\dfrac{w}{\rho^{QD}}}{\dfrac{w}{\rho^{QD}} + \dfrac{(1-w)}{\rho^{Pc}}}. \tag{5.1}$$

The volume fraction of nanoparticles is one the main parameters to characterise a nanocomposite. If the size of nanoparticles is known, the concentration of nanoparticles, n^{QD}, and subsequently the average distance between them, $\tilde{r}$, can be determined by [146]

$$n^{QD} = 6x/D^3\pi \tag{5.2}$$

$$\tilde{r} = \left(n^{QD}\right)^{-1/3} \tag{5.3}$$

where D is the nanoparticles diameter and $\tilde{r}$ is to the distance between centres of two neighbouring particles. Considering the average diameter of the formed PbS QDs to be about 4.5 nm, n^{QD} and $\tilde{r}$ are found to be about 6.1×10^{23} m^{-3} and 11.7 nm, respectively. These values are summarised in Table 5.4.

Table 5.4 Parameters regarding the distribution of the PbS QDs in the nanocomposite.

Parameters	**Symbols**	**Values**	**Units**
Mass fraction of PbS QDs	w	17	wt %
Volume fraction of PbS QDs	x	0.03	
Concentration of PbS QDs	n^{QD}	6.1×10^{23}	m^{-3}
Average distance between PbS QDs	$\tilde{r}$	11.7	nm

CHAPTER 6

Optical Absorption Spectroscopy

6.1 Optical absorption property

UV-Vis absorption spectrum of C_6H_2Pc/PbS nanocomposite has been depicted in Figure 6.1. As evident from the figure, the nanocomposite is mostly absorbing at the region between 650 and 750 nm, and also the region below 400 nm.

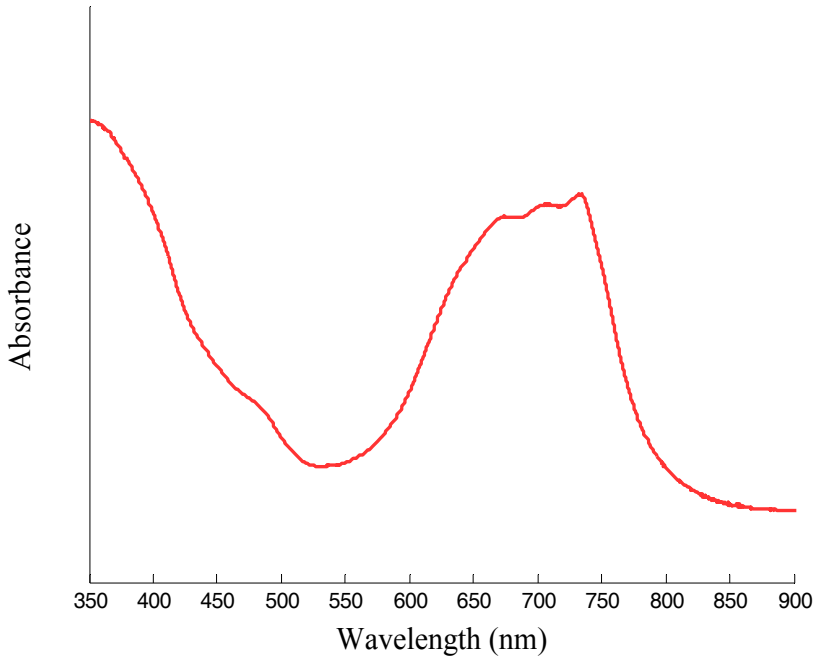

Figure 6.1 The optical absorption spectrum of C_6H_2Pc/PbS nanocomposite.

The total optical absorbance of a nanocomposite, A_{NC}, is expressed by the following expression as illustratively shown in Figure 6.2,

$$A_{NC} = A_{matriix} + A_{QD} \tag{6.1}$$

where

$$A_{matrix} = -\log(I_1/I_0) \tag{6.2}$$

$$A_{QD} = -\log(I/I_1) \tag{6.3}$$

$$A_{NC} = -\log(I/I_0) \tag{6.4}$$

where I_0, I_1 and I are, respectively, the intensity of the source light, the intensity of the light after passing through the matrix and the intensity of the light leaving the sample.

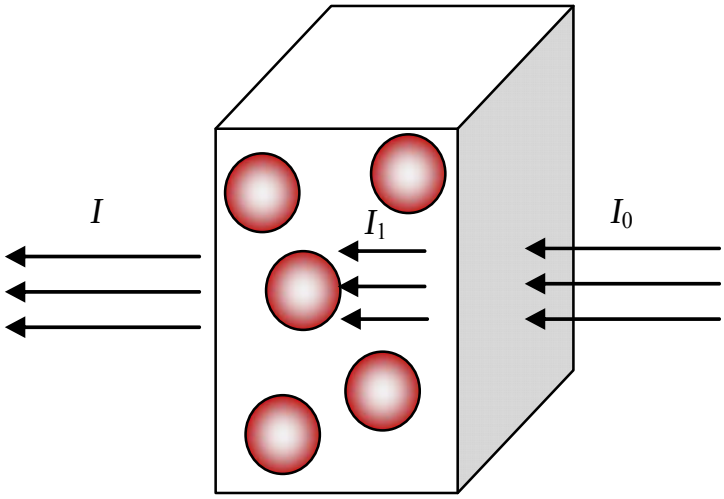

Figure 6.2 Illustrative representation of a nanocomposite absorbance. The source light with the intensity of I_0 first passing through the matrix may result in partially absorbing the source light and reducing the intensity to I_1. The light with intensity of I_1 then further reduces to I by going through the nanoparticles. The total absorbance of the nanocomposite is thus expressed by $A_{NC} = -\log(I/I_0)$.

The absorption spectrum of pure C_6H_2Pc film has been separately obtained in this study. The absorption spectrum of PbS QDs is not unique and varies with the size of PbS QDs; the onset of absorption is shifted to shorter wavelength by decreasing the QDs' size. In order to obtain the absorption spectrum of the produced PbS QDs, the absorption spectrum of pure C_6H_2Pc is subtracted from that of the nanocomposite. The details of this procedure are presented in the following subsections.

6.1.1 Absorption spectrum of C_6H_2Pc

UV-Vis absorption spectrum of pure C_6H_2Pc film has been shown in Figure 6.3. The main absorption region is between 650 and 750 nm corresponding to a broad double Q-band and a Soret band around 350 nm. Phthalocyanines are molecular crystals and the Q-band generally represents π-π^* transition in these compounds. In metal-free phthalocyanines, the Q-band is typically split, also called double Q-band, due to degeneracy at their LUMO level [46]. However, the split Q-band is not so clear at longer wavelengths [46]. Comparing to an unsubstituted metal-free phthalocyanine, the Q-band of C_6H_2Pc is shifted to a longer wavelength due to the existence of the substituent chains [62], and therefore the Q-band splitting is small.

For comparison, the absorption spectrum of C_6H_2Pc/PbS nanocomposite is shown again in Figure 6.3. The resemblance between the spectra of the nanocomposite and C_6H_2Pc film clearly indicates that the absorption features of the nanocomposite at 650-750 nm mainly correspond to C_6H_2Pc matrix. The slight discrepancy between the absorption peaks at this region, apart from their intensity, be attributed to a number of reasons such as different molecular arrangement of C_6H_2Pc molecules in each of the films [51], presence of some non-reacted C_6PbPc molecules in the nanocomposite film and/or the effects of the PbS QDs absorption. This issue will be discussed in the next subsection.

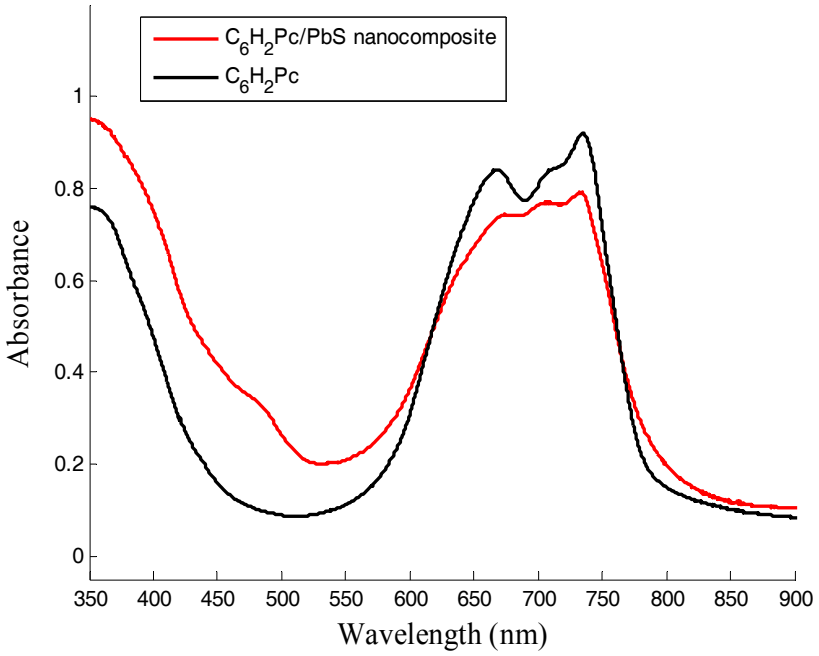

Figure 6.3 The absorption spectra of pure C_6H_2Pc film and C_6H_2Pc/PbS nanocomposite. The spectra of both materials were reproducible.

6.1.2 Absorption spectrum of PbS QDs

Having known the absorbance of C_6H_2Pc film, the PbS absorbance is estimated by subtracting the absorbance of C_6H_2Pc from that of the nanocomposite. It should be noted that according to the Bear law, the absorbance depends on the concentration of the absorbing material. Therefore for a correct subtraction, the concentration of C_6H_2Pc should be almost the same in both films, i.e. the nanocomposite and pure C_6H_2Pc. The solutions used for the film deposition of C_6H_2Pc and C_6PbPc (precursor for the nanocomposite) were similar in terms of weight, 10 mg in 1 ml solvent. Since the molecular weight of C_6H_2Pc is about 0.85 of C_6PbPc, the concentration of C_6PbPc molecules is 0.85 times less than that of C_6H_2Pc molecules in the solution. Therefore, even if all C_6PbPc molecules are converted to C_6H_2Pc molecules during

gas treatment, the number of C_6H_2Pc molecules in the nanocomposite film would be 0.85 time less than that in the pure C_6H_2Pc. Accordingly, before performing the subtraction, the absorbance of pure C_6H_2Pc is scaled down by a factor of 0.85 to reach to almost the same concentration of C_6H_2Pc in the nanocomposite. The result of subtracting the pure C_6H_2Pc absorbance from that of the nanocomposite is presented in Figure 6.4. The absorption spectrum of pure C_6PbPc film (deposited from 10 mg/ml solution) is also included in the figure for the sake of comparison.

There are a few peaks in the subtracted spectrum, curve (d), that are consistent with the ones at C_6PbPc spectrum, such as peaks at about 780 and 480 nm. These peaks indicate the presence of few C_6PbPc molecules in the nanocomposite related to non-reacted C_6PbPc during gas treatment. There is a peak at around 600 nm where none of the C_6H_2Pc and C_6PbPc is absorbing. This peak is believed to be attributed to the first excitonic peak of the PbS QDs.

The subtracted spectrum shows an increasing trend from 600 nm toward shorter wavelengths as it is basically expected for the absorption spectrum after the first excitonic peak. As an example, the absorption spectrum of 4 nm PbS QDs in polymer (PVA) has been depicted in Figure 6.5, taken from [6]. As seen in the figure, the first excitonic peak of 4 nm PbS QDs is observed at around 580 nm, which is consistent with our analysis. It should be noted that the absorption spectra of QDs can be either with feature (i.e. with excitonic transition peaks) or featureless, depend mainly on the level of particle size distribution [6]. The appearance of the strong exciton feature in the absorption edge of the produced PbS QDs indicates the narrow size distribution of the PbS QDs in the nanocomposite film, stating another feature of this nanocomposite.

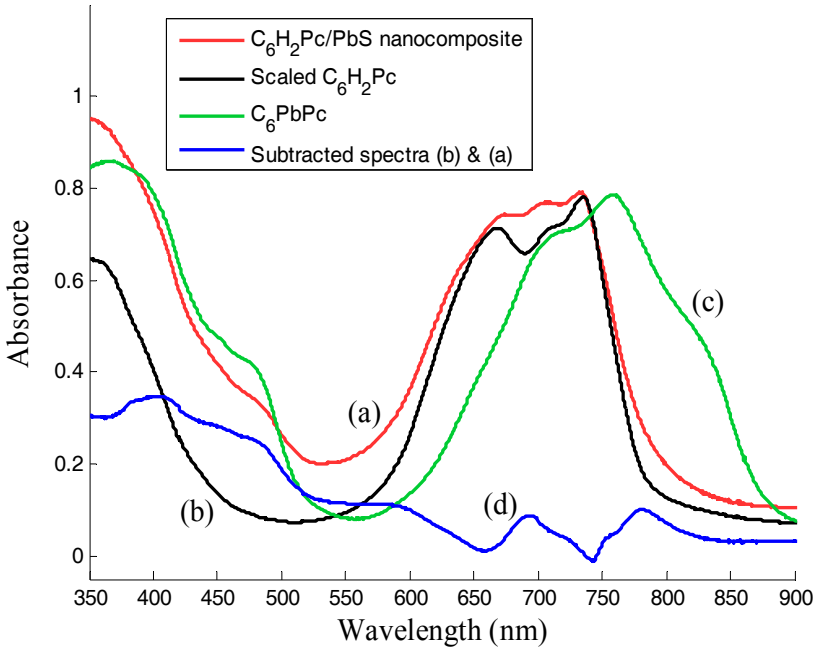

Figure 6.4 Optical absorbance spectra of: (a) C_6H_2Pc/PbS nanocomposite; (b) pure C_6H_2Pc scaled down by a factor of 0.85; (c) C_6PbPc film; and (d) the result of subtraction of curve (b) from curve (a).

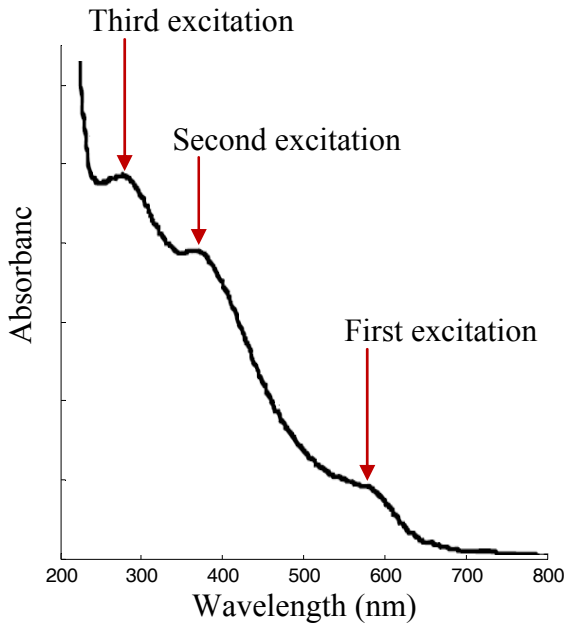

Figure 6.5 Absorbance spectrum of ~4 nm PbS QDs in polymer (PVA), taken from [6]. The first excitonic peak occurs at about 580 nm.

The onset of absorption spectrum of bulk PbS is around 3200 nm [77]. Comparing to bulk, the absorption spectrum of the PbS QDs shows a clear blue shift which is indicative of the band gap modification of the QDs due to the quantum confinement effect. The blue-shifted spectrum can be used as another evidence to verify the formation of PbS particles as small as quantum dots during the exposure of C_6PbPc film to H_2S gas.

6.2 PbS QDs band gap

The modified band gap of the PbS QDs can be calculated from the absorption spectrum. Basically, the first excitation occurs between the HOMO and LUMO energy levels and thus the photon energy at the first excitation is indicative of the energy gap between these levels. However, the presence of localised states, e.g. surface states, within the forbidden gap and/or the distribution of QDs size cause a broad excitonic peak instead of a sharp peak in the absorption spectrum [77]. In 1972, Tauc proposed a mathematical relation between the absorption tail and band gap of a material, expressed based on absorption coefficient α [163]:

$$\alpha_{\text{direct}} = \frac{C}{h\upsilon}\left(h\upsilon - E_g\right)^{1/2} \qquad \text{Direct band gap} \tag{6.5}$$

$$\alpha_{\text{indirect}} = \frac{C}{h\upsilon}\left(h\upsilon - E_g\right)^{2} \qquad \text{Indirect band gap} \tag{6.6}$$

where C is a constant, $h\upsilon$ is the photon energy and E_g is the band gap energy. Direct band gap refers to the excitation in which the momentum energy of electrons is unaffected by excitation from the valence to conduction band [24], while in the case of indirect band gap some parts of phonon energy are consumed to change the

momentum energy of the electrons. Tauc's law is widely used to calculate the band gap of materials, ranging from bulk to quantum dot size [77].

Lead sulphide is a direct band gap material [77] and Equation (6.5) is applied to calculate its band gap energy. Considering $A = \alpha d$, Equation (6.5) is rewritten as

$$(Ah\upsilon)^2 = C'\left(h\upsilon - E_g\right) \tag{6.7}$$

According to Equation (6.7), the band gap can be found from the x-intercept of the plot of $(Ah\upsilon)^2$ versus $h\upsilon$. The plot of $(Ah\upsilon)^2$ versus $h\upsilon$ for the obtained PbS QDs spectrum at the region 590 to 660 nm has been depicted in Figure 6.6. By fitting a straight line on the plot, the x-intercept and consequently the band gap of the PbS QDs is estimated to be 1.95 eV.

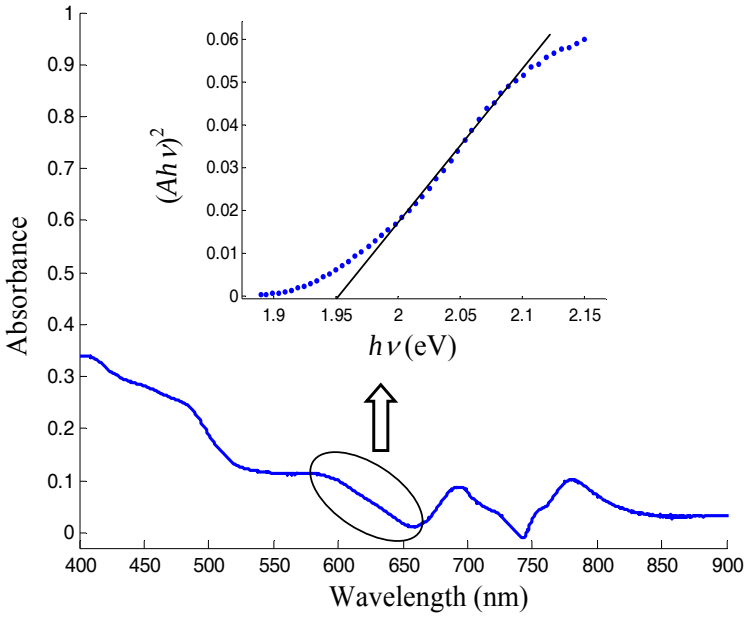

Figure 6.6 The subtracted absorbance spectrum of the nanocomposite from pure C_6H_2Pc, Curve (d) in Figure 6.4. The peak around 600 nm is attributed to the first excitonic peak of the PbS QDs. The inset shows the estimated band gap energy of the produced PbS QDs using the absorption tail and Tauc's law.

6.3 PbS QDs size

The average size of the PbS QDs has been estimated through the amount of change in the band gap energy compared to the bulk, using the effective mass approximation model as previously explained:

$$E_g^{\,Particle} - E_g^{\,bulk} = \frac{\hbar^2 \pi^2}{2R^2}\left(\frac{1}{m_e} + \frac{1}{m_h}\right) - \frac{1.8e^2}{\varepsilon R}. \qquad (6.8)$$

Having known the effective mass of electrons and holes in PbS crystal $m_e = m_h = 0.085m_0$ [77], where m_0 is the real mass of electrons, and $E_g^{\,bulk} = 0.41$ eV for bulk PbS [77], the average particles diameter is estimated to be about 3.7 nm. This value is in reasonable agreement with the ones obtained by other techniques, TEM (~4.5 nm) and XRD (~5.9 nm).

It is worth noting that most of researchers neglect the Coulomb term (the second term at the right-hand side of (6.8)) in the case of PbS QDs due to its rather small effect [77], although it is included here for a precise analysis.

6.4 Frontier energy levels of PbS QDs

The frontier energy levels, valence (HOMO) and conduction (LUMO) bands are almost equally shifted with respect to those of the bulk in the case of PbS QDs [78]. The reason is related to the nearly equal effective masses of holes and electrons in PbS, leading to almost equally share the confinement energy in the conduction and valence bands [78]. The equal effective mass results in the equal Bohr radius of holes and electrons, $a_{e,h} = \varepsilon \hbar^2 / \left(e^2 m_{e,h}\right)$, and thus the confinement dimension equally affects holes and electrons. The conduction and valence bands of bulk PbS were taken to have the energy value of about 4.55 and 4.96 eV respectively [164, 81], which means the bulk band gap is about 0.41 eV. Accordingly, the HOMO and

LUMO levels of the produced PbS QDs with the band gap of 1.95 eV are estimated to be about 5.73 and 3.78 eV, respectively. Figure 6.7 illustratively shows the shift in the energy level of the PbS QDs with respect to the bulk.

Having knowledge about the energy level of HOMO and LUMO is helpful to find out any possible mismatch between energy levels of the QDs and the matrix. The desirable unbalance between energy levels of a nanocomposite components has a significant impact on the electrical and optoelectrical properties of the nanocomposite, as already explained [122].

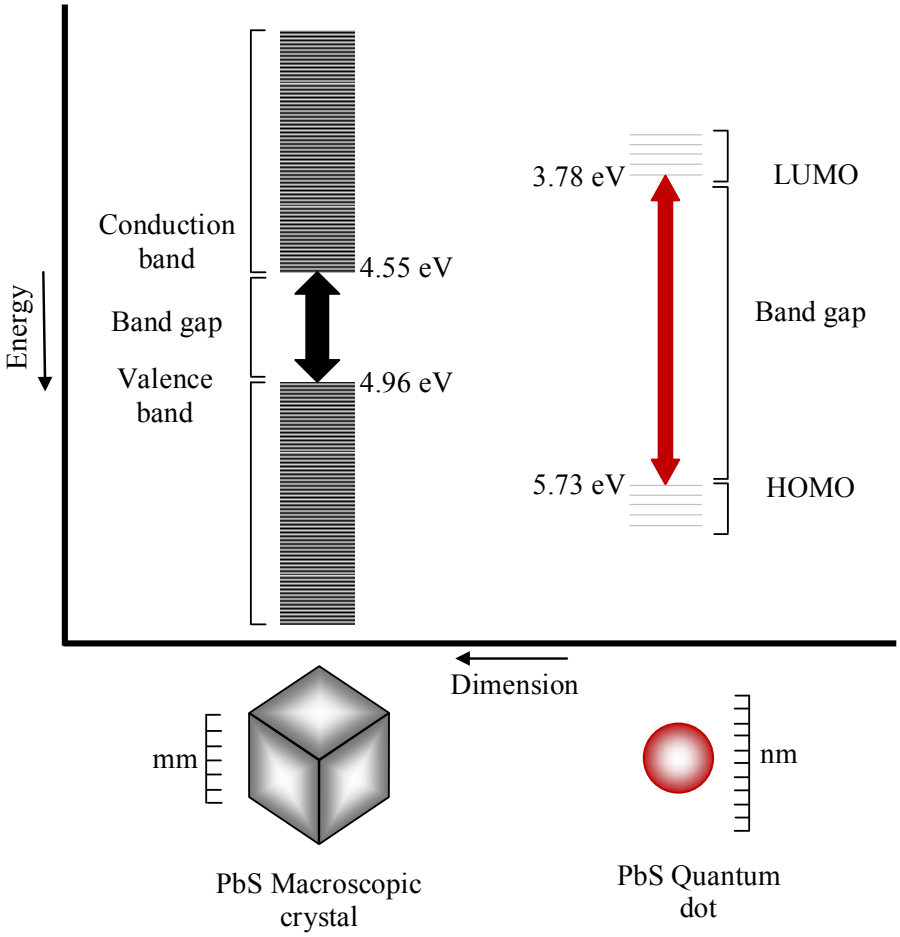

Figure 6.7 Illustrative representation of the quantum confinement effect and the estimated increase in the band gap of the produced PbS QDs. The frontier energy levels of PbS QDs shift equally with respect to those of the bulk.

CHAPTER 7

Steady-State Electrical Characterisation

7.1 Electrical conduction

The steady-state electrical characteristic of the nanocomposite in the sandwich structure device at room temperature has been depicted in Figure 7.1. The behaviour of the current density $(J = I/A)$ in response to the positive and negative bias is almost symmetric; rectification ratio is close to unity. This fact implies that ITO and Al electrodes make contacts with almost similar charge-injecting properties at the interface with the nanocomposite. A similar symmetric behaviour is observed for the steady-state electrical response of C_6H_2Pc sandwich structure device, as shown in Figure 7.1. All the analyses will then be presented for the positive bias. The type of contacts is ohmic for both devices. This fact is determined from the plot of current density *(J)* against electric field (*F*) on log scale, shown in Figure 7.2.

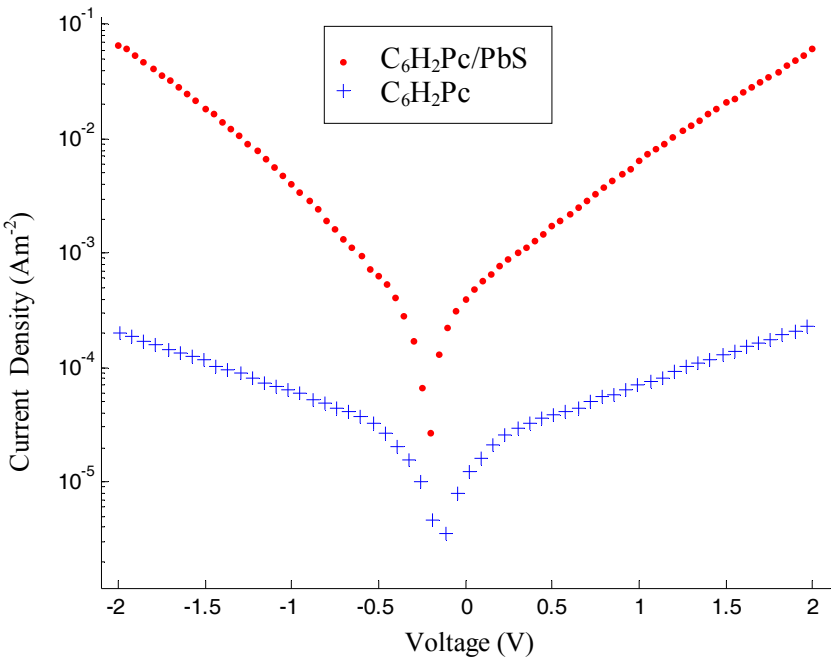

Figure 7.1 Steady-state electrical characteristic of sandwich structure devices at voltage sweeping from -2 V to +2 V.

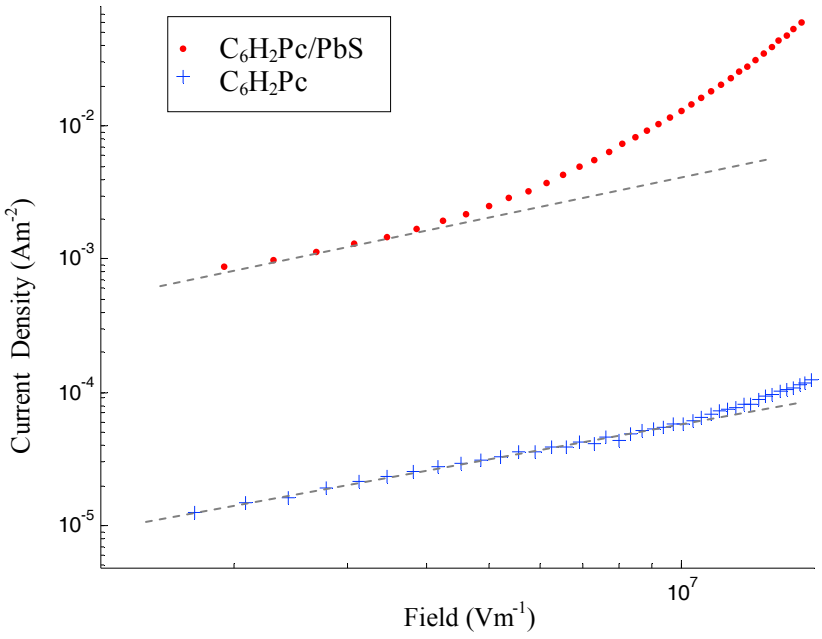

Figure 7.2 Steady-state electrical characteristic of sandwich structure devices on log-log scale. The dashed lines show the unity slope of the ohmic regions.

According to the plot, two distinct conduction mechanisms appear to exist depending upon the magnitude of the applied field. The dependence of J on F in the nanocomposite is linear at the fields below $4\times10^{6}\ \mathrm{Vm}^{-1}$, while the superlinear behaviour is observed above this field. The linear relation of *J–F* is evident from the unity slope of *J-F* plot in log scale showing the contacts are ohmic. The ohmic region is observed in both devices indicating the inclusion of the PbS QDs has no effect on the type of contacts formed at the interfaces.

The energy level diagram of the nanocomposite is shown in Figure 7.3. The values in the figure are based on the frontier energy levels of the PbS QDs obtained in Chapter 6 (HOMO=5.73 eV and LUMO=3.78 eV), and the reported energy levels for metal-free phthalocyanine in the literature, that are about HOMO=5.15 eV and LUMO=2.95 eV [165]. ITO has a high work function, 4.5-4.78 eV [166], which is close the HOMO level of organic compounds and typically makes an ohmic contact (for holes) with p-type organic semiconductors, including phthalocyanine compounds. But, the work function of Al, 4.06-4.28 eV [167], is low and theoretically is not expected to make an ohmic contact with metal-free phthalocyanines which has HOMO energy of 5.15 eV. There are two possible reasons for the formation of a hole-injecting contact at the Al interface: first, the formation of interfacial dipoles , which alters the energy gap between the work function of Al and Fermi level of C_6H_2Pc at the interface [26]; second the oxidation of Al during deposition process and the subsequent formation of a thin Al_2O_3 layer between Al and C_6H_2Pc. The thin Al_2O_3 layer empirically shows an increase in the rate of hole injection into the bulk [168].

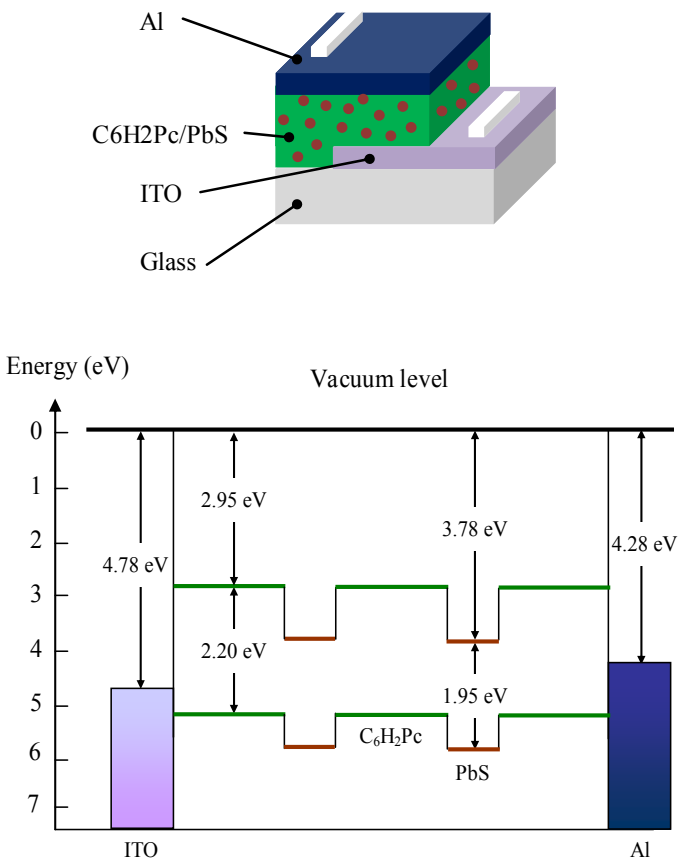

Figure 7.3 Energy level diagram of C_6H_2Pc/PbS nanocomposite sandwiched between ITO and Al electrodes. Formation of ohmic contacts for holes has been determined for both ITO and Al junctions, although based on MS theory a hole barrier is expected for Al electrode.

Based on Ohm's law, $J = \sigma F$, the conductivities of the nanocomposite, σ_{DC}^{NC}, and pure C_6H_2Pc, σ_{DC}^{Pc}, in the linear region are calculated to be around 3.1×10^{-10} and 6.0×10^{-12} $(\Omega m)^{-1}$, respectively. As evident, the incorporation of the PbS QDs enhances the dark conductivity of the nanocomposite by near two orders of magnitude, compared to pure C_6H_2Pc host matrix. The conductivity of the nanocomposite may be expressed in the form: $\sigma^{NC} = eN^{NC}\mu^{NC}$, where e is the

electrical charge of an electron, N^{NC} is the density of charge carries participating in the conduction process and μ^{NC} is the mobility of charges in the nanocomposite. The increase in the ohmic conductivity can be due to an increase in either the mobility or charge carrier density. Typically the main reason that may increase the mobility is the formation of conductive pathway by nanoparticles within the matrix. The percolation limit can be reached only in the case of high concentration nanoparticles (usually higher than 15 -20% [63]). The maximum volume fraction of the PbS QDs is about 3% implying that there is very low possibility for the formation of a conductive pathway by the PbS QDs.

There are some sources that may increase the charge density by inclusion of the PbS QDs into the matrix. Generally the density of intrinsic carriers (thermally generated carriers across the band gap) in organic semiconductors is low, in the range of $10^{9} - 10^{13}$ m^{-3} [2]. But, the inclusion of purposely-added and/or adventitious dopants, e.g. chemical impurities, significantly increases the density of carriers, around $10^{15} - 10^{20}$ m^{-3} in molecular organic semiconductors [2]. These localised states are usually preferential electron trapping in organic semiconductors leading to make p-type semiconductors [2]. The inclusion of the PbS QDs in C_6H_2Pc may increase the number of preferential electron trapping in the matrix. In addition, the possible morphological defects introduced into the matrix and/or high density of QDs surface states may be the other sources of increase in the charge density. The increase in the conductivity can boost the performance of electronic and optoelectronic devices as has been reported for a number of organic devices such as organic light emitting diodes [169].

7.2 Temperature-dependence

Temperature-dependence of electrical conduction of the sandwich structure devices has been obtained at temperatures ranging between 100 K and 293 K. The conductivity of both materials at the ohmic region is calculated at different temperatures and presented in Table 7.1. Figure 7.4 shows the temperature-dependence of σ_{DC}^{Pc} and σ_{DC}^{NC} based on the well-known Arrhenius plot**,** $\ln\sigma$ versus T^{-1}. Two separate regions are observed in the both Arrhenius plots suggesting different conduction processes are dominant at different temperature regions. The charge transport in C_6H_2Pc and C_6H_2Pc/PbS nanocomposite is believed to be by hopping mechanism. This fact is determined from the low value of the estimated mobility as well as the morphological study. According to XRD results, both the nanocomposite and pure C_6H_2Pc film are polycrystalline and thus the possibility of formation even narrow conduction band is very low. On the other hand, using the conductivity equation ($\sigma = eN\mu$ **)**, the mobility of C_6H_2Pc is estimated to be in the range of $10^{-9} - 10^{-11}$ $m^2V^{-1}s^{-1}$ by considering N to be about $10^{16} - 10^{18}$ m^{-3}. The considered value of N falls in the widely reported range for the concentration of thermally generated carriers (holes) of phthalocyanine compounds [50]. A common rule of thumb suggests that the mobility lower than 10^{-4} $m^2V^{-1}s^{-1}$ is indicative of charge transport based on hopping conduction rather than band conduction [50]. The conduction process, therefore, is believed to be hopping mechanism in C_6H_2Pc and also in the nanocomposite. The hopping conduction is the main characteristic of organic disordered semiconductors. The conduction process in disordered materials is mainly expressed as [38]

$$\sigma_{DC} = \sigma_0 \exp(-\frac{\Delta E}{kT})^{\beta} \qquad (7.1)$$

Table 7.1 Conductivity of C_6H_2Pc and C_6H_2Pc/PbS nanocomposite at different temperatures.

Temperature (K)	σ_{DC}^{Pc} $(\Omega m)^{-1}$	σ_{DC}^{NC} $(\Omega m)^{-1}$
293	6.0×10^{-12}	3.1×10^{-10}
265	1.8×10^{-13}	6.2×10^{-11}
240	4.0×10^{-14}	1.8×10^{-11}
200	2.0×10^{-14}	3.1×10^{-12}
150	1.8×10^{-14}	2.3×10^{-12}
100	1.4×10^{-14}	1.6×10^{-12}

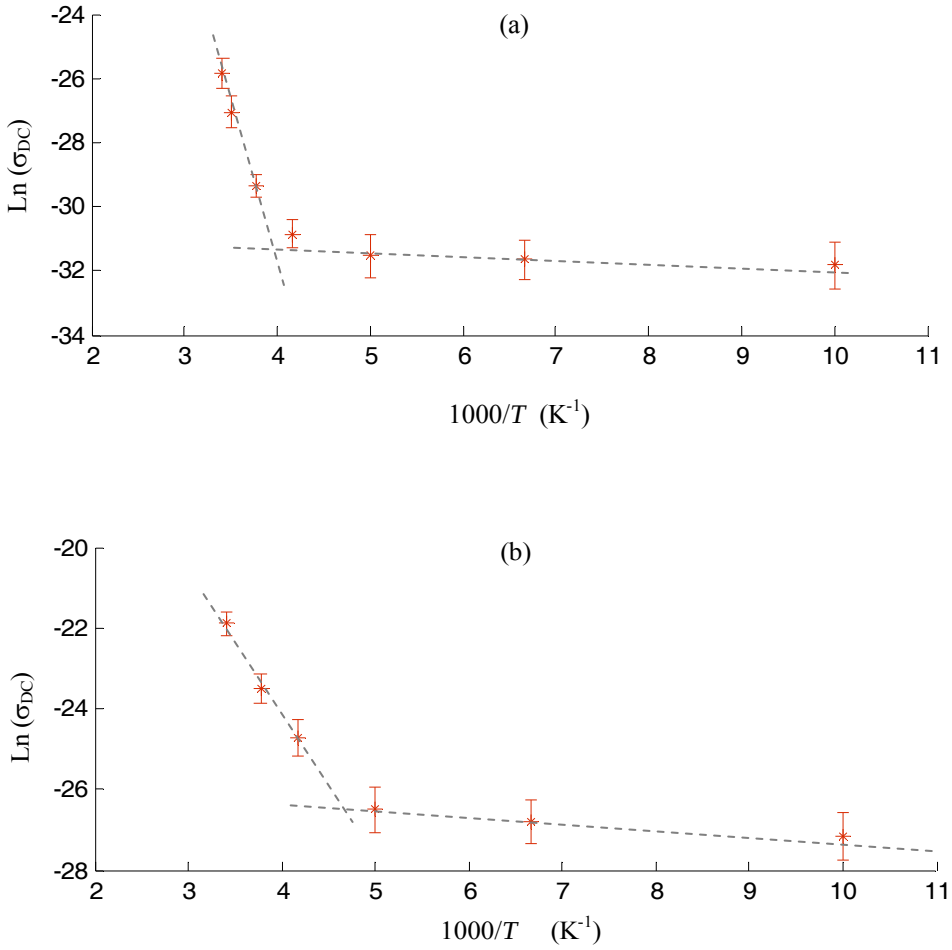

Figure 7.4 Temperature-dependence of (a) pure C_6H_2Pc and (b) C_6H_2Pc/PbS nanocomposite conductivity based on the Arrhenius plot. Two distinct regions are observable in the plots indicating the dominance of different conduction processes in different temperature regions. The activation energy at each region is determined from the slope of the fitted straight lines (dashed line) on the graphs. The experiment has been repeated five times and the average at each temperature is shown by an asterisk and deviation from average by an error-bar.

where σ_0 is pre-exponential factor and ΔE is the activation energy. The value of β is ranging from 1/4 to 2 depending on the materials and in some cases temperature. For example, in one of the well-known hopping mechanism, called variable range hopping model, $\beta = 1/3$ [170] and $\beta = 1/4$ [171] for two-dimensional (very thin film) and three-dimensional systems, respectively. In organic disordered semiconductors $\beta = 2$ has been observed and theoretically proved [15], although empirically other values of β have also been reported in organic disorder semiconductors [147, 38].

Referring to Figure 7.4, linear behaviour is observed in both temperature regions of the Arrhenius plots, i.e. T>240 and T<240 K, indicating β=1 and the conduction processes are thermally activated. The activation energy is calculated from the slope of the linear region and found to be about 0.820 eV and 0.320 eV, respectively, for C_6H_2Pc and the nanocomposite at T>240 K. These observations show that the incorporation of the PbS QDs decreases the activation energy by almost 0.5 eV at temperature range T>240 K. By fitting a straight line on each set of data at T<240 K, the activation energy at this region is also calculated to be 0.006 eV and 0.011 eV for C_6H_2Pc and the nanocomposite, respectively. The obtained activation energies are lower than kT (~0.025 eV at room temperature) suggesting the conduction process at T<240 K is unlikely to be thermally activated process.

7.3 High-field conduction mechanism

By increasing the field, the slope of *J-F* plot shown in Figure 7.2, exceeds unity indicating the onset of high-field effects on the conduction mechanism. There is a well-defined field, F_t, for transition from ohmic to superlinear behaviour which is

around 10^7 Vm^{-1} for C_6H_2Pc device at room temperature. The presence of the PbS QDs in the nanocomposite device shifts the transition field to a lower value, 4×10^6 Vm^{-1} at room temperature.

It should be noted that the applied field should not exceed 5×10^7 Vm^{-1} due to bistable conduction behaviour of the devices, in which the devices suddenly switch to higher-value conductivity (by a few orders of magnitude) at field around 5×10^7 Vm^{-1}. All the analyses correspond to the device electrical behaviour before the sudden switching.

The presence of ohmic contact at the interfaces suggests that the charge transport in the devices is not affected by the junctions and thus the high-field conduction mechanisms should be among the bulk-limited mechanisms. The Poole-Frenkel (PF) mechanism is found not to be well-fitted with *J-F* behaviour of C_6H_2Pc device. The validity of the one-dimensional Poole-Frenkel mechanism is checked by the plot of $\ln(\sigma_{DC})$ against $F^{1/2}$, which should be a straight line with the slope of β_{PF}/kT, according to the Poole-Frenkel equation (Equation (2.11)). Figure 7.5 depicts the plot of $\ln(\sigma_{DC}^{Pc})$ versus $F^{1/2}$ for C_6H_2Pc device, where the conductivity at each voltage is found by $\sigma_{DC} = Jd/V$. By fitting straight lines to the plot at the high-field region, the value of β_{PF} and then dielectric constant, ε, is calculated and found not to be consistent with the value expected for C_6H_2Pc. The high-frequency dielectric constant of C_6H_2Pc is found to be around 5, as will be presented in the next chapter, while the calculated ε from the plot is about 48 at room temperature which is ~10 times larger than that of C_6H_2Pc, and varies in the range of $30 < \varepsilon < 60$ by lowering temperature. The 1D PF mechanism, therefore, cannot be responsible for the field-dependent conduction mechanism of C_6H_2Pc device. A similar result is obtained for

the three-dimensional PF mechanism. The 3D PF mechanism, Equation (2.14), is hardly fitted to the experimental results and the value of β_{PF} and from that the value of ε is estimated which varies in the range of $13 < \varepsilon < 34$. This range is still far from the real value of ε in C_6H_2Pc.

Typically, the common high-field conduction mechanism in phthalocyanine compounds is the space-charge limited current (SCLC) if the junction contact is ohmic [50]. As evident from the *J-F* plot in log scale, Figure 7.6, a straight line can

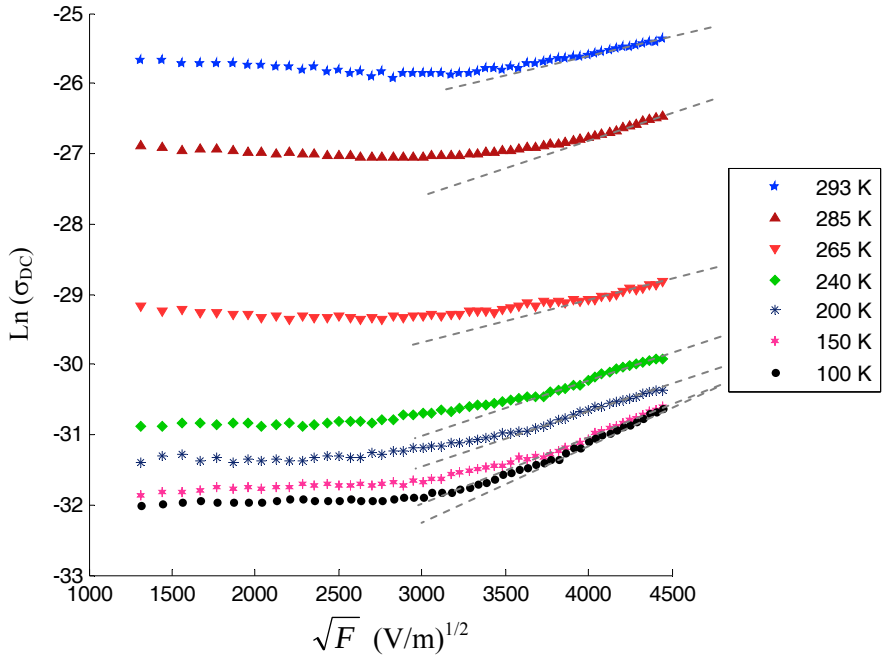

Figure 7.5 Plot of $\mathrm{Ln}(\sigma_{DC})$ versus $F^{1/2}$ corresponding to C_6H_2Pc device. The dashed lines show the linear-dependence of the graph at regions with high field effect. In the case of the Poole-Frenkel mechanism, the slopes of these lines determine the value of the field lowering coefficient of the Poole-Frenkel mechanism.

be fitted to the plot at superlinear region with the slope ranging from 1.9 to 3.1 by lowering temperature from 293 K to 100 K. This behaviour seems to follow the power-law, $J \propto V^{l+1}$, which is predicted by the SCLC mechanism with an exponential trap distribution, Equation (2.6). The SCLC mechanism with exponential trap distribution is indicative of conduction mechanism in which the injected charges fill the traps which are exponentially distributed within the forbidden gap. In this model the exponent *l* is inversely proportional to temperature, $l = T_0/T$ **,** where T_0 is characteristic temperature corresponds to exponential trap distribution. So to examine the consistency of the *J-F* behaviour with the SCLC mechanism, the plot of l against $1/T$ should be a straight line with the slope equal to T_0. As shown in Figure 7.7, two straight lines can be fitted to the plot of l versus $1/T$: one for temperatures higher than 240 K that results in $T_0 = 847$ K; and the other for temperatures below 240 K yields $T_0 = 94$ K. The value of T_0 is expected to be in the range of 548-1823 K for phthalocyanine compounds [50]. The value of $T_0 = 847$ K falls in this range indicating the possible consistency of conduction mechanism with the SCLC at *T*>240 K. However, there is still a doubt since the straight line does not pass through the origin as theoretically expected. This discrepancy suggests that while the SCLC mechanism may be the dominant conduction process for higher temperature range, the behaviour of C_6H_2Pc does not agree with the ideal SCLC equation. In fact the conventional SCLC equation is based on the band conduction process considering field-independent mobility, while in C_6H_2Pc the conduction is believed to be by hopping mechanism which is highly field-dependent causing the deviation of the high-field results from the ideal SCLC equation [172, 173].

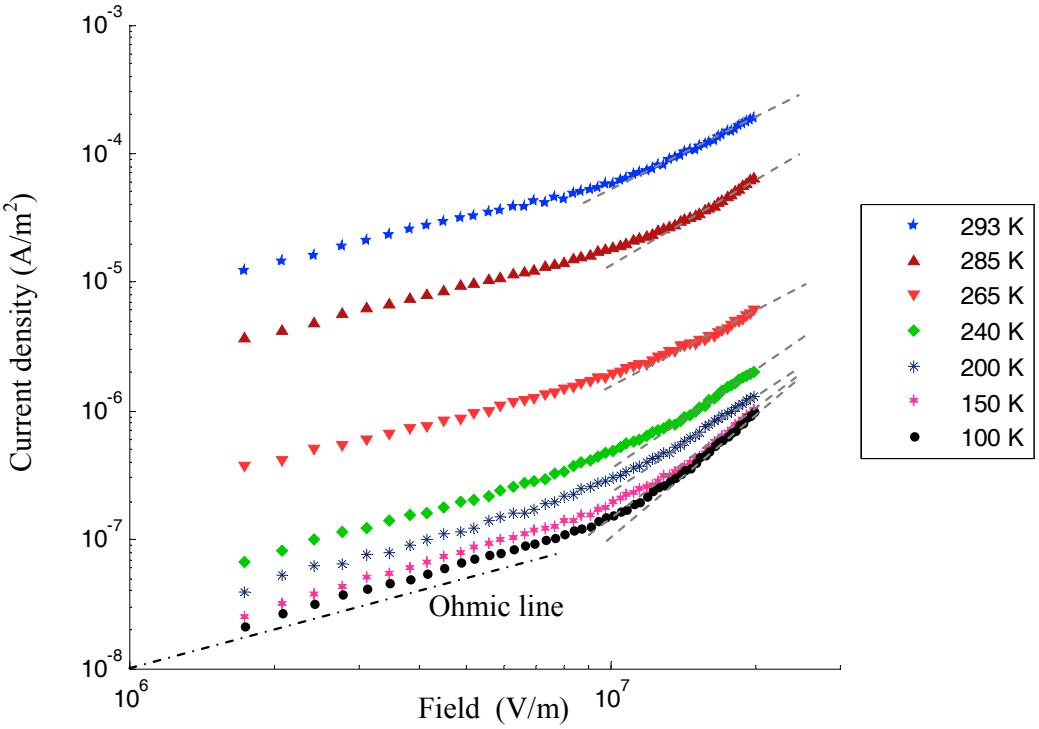

Figure 7.6 *J-F* characteristic of C_6H_2Pc device in log scale. The slopes of the fitted straight lines increase by lowering temperature.

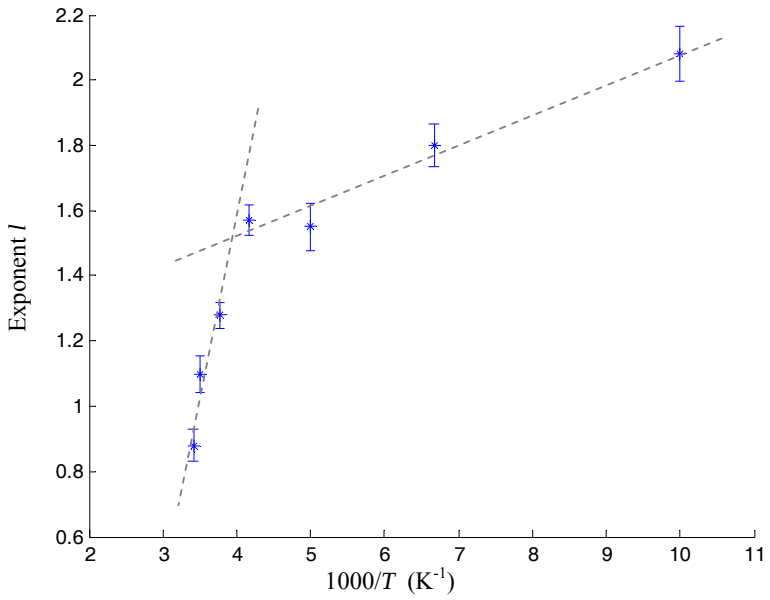

Figure 7.7 Plot of exponent *l* vs. reciprocal temperature for C_6H_2Pc. The characteristic temperature, T_0, corresponding to exponential trap distribution is determined from the slope of the fitted line. The experiment has been repeated five times and the average at each temperature is shown by an asterisk and deviation from average by an error-bar.

The possibility of the SCLC mechanism is examined for the nanocomposite device. As shown in Figure 7.8, the straight lines are closely fitted to the log-log plot of *J-F* at fields higher than F_t, indicating the power-law relation between *J* and *F*. The value of exponent *l*+1 varies between 3.14 and 5.16 by cooling down temperature from 293 K to 100 K. These values are higher than the ones obtained for C_6H_2Pc device showing the stronger effect of field on the nanocomposite devices. Similar to C_6H_2Pc device, two straight lines are fitted to the average values in the plot of *l* versus 1/*T* at different temperature regions, however none of them passes through origin, as shown in Figure 7.9. The slope of these lines yields the value of T_0 equal to 1776 and 113 K at *T*>240 K and *T*<240 K, respectively. With no previous reported value of T_0 for C_6H_2Pc/PbS nanocomposite, it is difficult to comment whether the SCLC is dominant conduction mechanism in the nanocomposite.

The *J-F* behaviour of the nanocomposite device is found to be consistent with the Poole-Frenkel mechanism. The plot of $\ln(\sigma_{DC}^{NC})$ versus $F^{1/2}$, Figure 7.10, shows a linear trend at higher field region, where the slope of the fitted line determines the value of the dielectric constant to be around 5 at room temperature. The value of dielectric constant varies in the range of 5 ± 1 by lowering temperature. This range is in good agreement with the value expected for the dielectric constant of the nanocomposite which is about 6.2, obtained from the high frequency response of the nanocomposite device (presented in the next chapter). This observation suggests that the *J-F* behaviour of the nanocomposite device at higher field region can be well-described by the one-dimensional PF mechanism. The validity of the three-dimensional PF mechanism is also examined by fitting data which yields the optical dielectric constant in the range of 2.1 ± 0.7. The real value of optical dielectric constant is closer to the obtained range by 1D PF analysis rather than 3D PF.

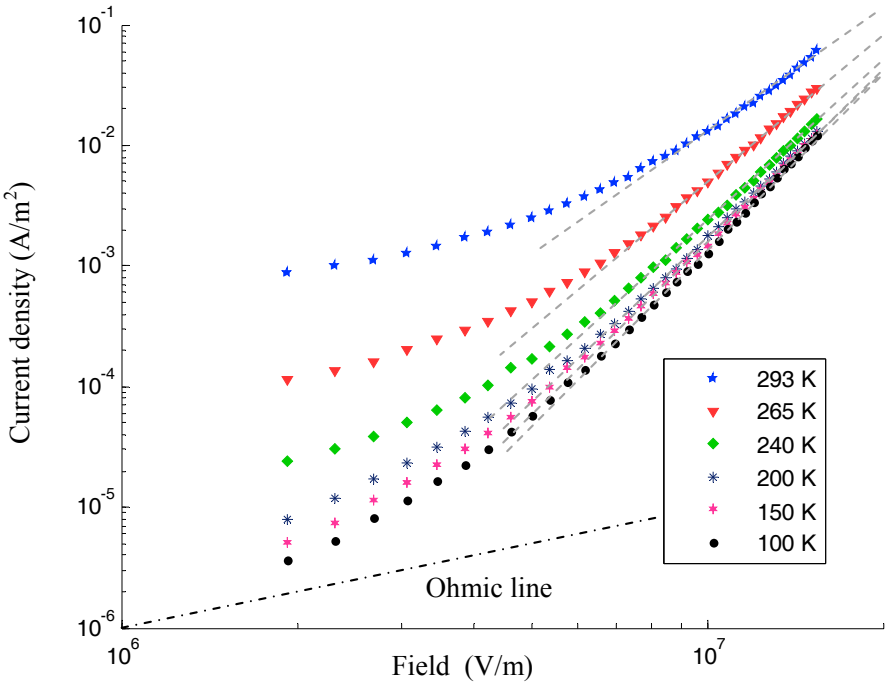

Figure 7.8 *J-F* characteristic of C_6H_2Pc/PbS device in log scale. The slopes of the fitted straight lines increase by lowering temperature.

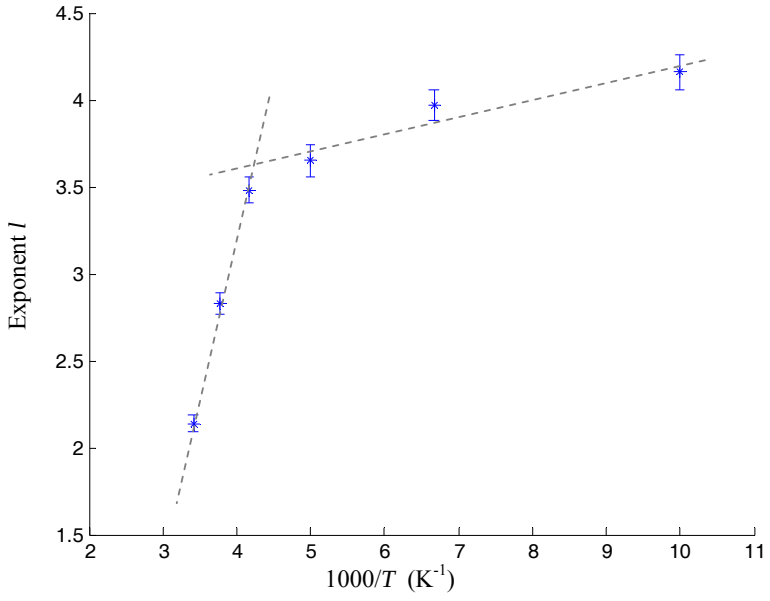

Figure 7.9 Plot of exponent *l* vs. reciprocal temperature for C_6H_2Pc/PbS device. The characteristic temperature, T_0, corresponding to exponential trap distribution is determined from the slope of the fitted line. The experiment has been repeated five times and the average at each temperature is shown by an asterisk and deviation from average by an error-bar.

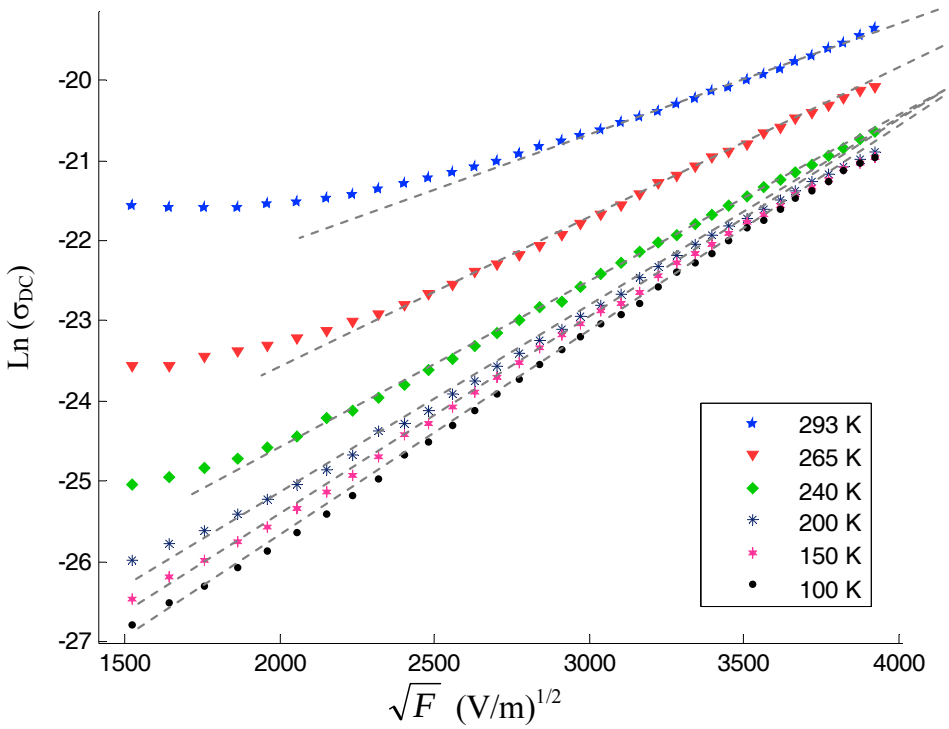

Figure 7.10 Plot of $\mathrm{Ln}\,(\sigma_{DC})$ versus $F^{1/2}$ corresponding to C_6H_2Pc/PbS device. The dashed lines show the linear-dependence of the graph at regions with high field effect. The field lowering coefficient of the Poole-Frenkel mechanism can be calculated from the slope of these lines.

The dominance of PF mechanism refers to the presence of charged localised states in the nanocomposite. One possibility of such states is charged surface states on the QDs. Generally quantum dots have large density of surface states such as dangling bonds [11]. PbS QDs can have either S dangling bonds or Pb dangling bonds, which are respectively acting as acceptor-like or donor-like centres [174]. It was observed that producing PbS QDs in excess of sulphur precursor reduces the possibility of Pb dangling bonds [174]. If this case happens during the H_2S exposure, S dangling bonds are formed on the PbS QDs surface. These charged localised states act as acceptor-like centres and be able to release their holes at high electric fields, and thus can justify the dominance of the Poole-Frenkel conduction mechanism in the nanocomposites.

CHAPTER 8

Impedance Spectroscopy

8.1 Experimental observations

The real and imaginary parts of admittance, Y' and Y'' respectively, are obtained by applying an alternating field to the sandwich structure devices:

$$Y = Y' + iY'' \tag{8.1}$$

Having known the geometry of the devices, the AC conductivity is then calculated from the real part of admittance which is known as conductance

$$\sigma_{AC} = \frac{d}{A} Y' \tag{8.2}$$

where d is the thickness of the films, $d^{Pc} = 100$ nm and $d^{NC} = 130$ nm, and A is the effective area of the devices $A = 4.5$ mm^2. Note that for the sake of brevity the notion "AC conductivity" is simply used for the real part of complex AC conductivity. Recall that the superscripts Pc and NC are used for the quantities

corresponding to C_6H_2Pc and the nanocomposite, respectively. The frequency-dependence of the conductivity in both C_6H_2Pc and C_6H_2Pc/PbS devices is shown in Figure 8.1. The measured conductivity may consist of both AC conductivity (σ_{AC}) and DC conductivity (σ_{DC}), i.e.

$$\sigma(\omega,T)=\sigma_{AC}(\omega,T)+\sigma_{DC}(T), \tag{8.3}$$

provided that $\sigma_{AC}(\omega,T)$ and $\sigma_{DC}(T)$ are originated from different processes. If $\sigma_{AC}(\omega,T)$ and $\sigma_{DC}(T)$ have similar process, i.e. $\sigma_{DC}(T)=\lim_{\omega\to 0}\sigma_{AC}(\omega,T)$, then Equation (8.3) is no longer used [39]. In both devices, the DC conductivity, as obtained in the previous chapter, is found to be negligible compared to the total measured conductivity. Therefore without loss of accuracy, the measured conductivity can be considered to be AC conductivity. Figure 8.2 shows the comparison between the measured and DC conductivity at room temperature; the same deduction is reached for lower temperatures too.

As evident from Figure 8.1, the AC conductivity of the nanocomposite device is higher than that of C_6H_2Pc device by about two orders of magnitude. However, the behaviour of AC conductivity with respect to frequency and temperature are almost similar in both devices as summarised below:

(I) $\sigma_{AC}(\omega,T)$ increases monotonically by increasing frequency from 10^2 to 10^6 Hz.

(II) $\sigma_{AC}(\omega,T)$ is temperature-dependant and decreases by lowering temperature down to T=100 K.

(III) The temperature-dependence of $\sigma_{AC}(\omega,T)$ becomes weak as temperature decreases.

(IV) The slope of the AC conductivity graph against frequency (in log scale) is below unity at frequencies lower than 10^4 Hz and increases by decreasing temperature.

Most of these types of behaviour are commonly reported in disordered semiconductors [41] and the values of slope below unity indicate that the frequency-dependence of the conductivity of both devices can be well described by the universal power-law, i.e. $\sigma_{AC}(\omega,T) = a(T)\omega^{s(\omega,T)}$, mainly at frequencies lower than 10^4 Hz. As evident from Figure 8.1, the graphs can be approximately divided into low and high frequency regions corresponding respectively to below and above 10^4 Hz. On each graph, the values of slope s at $f < 10^4$ Hz are below unity, while they exceed unity at frequencies higher than 10^4 Hz. The values of s are tabulated in Tables 8.1 and 8.2 regarding C_6H_2Pc and the nanocomposite device, respectively. The super-linear frequency-dependence, especially in the case of $s \approx 2$, is mainly attributed to the presence of the lead resistance [39]. The validity of this claim is investigated in the next section by modelling the device using an equivalent circuit and then fitting the AC quantities of the circuit to their corresponding experimental data. The dominant AC conduction mechanism in the nanocomposite is then studied after correcting the effect of the lead resistance.

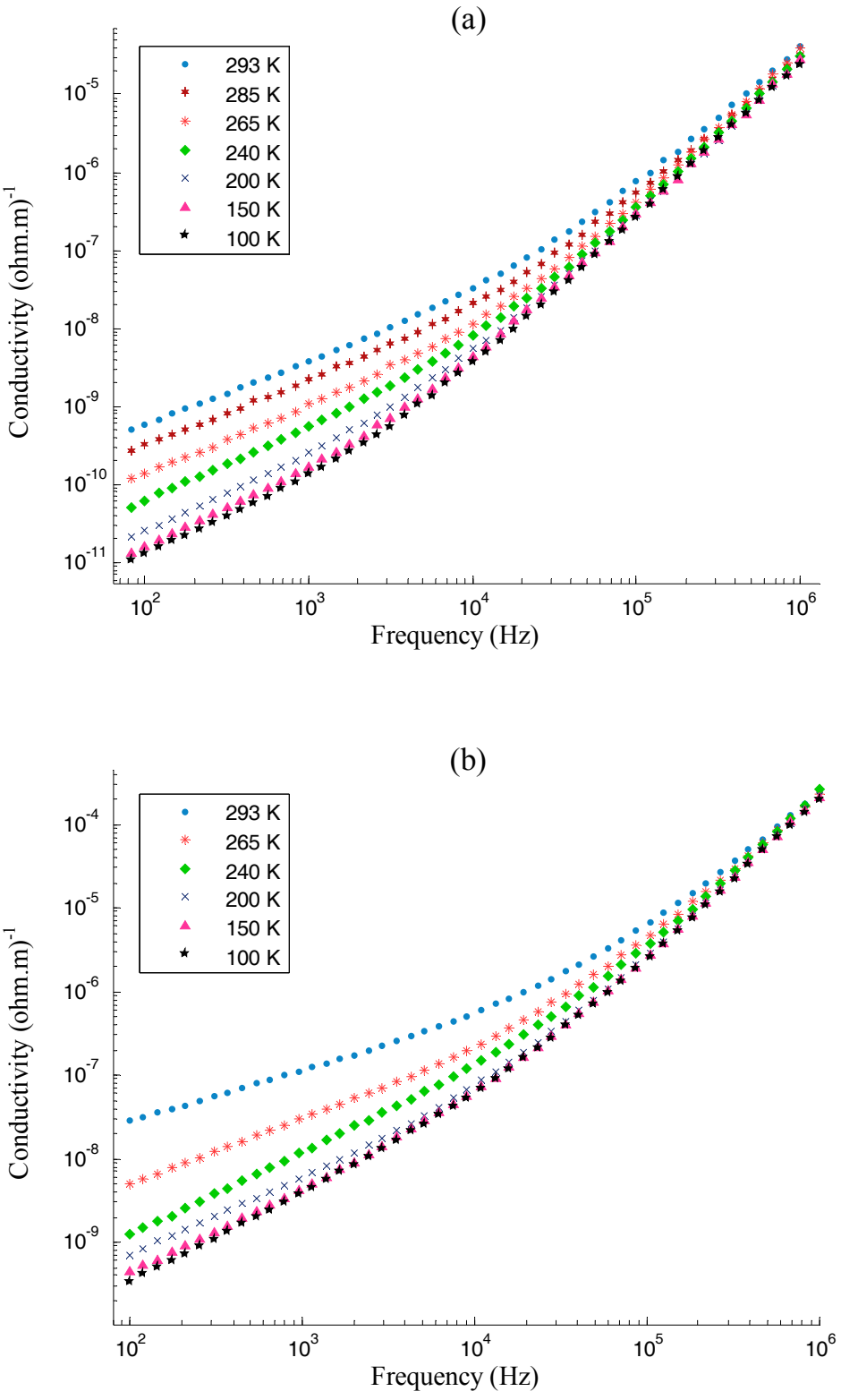

Figure 8.1 Frequency dispersion of (a) C_6H_2Pc and (b) C_6H_2Pc/PbS device conductivity at different temperatures.

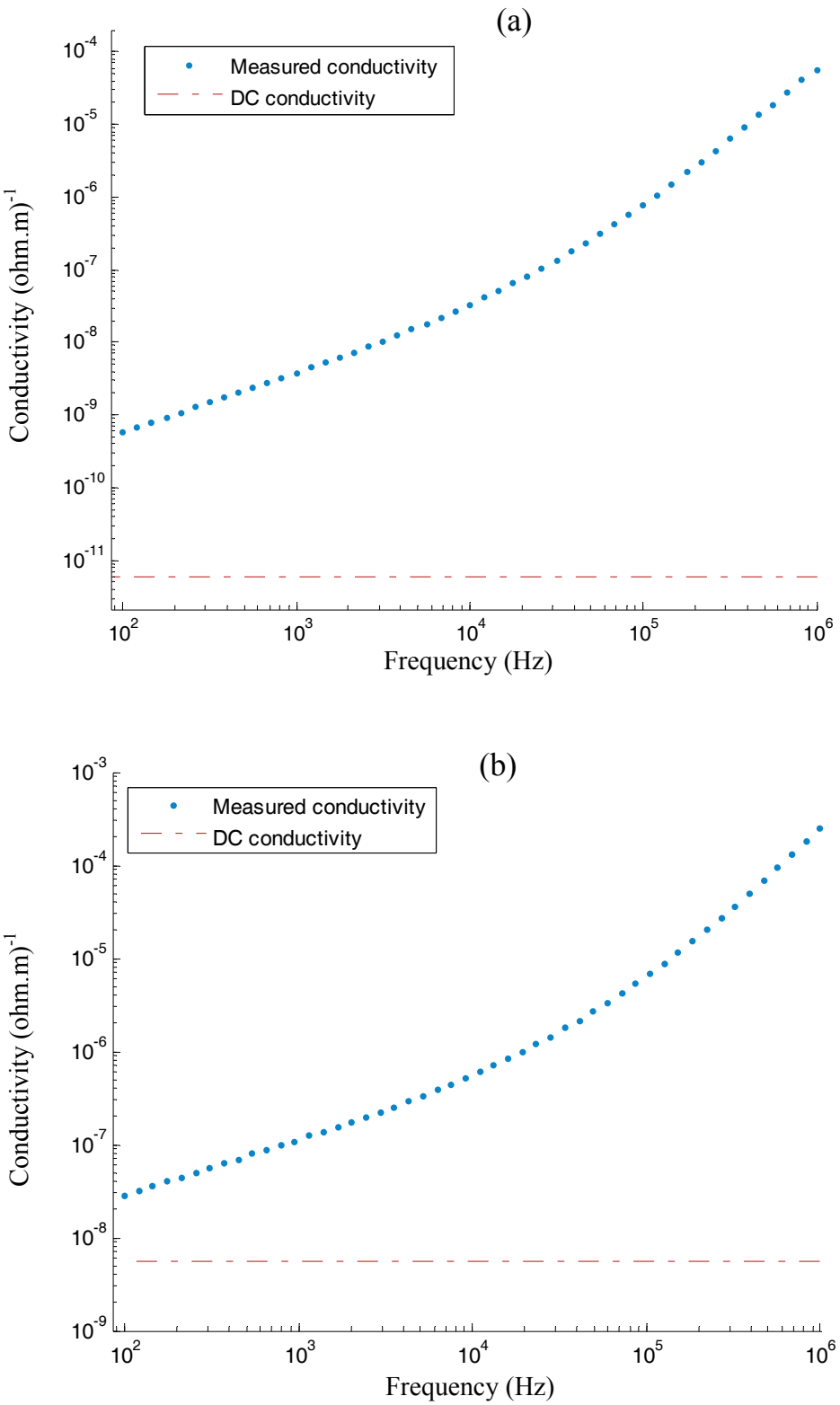

Figure 8.2 Comparing the DC conductivity with the total conductivity of (a) C_6H_2Pc and (b) C_6H_2Pc/PbS device. The total conductivity is the summation of both AC and DC conductivity. The obtained conductivity of both materials was reproducible.

Table 8.1 Slope of the AC conductivity graph of C_6H_2Pc device in both frequency regions. The error of the listed values is not more than 2%.

Temperature	Below 10^4 Hz	Above 10^4Hz
293 K	0.85	1.74
285 K	0.86	1.78
265 K	0.89	1.96
240 K	0.93	1.95
200 K	0.96	1.96
150 K	0.99	1.97
100 K	1.02	1.97

Table 8.2 Slope of the AC conductivity graph of C_6H_2Pc/PbS device in both frequency regions. The error of the listed values is not more than 2%.

Temperature	Below 10^4 Hz	Above 10^4 Hz
293 K	0.67	1.65
265 K	0.83	1.78
240 K	0.90	1.89
200 K	0.94	1.95
150 K	0.98	1.96
100 K	0.99	1.96

8.2 Correcting the effect of lead resistance

The effect of the lead resistance in a device behaviour can be determined by modelling the device via an equivalent circuit that consists of two regions of bulk and contact [39, 175]. The equivalent circuit consists of a parallel connection of R_b

and C_b, representing respectively the bulk resistance and capacitance, which is connected in series with R_c, representing the lead resistance, as illustrated in Figure 8.3. The lead resistance can be the resistance of the leads used to connect the devices to the measurement instrument and/or any undesirable contact between the metal electrode and the bulk material. Lakatos *et al.* [175] investigated the effect of the lead resistance on the conductance of a device, modelled by the circuit shown in Figure 8.3, where R_b is a frequency-independent element.

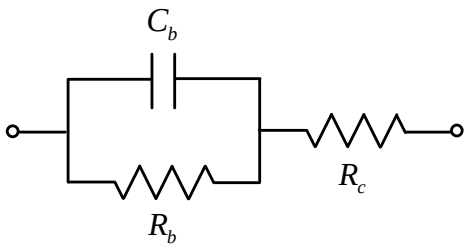

Figure 8.3 AC equivalent circuit of the devices. R_b, C_b and R_c representing, respectively, the bulk resistance, bulk capacitance and lead resistance.

However in this study, the circuit with a frequency-independent value of R_b could not replicate the experimental result of the devices. Therefore here, the bulk resistance is considered to be frequency-dependent defined by:

$$R_b(\omega) = \frac{1}{a\omega^s}\frac{d}{A} \tag{8.4}$$

Expression (8.4) is derived based on the experimental observation of the universal power-law behaviour in both devices. The values of s and a are considered those obtained experimentally by fitting a straight line on the plot of σ_{AC} vs. f in log scale (Figure 8.1) at frequencies lower than 10^4 Hz; s is the slope of the straight line (presented in Tables 8.1 and 8.2) and $\log(a)$ is its y-intercept. Note that the values of s are assumed to be frequency-independent. This assumption is not far from reality

since according to universal observation the value of s weakly depends on frequency and is usually considered to be frequency-independent [41, 39].

The real and imaginary parts of the equivalent circuit admittance are written respectively as:

$$Y' = \frac{\left[R_b(\omega) + R_c\right] + \left[\omega C_b R_b(\omega)\right]^2 R_c}{\left[R_b(\omega) + R_c\right]^2 + \left[\omega C_b R_b(\omega)\right]^2 {R_c}^2} \tag{8.5}$$

$$Y'' = \frac{\omega C_b {R_b}^2(\omega)}{\left[R_b(\omega) + R_c\right]^2 + \left[\omega C_b R_b(\omega)\right]^2 {R_c}^2} \tag{8.6}$$

where $R_b(\omega)$ is defined by expression (8.4). The accuracy of the equivalent circuit is validated by fitting the graphs of Y' and Y'' to their corresponding experimental data, by selecting appropriate values for the unknown quantities of R_c and C_b. The results of this fitting have been shown in Figures 8.4 and 8.5, and the obtained values of R_c and C_b have been tabulated in Tables 8.3 and 8.4, regarding C_6H_2Pc and the nanocomposite device, respectively. To further evaluate the proposed equivalent circuit, the admittance Cole-Cole plots of the devices are also included in Figures 8.4(c) and 8.5(c). As evident from the figures, the frequency response of the circuit is in good agreement with those of devices indicating the device behaviour can be described by the circuit with series lead resistance. It can be deduced that the deviation from the universal frequency response at frequencies higher than 10^4 Hz (up to 10^6 Hz) is attributed to the presence of the lead resistance.

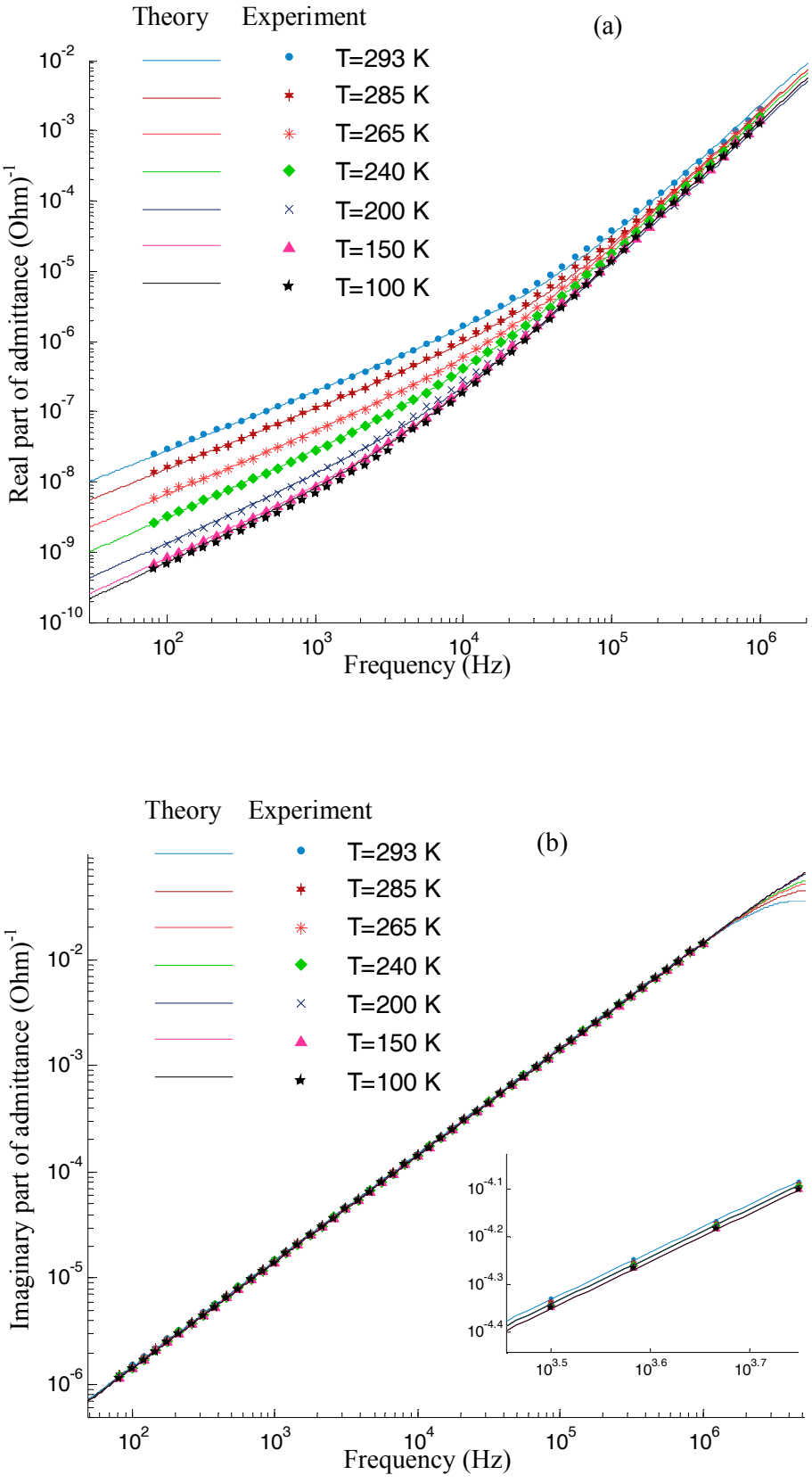

Figure 8.4 (a) The real part of admittance of C_6H_2Pc device. (b) The imaginary part of admittance of C_6H_2Pc device; the inset is a scaled view of the plot and has the same axis labels. (Continued)

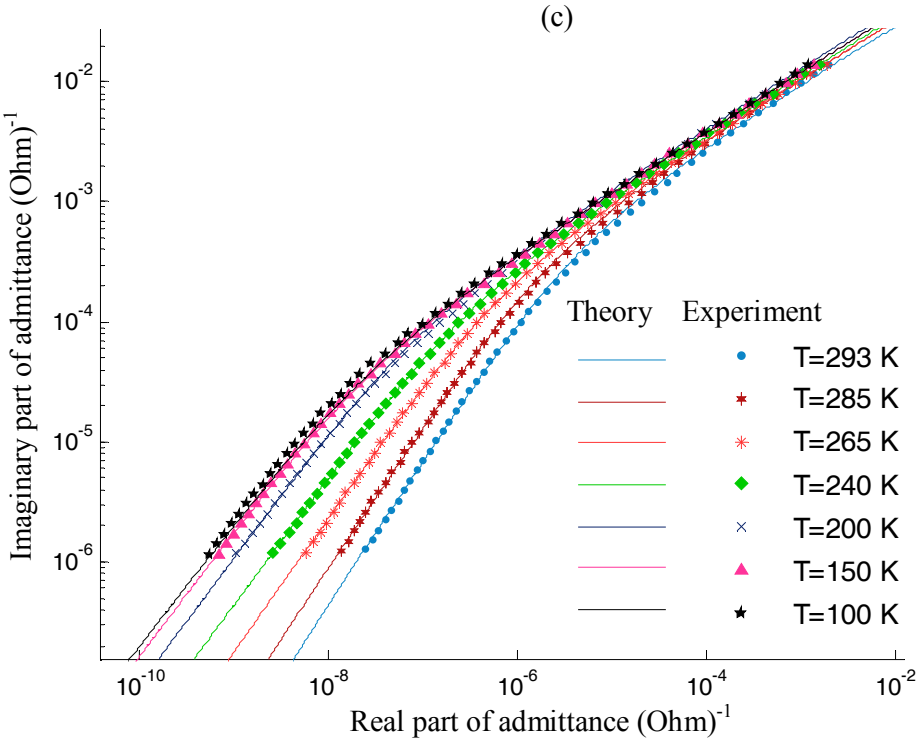

Figure 8.4 (c) The admittance Cole-Cole plot of C_6H_2Pc device.

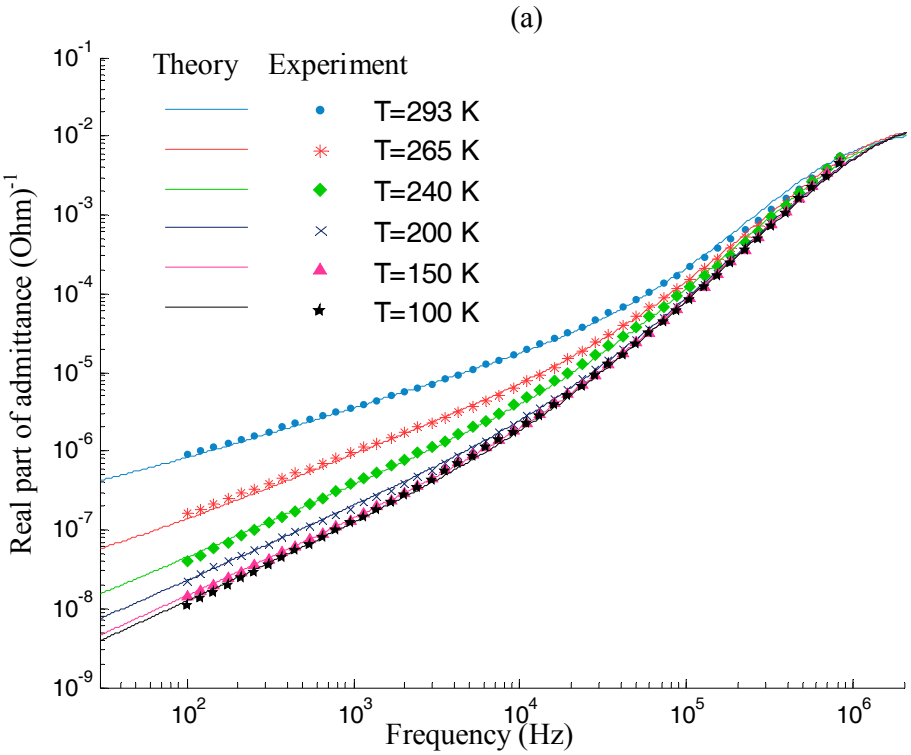

Figure 8.5 (a) The real part of admittance of C_6H_2Pc/PbS device. (Continued)

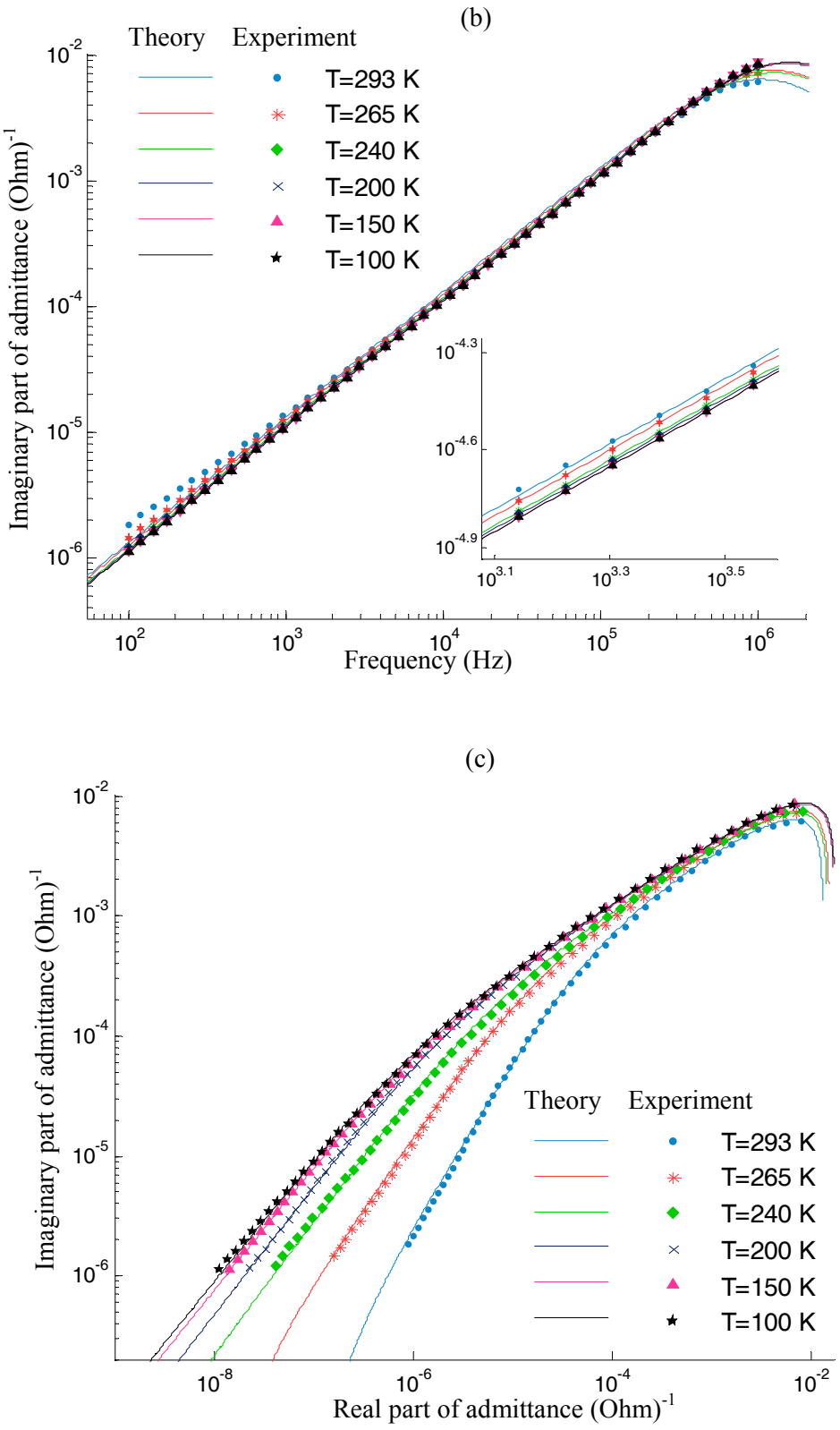

Figure 8.5 (b) The imaginary part of admittance of C_6H_2Pc/PbS device; the inset is a scaled view of the plot and has the same axis labels. (c) The admittance Cole-Cole plot of C_6H_2Pc/PbS device.

Table 8.3 Equivalent circuit parameters of C_6H_2Pc device.

Temperature	R_c^{Pc} (Ω)	C_b^{Pc} (nF)
293	11	2.344
285	9	2.291
265	9	2.291
240	8	2.291
200	6	2.291
150	7	2.239
100	7	2.239

Table 8.4 Equivalent circuit parameters of C_6H_2Pc/PbS device.

Temperature	R_c^{NC} (Ω)	C_b^{NC} (nF)
293	75	2.10
265	65	1.99
240	68	1.86
200	58	1.82
150	58	1.78
100	57	1.78

Alternatively the devices can be modelled by considering a constant R_c for all temperatures and tuning three other parameters, i.e. C_b, s and a, at each temperature. Since in this alternative approach, R_c is temperature-independent, the fitting process involves concurrent finding of the three temperature-dependent parameters at all temperatures as well as R_c. This issue complicates the fitting

process as the number of unknown parameters to be found is high compared to the proposed method.

8.3 AC conduction mechanism

To determine the dominant AC conduction mechanism, the frequency response of the materials without any interference of the lead resistance is analysed. According to the equivalent circuit, to correct the effect of lead resistance, it only requires considering the AC conductivity of the bulk region of the equivalent circuit, i.e.

$$\sigma_{AC} = \frac{d}{A}\frac{1}{R_b(\omega)} = a\omega^s \tag{8.7}$$

Figure 8.6 shows the frequency response of the AC conductivity of C_6H_2Pc, σ_{AC}^{Pc}, and the nanocomposite, σ_{AC}^{NC}, in comparison with the AC conductivity of the whole devices. The lead resistance mainly influences the device behaviour at frequencies higher than 10^4 Hz at room temperature. The effect of lead resistance starts at lower frequencies by lowering temperatures.

As mentioned in section 2.6, two probable models for AC conduction mechanism in the semiconductors following the universal power-law are the QMT model and the CBH model. The variation of the exponent s with temperature, in particular increasing s by decreasing temperatures, is consistent with the CBH model in which the relaxation process is by hopping of charges between pair of localised states. The consistency of the CBH model for both σ_{AC}^{Pc} and σ_{AC}^{NC} is further investigated by fitting the following CBH equation to each of the experiments.

$$\sigma_{AC} = \frac{\pi^3}{24} N^2 \varepsilon\ \varepsilon_0 \omega R_\omega^6 \tag{8.8}$$

where

$$R_{\omega} = \frac{e^2}{\pi\varepsilon\ \varepsilon_0 \left(W_m + kT\ln(\omega\tau_0)\right)}. \tag{8.9}$$

W_m (maximum barrier height) and N (density of hopping sites) are the variables whose values are found through the fitting process. The other parameters are characteristic relaxation time which is assumed to be equal to the inverse of phonon vibration frequency, $\tau_0 = 10^{-13}$ s, and the value of dielectric constant considered to be 5 and 6.2, respectively, for C_6H_2Pc and the nanocomposite, as calculated in Section 8.4. Figures 8.7 and 8.8 depict the results of the fitting for both C_6H_2Pc and the nanocomposite, respectively. To get a clear impression of the fitting results, the results are presented in two plots: the plots of the temperature-dependence of the AC conductivity in the form of Arrhenius-like plot (σ_{AC} vs. 1000/*T*), and the temperature-dependence of the exponent s (s vs. *T*). The theoretical values of *s* are calculated using Equation (2.21) which is rewritten below for the sake of convenience:

$$s_{CBH}\left(\omega, T\right) = 1 - \frac{6kT}{W_m + kT\ln(\omega\tau_0)} \tag{8.10}$$

The typical values are calculated at the fixed frequency of 10^3 Hz. Note that the frequency dispersion of *s* is very weak and negligible (lower than %1 and %1.3 for the obtained values of W_m^{Pc} and W_m^{NC}, respectively). It is realised from the fitting results that the CBH model is well fitted to the AC conductivity of both materials at temperatures lower than 240 K. For higher temperatures (*T*>240), the temperature-dependence of σ_{AC}^{Pc} and σ_{AC}^{NC} is much stronger than what predicted by the CBH model.

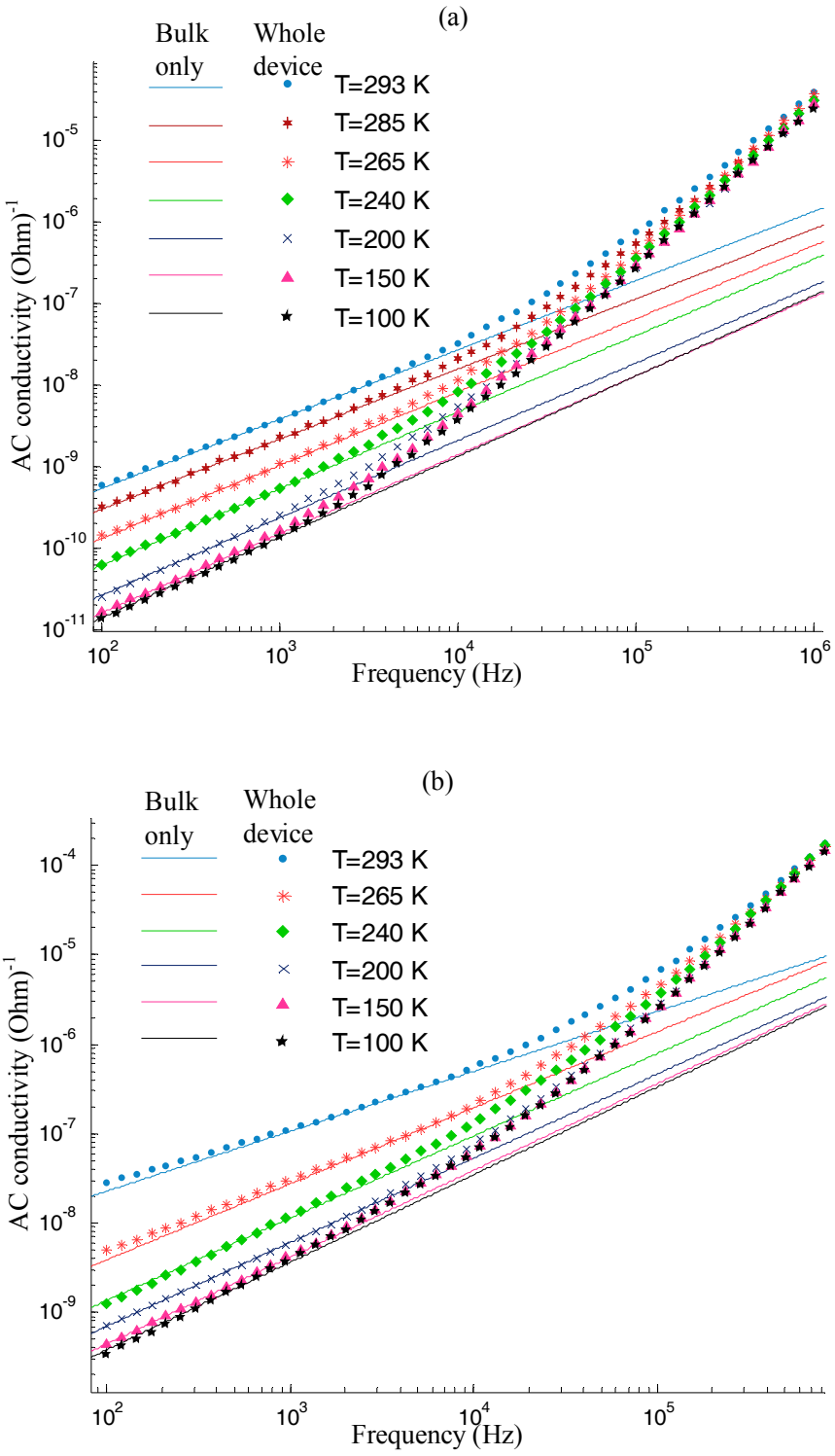

Figure 8.6 AC conductivity of (a) C_6H_2Pc and (b) C_6H_2Pc/PbS after correcting the effect of lead resistance. The frequency response of the devices is influenced by the lead resistance mainly at frequencies higher than 10^4 Hz at room temperature which shifts to lower frequency by decreasing temperature.

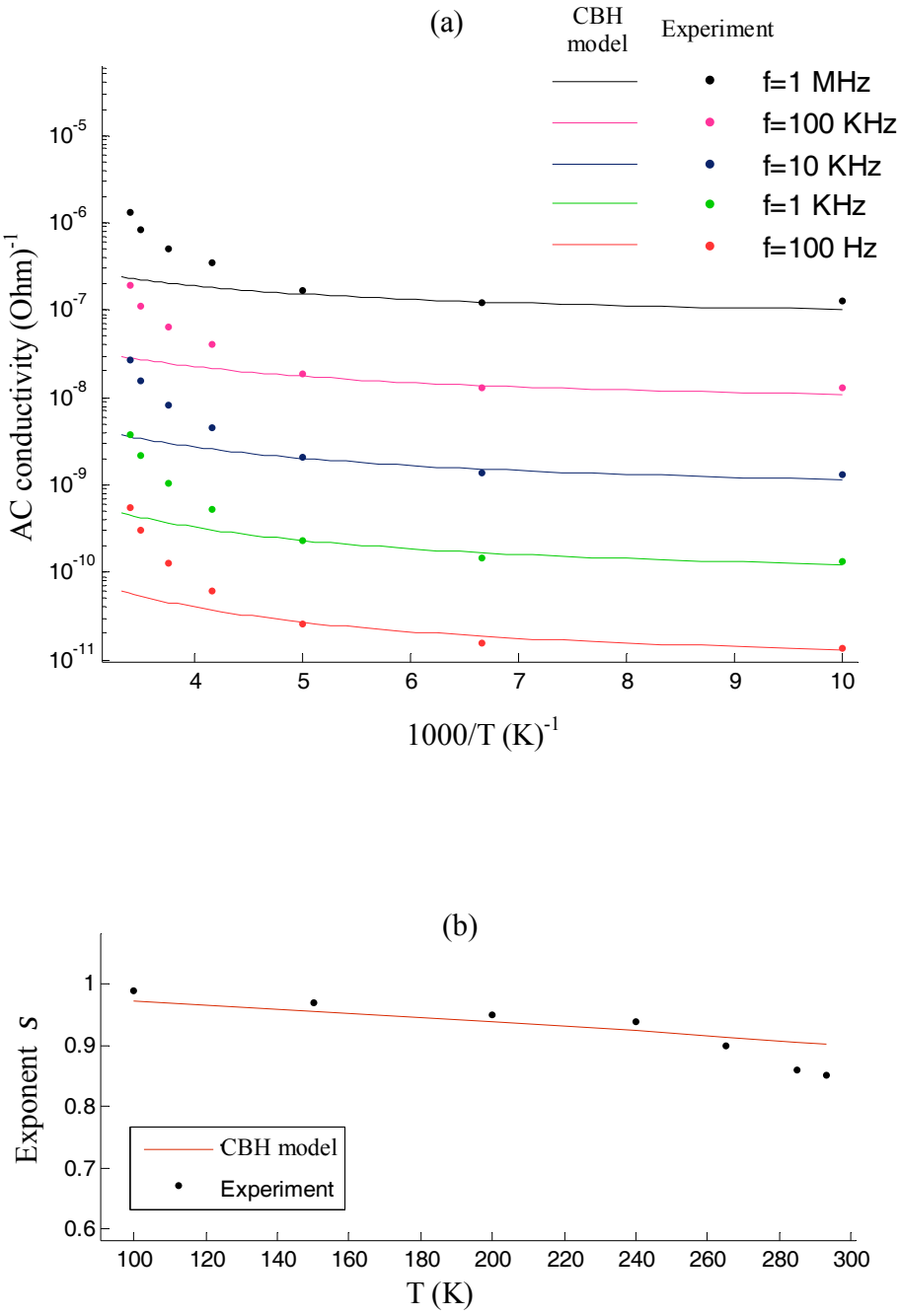

Figure 8.7 Fitting the CBH model to the experimental data of C_6H_2Pc device presenting by (a) temperature-dependence of the AC conductivity (b) temperature-dependence of exponent *s*.

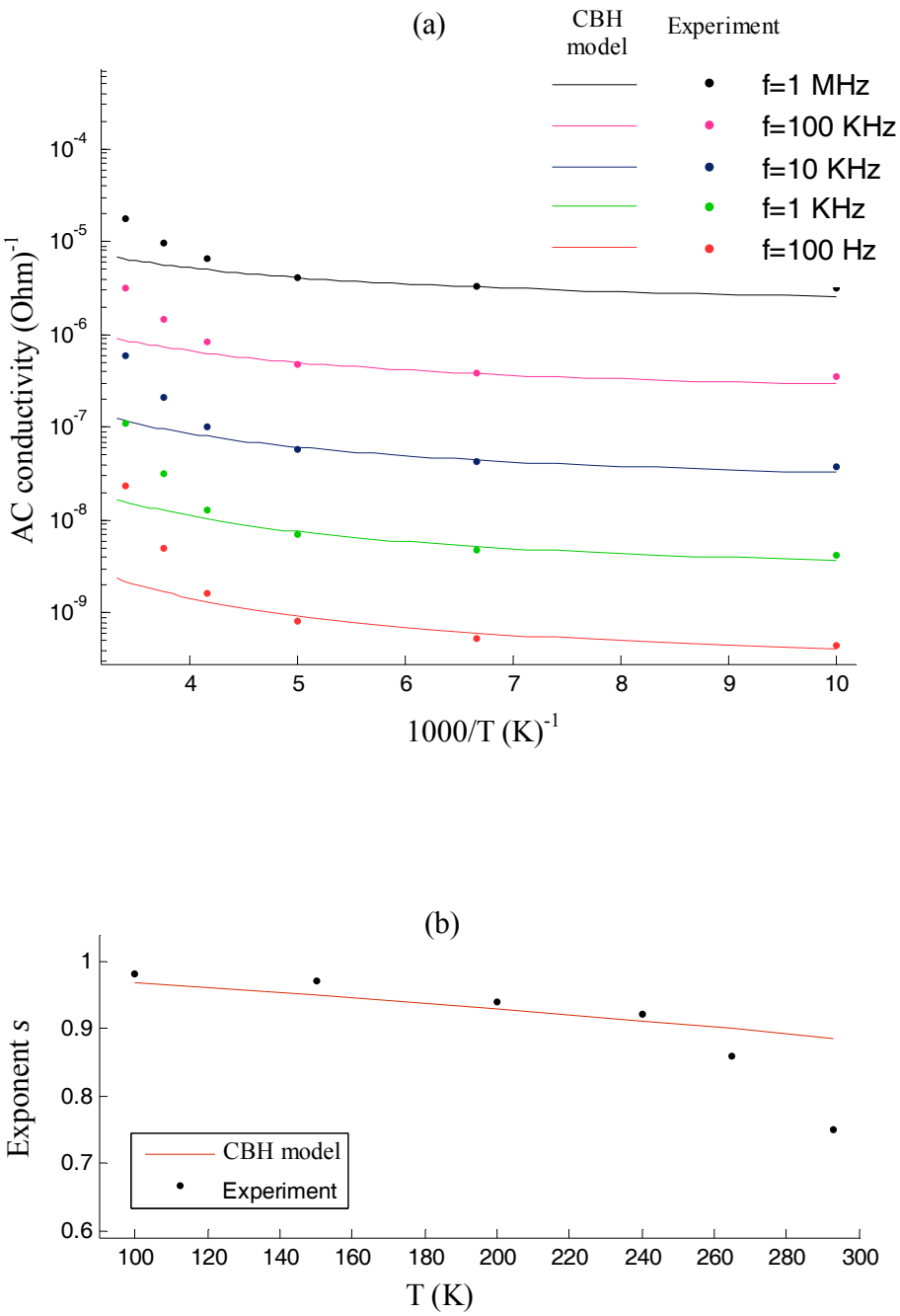

Figure 8.8 Fitting the CBH model to the experimental data of C_6H_2Pc/PbS device presenting by (a) temperature-dependence of the AC conductivity (b) temperature-dependence of exponent *s*.

The obtained values of W_m and N for both materials have been listed in Table 8.5. The value of W_m in the nanocomposite is smaller than that of C_6H_2Pc, while N of the nanocomposite is larger, by a factor of 6, compared to that of C_6H_2Pc. These observations suggest that the incorporation of the PbS QDs in C_6H_2Pc introduces new hopping sites with smaller binding energy, which dominantly contribute in the AC conduction of the nanocomposite, at least for T<240 K. Some possible sources of the new hopping sites can be morphological defects introduced to the matrix by inclusion of the PbS QDs or probable surface states and dangling bonds of the PbS QDs. Using the relation of R_ω, Equation (2.19), the most probable hopping length in the nanocomposite is found to be 0.69 ± 0.1 nm which is much smaller than the distance between the PbS QDs in the nanocomposite, ~11.7 nm presented in Table 5.4, indicating there should not be any direct hopping between two neighbouring QDs.

Table 8.5 Parameters applied for fitting the CBH model to the AC conductivity of the materials.

	W_m (eV)	N (m^{-3})	ε	τ_0 (s)
C_6H_2Pc	2	7.3×10^{25}	5	10^{-13}
C_6H_2Pc/PbS	1.8	4.5×10^{26}	6.2	10^{-13}

8.4 Dielectric constant

Based on the Equation (8.1), the relative dielectric constant of the device is calculated using the following expression

$$\varepsilon = \frac{d}{\varepsilon_0 A}\frac{Y''}{\omega}. \tag{8.11}$$

Figure 8.9 shows the frequency-dependence of the dielectric constant of C_6H_2Pc and the nanocomposite device. The nanocomposite exhibits stronger frequency

dispersion compared to the pure matrix. This may be referred to the presence of interfacial polarisation at the interface between the PbS QDs and the matrix. The interfacial polarisation typically observed in heterojunction systems when the polarisation abilities of the phases are different, and it is mainly dominant at low frequency region [176]. The frequency- and temperature-dependence of ε in both devices are getting weak by decreasing temperature and become almost disappeared at around 200 K. The value of dielectric constant at very high frequencies, near optical frequencies, corresponds only to electronic polarisation of materials (displacement of electrons around nuclei) rather than any other polarisation such as interfacial, dipole orientational and/or ionic polarisation. Lowering temperature can also reduce the effect of the orientational polarisation. Accordingly, the high-frequency dielectric constant can be determined from the saturation value of ε at very high-frequency and low temperature. The dielectric constant of the materials at the highest attained frequency and lowest temperature is found to be 5 and 6.2 corresponding to C_6H_2Pc and the nanocomposite, respectively. As seen in the figures, there is a sharp drop in ε at the higher end of the scanned frequency in both devices. This drop is attributed to the effect of lead resistance at high frequency region. According to the equivalent circuit and considering $R_b >> R_c$, Y'' in Equation (8.6) can be written as

$$Y'' = \frac{1/C_b\omega}{\left(1/C_b\omega\right)^2 + \left(R_c\right)^2} \tag{8.12}$$

Using expression (8.12), the dielectric constant of both devices is defined by

$$\varepsilon = \frac{\varepsilon_b}{1 + {R_c}^2 C_0^2\, \omega^2 \varepsilon_b^2} \tag{8.13}$$

where $\varepsilon_b = C_b/C_0$.

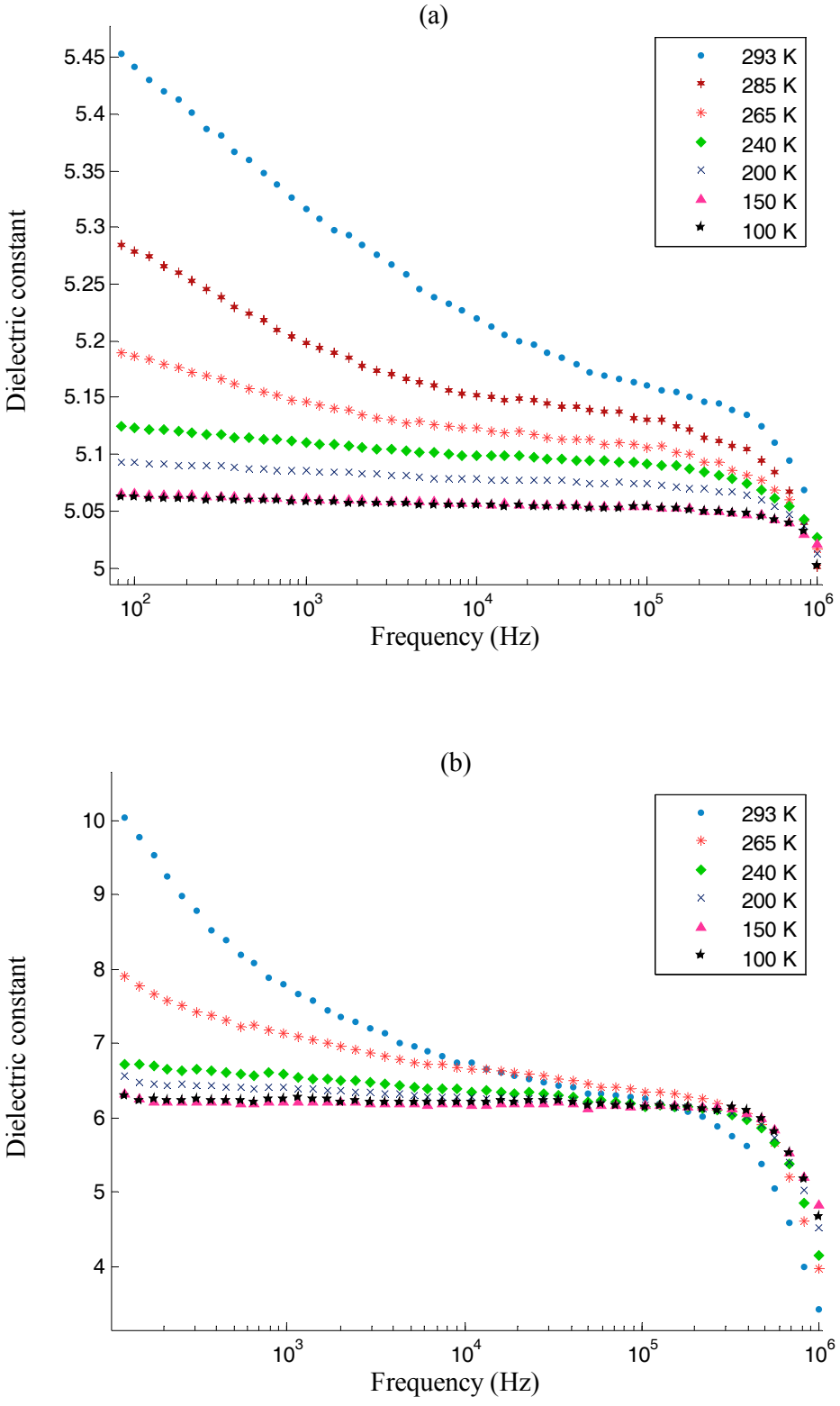

Figure 8.9 Frequency dispersion of dielectric constant of (a) C_6H_2Pc and (b) C_6H_2Pc/PbS device.

As evident from the above relation, at lower frequencies, i.e. $\omega << 1/(R_c C_0 \varepsilon_b)$, the lead resistance has no influence on ε whereas it causes a sharp drop in the dielectric constant at higher frequencies. The obtained values of the dielectric constant of the nanocomposite and C_6H_2Pc correspond to ε before the occurrence of the sharp drop.

CHAPTER 9

Conclusions and Future Work

9.1 Concluding remarks

A unique organic/inorganic nanocomposite of lead sulphide quantum dots embedded in a non-peripherally octa-hexyl metal-free phthalocyanine film was successfully prepared by exposure of thin spun films of non-peripherally octa-hexyl lead phthalocyanine to hydrogen sulphide gas. All the simplicity of the preparation process arises from the special feature of the precursor, C_6PbPc. This substituted lead phthalocyanine has a degree of lead lability leading to easily release the lead ion from the centre of phthalocyanine ring and formation of the PbS by sulphidation with H_2S gas. The formation of particles in the size of quantum dots indicates that the QDs aggregation tendency was limited by the solid environment of the phthalocyanine film, with no need of capping agents.

This nanocomposite is composed of two functional materials (C_6H_2Pc and PbS QDs), each with specific optical and electrical properties. The nanocomposite possesses some of the specific properties of each of the components. Being light-weight, flexible and cost-effective are all owing to the matrix, C_6H_2Pc. Besides, the visible absorption property of the nanocomposite mainly arises from the intense absorbance

of C_6H_2Pc in this region. The analysis of the optical absorption proves that the PbS QDs are subjected to the strong quantum confinement effect which causes a band gap modification from 0.41 eV in the bulk to 1.95 eV leading to significant change in the QDs properties compared to the bulk. The observed blue-shift in the absorption edge of the PbS QDs with respect to the bulk is responsible for an increase in the absorbance of the nanocomposite at the visible region beyond 600 nm.

Fundamental electrical studies specify the effects of inclusion of the PbS QDs on the electrical property of the nanocomposite. It is revealed that the inclusion of the QDs can enhance the conductivity by near two orders of magnitude, without formation of a connected network by the QDs inside the matrix. The conduction mechanism is also found to be based on a thermally activated process in both the nanocomposite and the matrix, although the inclusion of the QDs reduces the activation energy from 0.82 eV to 0.32 eV. Analysis of the conduction behaviour at high field indicates that the QDs change the dominant conduction mechanism from the probable space-charge limited current in the matrix to the Poole-Frenkel mechanism in the nanocomposite.

The AC conductivity of the nanocomposite is frequency-dependent following the universal power-law in frequency ranging from 100 Hz to 1 MHz. The charge relaxation is found to occur by hopping between localised states mainly at T<240 K. By fitting data to the CBH model, the hopping length was found to be 0.69 ± 0.1 nm which is much smaller than the estimated distance between the PbS QDs, ~ 11.7 nm, indicating the hopping cannot be directly between the neighbouring QDs and involves the localised states within the matrix.

9.2 Future work

Following the fundamental study undertaken in this thesis, further investigations are suggested to determine the special characteristics and features of this nanocomposite in pursuit of their device applications. Some examples are listed below:

- For the first priority, it will be valuable to study the effect of possible variations on the microstructure of the nanocomposite. The outcome of this research is helpful to modify the constructed nanocomposite well-matched for specific applications. Some factors such as temperature during the gas exposure, the thickness of the film and the exposure time are likely to alter the microstructure of the nanocomposite. For instance, it is believed that the size of PbS QDs may increase by rising the temperature during the H_2S gas treatment. Heating plausibly mobilises the particles and causes more agglomeration and consequently yields the formation of bigger particles, as it is observed in other nanocomposites too [77]. By controlling the size of the PbS QDs, the size of their band gap and subsequently their optical and electrical properties can be tuned. This may have direct effects on the properties of the nanocomposite.

- As a complementary work to the electrical study, investigation of the transient electrical behaviour and carrier mobility of the nanocomposite is recommended. A simple and accessible technique of time of flight measurement may clearly determine any modification in charge mobility by inclusion of the PbS QDs into the C_6H_2Pc.

- Further investigation is required to verify the dominance of the SCLC mechanism using the scaling law. If the current density follows the SCLC mechanism, then the current-voltage relationship obeys a scaling law of the following form:

$$\frac{J}{d} = f\left(\frac{V}{d^2}\right) \tag{9.1}$$

where f is an arbitrary function, e.g. $f(x) = \frac{9}{8}\varepsilon\varepsilon_0\mu x^2$ in the case of trap-free SCLC (Equation (2.2)). Accordingly, the thickness of the film can be used as a variable factor to examine the possibility of SCLC mechanism in the film. It should be noted that the scaling law is based on the assumption of field-independent mobility and neglecting diffusion of carriers.

- Study the electrical conduction of the nanocomposite using effective media approximation (EMA) would also be a valuable work. The EMA estimates the relation between the properties of an inhomogeneous mixture and its components using the known physical property of each component. By this approach, the electrical conductivity of the nanocomposite can be expressed as a function of the electrical conductivity and also the volume fraction of the QDs (χ^{QD}) and the matrix (χ^{Pc}):

$$\sigma^{NC} = f\left(\sigma^{Pc}, \sigma^{QD}, \chi^{Pc}, \chi^{QD}\right) \tag{9.2}$$

Some of the proposed models for such inhomogeneous mixture are presented in [38].

- The bistable electrical conduction behaviour of the nanocomposite sandwiched between ITO and Al electrodes is repeatedly observed during the steady-state electrical measurement. By applying the threshold voltage, the electrical conduction of the device suddenly increases. A typical example of these observations is shown in Figure 9.1. It was found that the high-conduction states can be retained by removing the power, and to recover back the low-conduction state negative voltage should be applied. According to different types of memory devices, volatile and non-volatile, such behaviour is base of non-volatile memory devices in which the stored data are not lost by turning off the electrical power. The switching behaviour is the minimum requirement for memory devices. Other factors such as switching speed, on/off ratio and retention time are vital for high performance memory devices. A study on the potential applications of C_6H_2Pc/PbS in organic memory devices would be a beneficial future work.
- The inherent optical properties of both components of the nanocomposite are encouraging to investigate the optoelectronic properties of this nanocomposite. The preliminary results of this work show that the mismatch between the energy levels of the PbS QDs and phthalocyanine is desirable for photovoltaic devices. The operation of a photovoltaic device is based on the separation of photogenerated excitons to holes and electrons at the interface between phases. The high efficiency achieves when the generated electrons and holes respectively transfer to hole- and electron-conducting materials. Metal-free phthalocyanines are hole-conducting semiconductors.

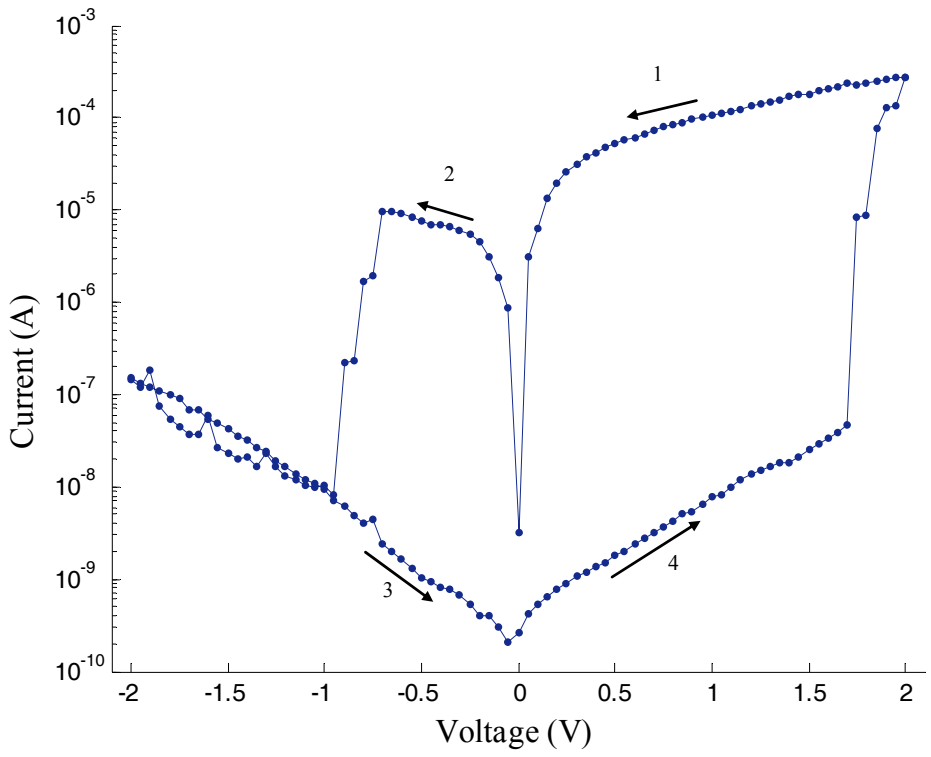

Figure 9.1 The bistable electrical behaviour of C_6H_2Pc/PbS nanocomposite sandwiched between ITO and Al electrodes. The arrows show the direction of sweeping voltage; note that the device was already switched to high-conduction states, so the loop starts from high-conduction state. The high-conduction state can be retained by removing the power.

According to the estimated band diagram of the nanocomposite (Figure 7.3), the HOMO level of C_6H_2Pc is energetically located at lower energy (lies closer to the vacuum level) than that of the PbS QDs, and hence more favourable for generated holes, while the generated electrons are probably captured inside the PbS QDs. Moreover, both components are probably able to generate excitons according to the results reported in literature [81, 69]. Therefore, it is really worthwhile to study the idea of fabricating organic photovoltaic devices based on C_6H_2Pc/PbS nanocomposite. Although, the low concentration of the PbS QDs cannot form a conductive pathway for electrons, the photovoltaic performance can still be excepted as has already

been observed for MEH-PPV/PbS in which the photogenerated electrons are trapped inside the PbS QDs [81].

- The C_6H_2Pc/PbS may also be an appropriate candidate for active materials in photodetectors. The silicon-based photodetectors have high efficiency but work beyond the visible region due to low band gap of silicon. Many efforts have been made to fabricate low-cost organic photodetectors working in the visible region, although so far they could not reach to the high sensitivity of silicon devices. The C_6H_2Pc/PbS composite with absorption property in wide range of the visible region can be a candidate for visible photodetectors.

- One of the main advantages of organic/inorganic nanocomposite is possibility to exploit the privilege of the QDs in light-weight and flexible organic devices. Among all the features of PbS QDs, the strong non-linear optical property is highly noticeable. Study about this feature in C_6H_2Pc/PbS nanocomposite can reveal the potential application of this nanocomposite in fast optical switches and telecommunication devices.

Appendix 1 Standard database of Galena

Name and formula

Reference code:	00-005-0592
Mineral name:	Galena, syn
PDF index name:	Lead Sulphide
Empirical formula:	PbS
Chemical formula:	PbS

Crystallographic parameters

Crystal system:	Cubic
Space group:	Fm-3m
Space group number:	225
a (Å):	5.9362
b (Å):	5.9362
c (Å):	5.9362
Alpha (°):	90.0000
Beta (°):	90.0000
Gamma (°):	90.0000
Calculated density (g/cm^3):	7.60
Measured density (g/cm^3):	7.57
Volume of cell (10^6 pm^3):	209.18
Z:	4.00
RIR:	-

Subfiles and Quality

Subfiles:	Inorganic Mineral Alloy, metal or intermetalic Common Phase Educational pattern Forensic NBS pattern
Quality:	Indexed (I)

Comments

Color:	Gray metallic.
General comments:	Opaque mineral optical data on synthetic sample: RR2Re= 43.7, Disp.=16, VHN100=59-65, Color values=.304, .309, 43.7, Ref.: IMA Commission on Ore Microscopy QDF.
Sample source:	Sample from National Lead Company.
Analysis:	Spectroscopic analysis: <0.01% Cu, Fe, Ag, Al, Mg, Si, Sn and Ca in sample.

Additional pattern:	To replace 00-022-0652 and validated by calculated pattern. See PDF 01-078-1054, 01-078-1055, 01-078-1056, 01-078-1057, 01-078-1058, 01-078-1897 and 01-077-0244.
Unit cell data source:	Powder Diffraction.
Temperature:	Pattern taken at 299 K.

References

Primary reference:	Swanson, Fuyat., *Natl. Bur. Stand. (U.S.), Circ. 539*, **II**, 18, (1953)

Peak list

No.	h	k	l	d [A]	2Theta[deg]	I [%]
1	1	1	1	3.42900	25.964	84.0
2	2	0	0	2.96900	30.075	100.0
3	2	2	0	2.09900	43.059	57.0
4	3	1	1	1.79000	50.978	35.0
5	2	2	2	1.71400	53.413	16.0
6	4	0	0	1.48400	62.540	10.0
7	3	3	1	1.36200	68.883	10.0
8	4	2	0	1.32700	70.969	17.0
9	4	2	2	1.21200	78.923	10.0
10	5	1	1	1.14240	84.797	6.0
11	4	4	0	1.04890	94.511	3.0
12	5	3	1	1.00340	100.294	5.0
13	6	0	0	0.98930	102.271	6.0
14	6	2	0	0.93860	110.308	4.0
15	5	3	3	0.90500	116.676	2.0
16	6	2	2	0.89520	118.741	4.0
17	4	4	4	0.85680	128.065	1.0
18	7	1	1	0.83120	135.862	3.0
19	6	4	0	0.82320	138.696	3.0

Structure

No.	Name	Elem.	X	Y	Z	Biso	sof	Wyck.
1	PB1	Pb	0.00000	0.00000	0.00000	0.5000	1.0000	4a
2	S1	S	0.50000	0.50000	0.50000	0.5000	1.0000	4b

Stick Pattern

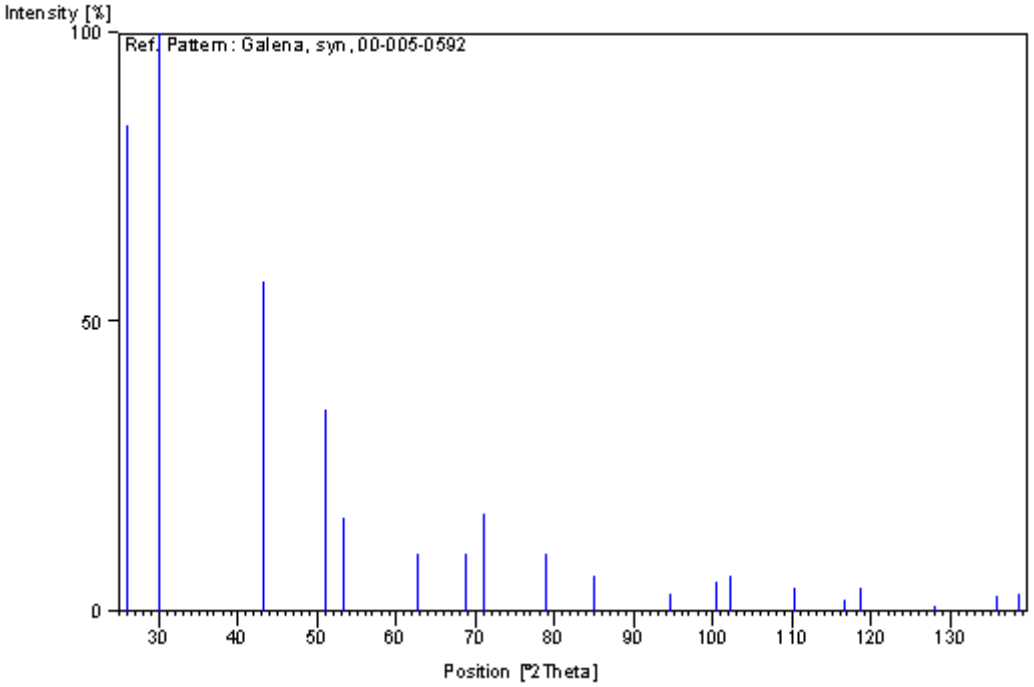

Figure A1.1 Stick Pattern of Galena

Appendix 2 Particle in a 1-D box

Consider a particle of mass m whose motion is confined in space and an energy E which evolves in a potential $U(x)$ mathematically defined by [177]

$$U(x) = \begin{cases} \infty & \text{if } x < 0 \text{ or } x > a \\ 0 & \text{if } 0 < x < a \end{cases} \tag{A2.1}$$

The following Schrodinger equation can be expressed in the above mentioned potential

$$\begin{cases} \Psi(x) = 0 & \text{if } x < 0 \text{ or } x > a \\ \frac{\hbar^2}{2m}\frac{d^2\Psi(x)}{dx^2} + E\,\Psi(x) = 0 & \text{if } 0 < x < a \end{cases} \tag{A2.2}$$

The general solution of the Schrodinger equation inside the box can be written as

$$\Psi(x) = A\sin(kx) + B\cos(kx) \tag{A2.3}$$

Subject to the following boundary conditions

$$\Psi(0) = \Psi(a) = 0 \tag{A2.4}$$

Applying the boundary conditions yields

$$\begin{cases} B = 0 \\ \sin(ka) = 0 \;\Rightarrow\; k = k_n = n\frac{\pi}{a} \quad for \;\; n = \pm 1, \pm 2, \ldots \end{cases} \tag{A2.5}$$

Substituting the solution in equation (A2.2) yields the energy of a particle in 1-D box

$$E_n = n^2 \frac{\hbar^2 \pi^2}{2ma^2} \tag{A2.6}$$

References

1. W. Brütting, *Physics of organic semiconductors*, Wiley-VCH, 2005.

2. B. A. Gregg, S. G. Chen and R. A. Cormier, *Coulomb forces and doping in organic semiconductors*, Chem. Mat. **16** (2004), no. 23, 4586-4599.

3. L. Merhari, *Hybrid nanocomposites for nanotechnology*, Springer, 2009.

4. N. C. Greenham, X. peng and A. P. Alivisatos, *Charge separation and transport in conjugated-polymer/semiconductor-nanocrystal composites studied by photoluminescence quenching and photoconductivity* Physical Review B **54** (1996), no. 24, 17628-17637.

5. A. Arora and G. W. Padua, *Review: Nanocomposites in food packaging*, J. Food Sci. **75**, no. 1, R43-R49.

6. L. L. Beecroft and C. K. Ober, *Nanocomposite materials for optical applications*, Chem. Mat. **9** (1997), no. 6, 1302-1317.

7. R. Gangopadhyay and A. De, *Conducting polymer nanocomposites: A brief overview*, Chem. Mat. **12** (2000), no. 3, 608-622.

8. A. V. Nabok, A. K. Ray, M. J. Cook, P. M. Burnham, Iwantono, H. Yanuar, M. Simmonds and T. V. Basova, *Lead sulphide/phthalocyanine nanocomposite spun films*, IEEE Trans. Nanotechnol. **3** (2004), no. 3, 388-394.

9. H. Inokuchi, *The discovery of organic semiconductors. Its light and shadow*, Organic electronics **7** (2006), 62-76.

10. L. Brus, *Electronic wave-functions in semiconductor clusters - experiment and theory*, Journal of Physical Chemistry **90** (1986), no. 12, 2555-2560.

11. V. A. Singh, V. Ranjan and V. Kapoor, *Semiconductor quantum dots: Theory and phenomenology*, Bull. Mat. Sci. **22** (1999), no. 3, 563-569.

12. A. D. Yoffe, *Low-dimensional systems: Quantum size effects and electronic properties of semiconductor microcrystallites (zero-dimensional systems) and some quasi-two dimensional systems*, Advances in Physics **42** (1993), no. 2, 173-266.

13. C. W. Tang and S. A. Vanslyke, *Organic electroluminescent diodes*, Appl. Phys. Lett. **51** (1987), no. 12, 913-915.

14. D. Hertel and H. Bassler, *Photoconduction in amorphous organic solids*, ChemPhysChem **9** (2008), no. 5, 666-688.

15. H. Bassler, *Charge transport in disordered organic photoconductors- a monte-carlo simulation study*, Phys. Status Solidi B-Basic Res. **175** (1993), no. 1, 15-56.

16. C. D. Dimitrakopoulos and P. R. L. Malenfant, *Organic thin film transistors for large area electronics*, Advanced Materials **14** (2002), no. 2, 99-+.

17. F. Eder, H. Klauk, M. Halik, U. Zschieschang, G. Schmid and C. Dehm, *Organic electronics on paper*, Appl. Phys. Lett. **84** (2004), no. 14, 2673-2675.

18. C. D. Dimitrakopoulos and D. J. Mascaro, *Organic thin-film transistors: A review of recent advances*, IBM J. Res. Dev. **45** (2001), no. 1, 11-27.

19. G. Horowitz, *Organic field-effect transistors*, Advanced Materials **10** (1998), no. 5, 365-377.

20. A. Dodabalapur, *Organic light emitting diodes*, Solid State Commun. **102** (1997), no. 2-3, 259-267.

21. J. R. Sheats, H. Antoniadis, M. Hueschen, W. Leonard, J. Miller, R. Moon, D. Roitman and A. Stocking, *Organic electroluminescent devices*, Science **273** (1996), no. 5277, 884-888.

22. J. M. Nunzi, *Organic photovoltaic materials and devices*, C. R. Phys. **3** (2002), no. 4, 523-542.

23. H. Hoppe and N. S. Sariciftci, *Organic solar cells: An overview*, J. Mater. Res. **19** (2004), no. 7, 1924-1945.

24. B. G. Streetman and S. Banerjee, *Solid state electronic devices*, Prentice Hall, 2000.

25. S. Braun, W. R. Salaneck and M. Fahlman, *Energy-level alignment at organic/metal and organic/organic interfaces*, Advanced Materials **21** (2009), no. 14-15, 1450-1472.

26. H. Ishii, K. Sugiyama and E. Ito, *Energy level alignment and interfacial electronic structures at organic/metal and organic/organic interface*, Advanced Materials **11** (1999), no. 8, 605-625.

27. M. C. Petty, *Molecular electronics from principles to practice*, John Wiley & Sons Ltd., 2007.

28. K. Potje-Kamloth, *Semiconductor junction gas sensors*, Chemical Reviews **108** (2008), no. 2, 367-399.

29. J. G. Simmons, *Conduction in thin dielectric films*, Journal of physics D: Applied Physics **4** (1971), 613.

30. N. F. Mott and R. W. Gurney, *Electronic processes in ionic crystals*, Clarendon Press, Oxford, 1948.

31. A. Rose, *Space-charge-limited currents in solids*, Physical Review **97** (1955), no. 6, 1538-1544.

32. M. A. Lampert, *Volume-controlled current injection in insulators*, Rep. Prog. Phys. **27** (1964), 329-367.

33. P. W. M. Blom and M. Vissenberg, *Charge transport in poly(p-phenylene vinylene) light-emitting diodes*, Mater. Sci. Eng. R-Rep. **27** (2000), no. 3-4, 53-94.

34. J. G. Simmons, *Poole-frenkel effect and schottky effect in metal-insulator-metal systems*, Physical Review **155** (1967), no. 3, 657.

35. C. A. Mead, *Electron transport mechanisms in thin insulating films*, Physical Review **128** (1962), no. 5, 2088-2093.

36. R. D. Gould, "High-field conduction in nanostructures," *Encyclopedia of nanoscience and nanotechnology*, H. S. Nalwa (Editor), vol. 3, American scientific publishers, 2004, pp. 891-915.

37. J. L. Hartke, *The three dimensional poole frenkel effect*, J. Appl. Phys. **39** (1968), 4871.

38. S. Kasap and P. Capper, *Handbook of electronic and photonic materials*, Springer, 2006.

39. A. R. Long, *Frequency-dependent loss in amorphous semiconductors*, Advances in Physics **31** (1982), no. 5, 553-637.

40. A. K. Jonscher, *Dielectric relaxation in solids*, Chelsea Dielectrics Press Ltd, London, 1983.

41. S. R. Elliott, *Ac conduction in amorphous chalcogenid and pnictide semiconductors*, Advances in Physics **36** (1987), no. 2, 135-218.

42. P. Erk and H. Hengelsberg, "Phthalocyanine dyes and pigments," *The porphyrin handbook*, K. M. Kadish, K. M. Smith and R. Guilard (Editors), vol. 19, Academic Press, San Diego, 2003, p. 105.

43. D. D. Eley, *Phthalocyanines as semiconductors*, Nature **162** (1948), 819-819.

44. C. G. Claessens, U. Hahn and T. Torres, *Phthalocyanines: From outstanding electronic properties to emerging applications*, Chem. Rec. **8** (2008), no. 2, 75-97.

45. G. Guillaud, J. Simon and J. P. Germain, *Metallophthalocyanines - gas sensors, resistors and field effect transistors*, Coord. Chem. Rev. **178** (1998), 1433-1484.

46. J. Jiang, *Functional phthalocyanine molecular materials*, Springer, 2010.

47. M. Pope and C. e. Swenberg, *Electronic processes in organic crystals and polymers*, Oxford university press, 1999.

48. A. Miyamoto, K. Nichogi, A. Taomoto, T. Nambu and M. Murakami, *Structural control of evaporated lead-phthalocyanine films*, Thin Solid Films **256** (1995), 64-67.

49. Y. Z. Wu, H. Tian, K. C. Chen, Y. Q. Liu and D. B. Zhu, *Synthesis and properties of soluble metal-free phthalocyanines containing tetra- or octa-alkyloxy substituents*, Dyes Pigment. **37** (1998), no. 4, 317-325.

50. R. D. Gould, *Structure and electrical conduction properties of phthalocyanine thin films*, Coord. Chem. Rev. **156** (1996), 237-274.

51. N. B. McKeown, I. Chambrier and M. J. Cook, *Synthesis and characterization of some 1,4,8,11,15,18,22,25,-octa-alkyl-22,25-bis(carboxypropyl) phthalocyanines and 1,4,8,11,15,18-hexa-alkyl-22,25-bis(carboxypropyl) phthalocyanines*, J. Chem. Soc.-Perkin Trans. 1 (1990), no. 4, 1169-1177.

52. M. J. Cook, *Properties of some alkyl substituted phthalocyanines and related macrocycles*, Chem. Rec. **2** (2002), no. 4, 225-236.

53. N. B. Mckeown, *Phthalocyanine materials: Synthesis, structure and function*, Cambridge University Press, 1998.

54. I. Muzikante, E. Fonavs, E. Silinsh, C. Fretigny, M. Bouvet, J. Simon and S. Spirkovitch, *Charge carrier transport properties of thin films of an intrinsic molecular semiconductor: Lutetium bisphthalocyanine*, Molecular Crystals and Liquid Crystals Science and Technology Section C-Molecular Materials **9** (1998), no. 4, 301-331.

55. G. Guillaud and J. Simon, *Transient properties of nickel phthalocyanine thin-film transistors*, Chem. Phys. Lett. **219** (1994), no. 1-2, 123-126.

56. G. Guillaud, M. Alsadoun, M. Maitrot, J. Simon and M. Bouvet, *Field-effect transistors based on intrinsic molecular semiconductors*, Chem. Phys. Lett. **167** (1990), no. 6, 503-506.

57. Z. Bao, A. J. Lovinger and A. Dodabalapur, *Organic field-effect transistors with high mobility based on copper phthalocyanine*, Appl. Phys. Lett. **69** (1996), no. 20, 3066-3068.

58. N. B. Chaure, A. N. Cammidge, I. Chambrier, M. J. Cook, M. G. Cain, C. E. Murphy, C. Pal and A. K. Ray, *High-mobility solution-processed copper phthalocyanine-based organic field-effect transistors*, Sci. Technol. Adv. Mater. **12** (2011), no. 2, 7.

59. Z. N. Bao, A. J. Lovinger and A. Dodabalapur, *Highly ordered vacuum-deposited thin films of metallophthalocyanines and their applications in field-effect transistors*, Advanced Materials **9** (1997), no. 1, 42-&.

60. M. Ofuji, K. Ishikawa, H. Takezoe, K. Inaba and K. Omote, *Crystallite size effect on the hole mobility of uniaxially aligned copper phthalocyanine thin-film field-effect transistors*, Appl. Phys. Lett. **86** (2005), no. 6.

61. L. Q. Li, Q. X. Tang, H. X. Li, W. Hu, X. O. Yang, Z. Shuai, Y. Q. Liu and D. Zhu, *Organic thin-film transistors of phthalocyanines*, Pure Appl. Chem. **80** (2008), no. 11, 2231-2240.

62. M. J. Cook, A. J. Dunn, S. D. Howe, A. J. Thomson and K. J. Harrison, *Octa-alkoxy phthalocyanine and naphthalocyanine derivatives dyes with q-band absorption in the far red or near-infrared*, J. Chem. Soc.-Perkin Trans. 1 (1988), no. 8, 2453-2458.

63. L. Bakueva, S. Musikhin, E. H. Sargent, H. E. Ruda and A. Shik, "Luminescence and photovoltaic effects in polymer-based nanocomposites," *Handbook of organic-inorganic hybrid materials and nanocomposites*, H. S. Nalwa (Editor), vol. 2, American Scientific, 2003, p. 181.

64. C. W. Tang, *2-layer organic photovoltaic cell*, Appl. Phys. Lett. **48** (1986), no. 2, 183-185.

65. D. Wohrle and D. Meissner, *Organic solar-cells*, Advanced Materials **3** (1991), no. 3, 129-138.

66. R. Koeppe, N. S. Sariciftci, P. A. Troshin and R. N. Lyubovskaya, *Complexation of pyrrolidinofullerenes and zinc-phthalocyanine in a bilayer organic solar cell structure*, Appl. Phys. Lett. **87** (2005), no. 24.

67. S. Uchida, J. G. Xue, B. P. Rand and S. R. Forrest, *Organic small molecule solar cells with a homogeneously mixed copper phthalocyanine: C-60 active layer*, Appl. Phys. Lett. **84** (2004), no. 21, 4218-4220.

68. J. G. Xue, S. Uchida, B. P. Rand and S. R. Forrest, *4.2% efficient organic photovoltaic cells with low series resistances*, Appl. Phys. Lett. **84** (2004), no. 16, 3013-3015.

69. Y. Terao, H. Sasabe and C. Adachi, *Correlation of hole mobility, exciton diffusion length, and solar cell characteristics in phthalocyanine/fullerene organic solar cells*, Appl. Phys. Lett. **90** (2007), no. 10, 3.

70. F. I. Bohrer, A. Sharoni, C. Colesniuc, J. Park, I. K. Schuller, A. C. Kummel and W. C. Trogler, *Gas sensing mechanism in chemiresistive cobalt and metal-free phthalocyanine thin films*, J. Am. Chem. Soc. **129** (2007), no. 17, 5640-5646.

71. C. L. Honeybourne and R. J. Ewen, *The enhancement of dark dc conductivity by gas-adsorption on thin films of macrocyclic copper complexes* J. Phys. Chem. Solids **44** (1983), no. 8, 833-838.

72. M. S. Nieuwenhuizen, A. J. Nederlof and A. W. Barendsz, *Metallophthalocyanines as chemical interfaces on a surface acoustic-wave gas sensor for nitrogen-dioxide*, Anal. Chem. **60** (1988), no. 3, 230-235.

73. F. L. E. Jakobsson, X. Crispin and M. Berggren, *Towards addressable organic impedance switch devices*, Appl. Phys. Lett. **87** (2005), no. 6, 3.

74. B. Mukherjee, A. K. Ray, A. K. Sharma, M. J. Cook and I. Chambrier, *A simply constructed lead phthalocyanine memory diode*, J. Appl. Phys. **103** (2008), no. 7, 4.

75. S. I. Shihub and R. D. Gould, *Frequency-dependence of electronic conduction parameters in evaporated thin films of cobalt phthalocyanine*, Thin Solid Films **254** (1995), no. 1-2, 187-193.

76. M. M. El-Nahass, A. F. El-Deeb and F. Abd-El-Salam, *Influence of temperature and frequency on the electrical conductivity and the dielectric properties of nickel phthalocyanine*, Organic electronics **7** (2006), no. 5, 261-270.

77. Y. Wang, A. Suna, W. Mahler and R. Kasowski, *Pbs in polymers: From molecules to bulk solids*, J. Chem. Phys. **87** (1987), no. 12, 7315-7322.

78. I. Kang and F. W. Wise, *Electronic structure and optical properties of pbs and pbse quantum dots*, J. Opt. Soc. Am. B-Opt. Phys. **14** (1997), no. 7, 1632-1646.

79. R. S. Yadav, P. Mishra, R. Mishra, M. Kumar and A. C. Pandey, *Growth mechanism and optical property of cds nanoparticles synthesized using amino-acid histidine as chelating agent under sonochemical process*, Ultrason. Sonochem. **17**, no. 1, 116-122.

80. M. A. Hines and G. D. Scholes, *Colloidal pbs nanocrystals with size-tunable near-infrared emission: Observation of post-synthesis self-narrowing of the particle size distribution*, Advanced Materials **15** (2003), no. 21, 1844-1849.

81. S. A. McDonald, G. Konstantatos, S. G. Zhang, P. W. Cyr, E. J. D. Klem, L. Levina and E. H. Sargent, *Solution-processed pbs quantum dot infrared photodetectors and photovoltaics*, Nat. Mater. **4** (2005), no. 2, 138-U114.

82. S. A. McDonald, P. W. Cyr, L. Levina and E. H. Sargent, *Photoconductivity from pbs-nanocrystal/semiconducting polymer composites for solution-processible, quantum-size tunable infrared photodetectors*, Appl. Phys. Lett. **85** (2004), no. 11, 2089-2091.

83. S. Zhang, P. W. Cyr, S. A. McDonald, G. Konstantatos and E. H. Sargent, *Enhanced infrared photovoltaic efficiency in pbs nanocrystal/semiconducting polymer composites: 600-fold increase in maximum power output via control of the ligand barrier*, Appl. Phys. Lett. **87** (2005), no. 23, 3.

84. L. Bakueva, I. Gorelikov, S. Musikhin, X. S. Zhao, E. H. Sargent and E. Kumacheva, *Pbs quantum dots with stable efficient luminescence in the near-ir spectral range*, Advanced Materials **16** (2004), no. 11, 926-929.

85. J. H. Warner, E. Thomsen, A. R. Watt, N. R. Heckenberg and H. Rubinsztein-Dunlop, *Time-resolved photoluminescence spectroscopy of ligand-capped pbs nanocrystals*, Nanotechnology **16** (2005), no. 2, 175-179.

86. R. D. Schaller, M. Sykora, J. M. Pietryga and V. I. Klimov, *Seven excitons at a cost of one: Redefining the limits for conversion efficiency of photons into charge carriers*, Nano Lett. **6** (2006), no. 3, 424-429.

87. Y. Wang, *Nonlinear optical properties of nanometer-sized semiconductor clusters*, Accounts Chem. Res. **24** (1991), no. 5, 133-139.

88. B. Liu, H. P. Li, C. H. Chew, W. X. Que, Y. L. Lam, C. H. Kam, L. M. Gan and G. Q. Xu, *Pbs-polymer nanocomposite with third-order nonlinear optical response in femtosecond regime*, Mater. Lett. **51** (2001), no. 6, 461-469.

89. H. S. Kim, M. H. Lee, N. C. Jeong, S. M. Lee, B. K. Rhee and K. B. Yoon, *Very high third-order nonlinear optical activities of intrazeolite pbs quantum dots*, J. Am. Chem. Soc. **128** (2006), no. 47, 15070-15071.

90. D. J. Asunskis, I. L. Bolotin and L. Hanley, *Nonlinear optical properties of pbs nanocrystals grown in polymer solutions*, Journal of Physical Chemistry C **112** (2008), no. 26, 9555-9558.

91. S. Komarneni, *Nanocomposites*, Journal of Materials Chemistry **2** (1992), no. 12, 1219-1230.

92. Y. Wang and N. Herron, *Optical-properties of cds and pbs clusters encapsulated in zeolite*, Journal of Physical Chemistry **91** (1987), no. 2, 257-260.

93. F. Gao, Q. Y. Lu, X. Y. Liu, Y. S. Yan and D. Y. Zhao, *Controlled synthesis of semiconductor pbs nanocrystals and nanowires inside mesoporous silica sba-15 phase*, Nano Lett. **1** (2001), no. 12, 743-748.

94. J. H. Chen, C. G. Chao, J. C. Ou and T. F. Liu, *Growth and characteristics of lead sulfide nanocrystals produced by the porous alumina membrane*, Surf. Sci. **601** (2007), no. 22, 5142-5147.

95. K. Moller, T. Bein, N. Herron, W. Mahler and Y. Wang, *Enccapsulation of lead sulfide molecular clusters into solid matrices. Structural analysis with x-ray absorption spectroscopy*, Inorg. Chem. **28** (1989), no. 15, 2914-2919.

96. Z. H. Zeng, S. H. Wang and S. H. Yang, *Synthesis and characterization of pbs nanocrystallites in random copolymer ionomers*, Chem. Mat. **11** (1999), no. 11, 3365-3369.

97. W. Mahler, *Polymer-trapped semiconductor particles*, Inorg. Chem. **27** (1988), no. 3, 435-436.

98. A. V. Nabok, T. Richardson, F. Davis and C. J. M. Stirling, *Cadmium sulfide nanoparticles in langmuir-blodgett films of calixarenes*, Langmuir **13** (1997), no. 12, 3198-3201.

99. E. S. Smotkin, C. Lee, A. J. Bard, A. Campion, M. A. Fox, T. E. Mallouk, S. E. Webber and J. M. White, *Size quantization effects in cadmium-sulfide layers formed by a langmuir-blodgett technique*, Chem. Phys. Lett. **152** (1988), no. 2-3, 265-268.

100. V. Erokhin, P. Facci, L. Gobbi, S. Dante, F. Rustichelli and C. Nicolini, *Preparation of semiconductor superlattices from lb precursor*, Thin Solid Films **327** (1998), 503-505.

101. I. Moriguchi, H. Nii, K. Hanai, H. Nagaoka, Y. Teraoka and S. Kagawa, *Synthesis of size-confined metal sulfides in langmuir_blodgett films*, Colloid Surf. A-Physicochem. Eng. Asp. **103** (1995), no. 3, 173-181.

102. A. Ruaudelteixier, J. Leloup and A. Barraud, *Insertion compounds in lb films*, Molecular Crystals and Liquid Crystals **134** (1986), no. 1-4, 347-354.

103. T. Kyprianidouleodidou, W. Caseri and U. W. Suter, *Size variation of pbs particles in high-refractive-index nanocomposites*, Journal of Physical Chemistry **98** (1994), no. 36, 8992-8997.

104. N. Pellegri, R. Trbojevich, O. DeSanctis and K. Kadono, *Fabrication of pbs nanoparticles embedded in silica gel by reverse micelles and sol-gel routes*, J. Sol-Gel Sci. Technol. **8** (1997), no. 1-3, 1023-1028.

105. A. Lobo, T. Moller, M. Nagel, H. Borchert, S. G. Hickey and H. Weller, *Photoelectron spectroscopic investigations of chemical bonding in organically stabilized pbs nanocrystals*, J. Phys. Chem. B **109** (2005), no. 37, 17422-17428.

106. A. Watt, E. Thomsen, P. Meredith and H. Rubinsztein-Dunlop, *A new approach to the synthesis of conjugated polymer-nanocrystal composites for heterojunction optoelectronics*, Chem. Commun. (2004), no. 20, 2334-2335.

107. D. J. Asunskis, I. L. Bolotin, A. T. Wroble, A. M. Zachary and L. Hanley, *Lead sulfide nanocrystal-polymer composites for optoelectronic applications*, Macromol. Symp. **268** (2008), 33-37.

108. A. A. Patel, F. X. Wu, J. Z. Zhang, C. L. Torres-Martinez, R. K. Mehra, Y. Yang and S. H. Risbud, *Synthesis, optical spectroscopy and ultrafast electron dynamics of pbs nanoparticles with different surface capping*, J. Phys. Chem. B **104** (2000), no. 49, 11598-11605.

109. T. W. F. Chang, S. Musikhin, L. Bakueva, L. Levina, M. A. Hines, P. W. Cyr and E. H. Sargent, *Efficient excitation transfer from polymer to nanocrystals*, Appl. Phys. Lett. **84** (2004), no. 21, 4295-4297.

110. L. Bakueva, S. Musikhin, M. A. Hines, T. W. F. Chang, M. Tzolov, G. D. Scholes and E. H. Sargent, *Size-tunable infrared (1000-1600 nm) electroluminescence from pbs quantum-dot nanocrystals in a semiconducting polymer*, Appl. Phys. Lett. **82** (2003), no. 17, 2895-2897.

111. A. Sashchiuk, E. Lifshitz, R. Reisfeld, T. Saraidarov, M. Zelner and A. Willenz, *Optical and conductivity properties of pbs nanocrystals in amorphous zirconia sol-gel films*, J. Sol-Gel Sci. Technol. **24** (2002), no. 1, 31-38.

112. T. Saraidarov, R. Reisfeld, A. Sashchiuk and E. Lifshitz, *Synthesis and characterization of lead sulfide nanoparticles in zirconia-silica-urethane thin films prepared by the sol-gel process*, J. Sol-Gel Sci. Technol. **26** (2003), no. 1-3, 533-540.

113. A. Martucci, P. Innocenzi, J. Fick and J. D. Mackenzie, *Zirconia-ormosil films doped with pbs quantum dots*, Journal of Non-Crystalline Solids **244** (1999), no. 1, 55-62.

114. F. Del Monte, Y. H. Xu and J. D. Mackenzie, *Preparation and characterization of pbs quantum dots doped ormocers*, J. Sol-Gel Sci. Technol. **17** (2000), no. 1, 37-45.

115. P. Jiang, Z. F. Liu and S. M. Cai, *Growing monodispersed pbs nanoparticles on self-assembled monolayers of 11-mercaptoundecanoic acid on au(111) substrate*, Langmuir **18** (2002), no. 11, 4495-4499.

116. R. Reisfeld, *Nanosized semiconductor particles in glasses prepared by the sol-gel method: Their optical properties and potential uses*, Journal of Alloys and Compounds **341** (2002), no. 1-2, 56-61.

117. B. Zhang, G. H. Li, J. Zhang, Y. Zhang and L. D. Zhang, *Synthesis and characterization of pbs nanocrystals in water/c12e9/cyclohexane microemulsions*, Nanotechnology **14** (2003), no. 4, 443-446.

118. C. B. Murray, C. R. Kagan and M. G. Bawendi, *Synthesis and characterization of monodisperse nanocrystals and close-packed nanocrystal assemblies*, Annu. Rev. Mater. Sci. **30** (2000), 545-610.

119. A. A. R. Watt, D. Blake, J. H. Warner, E. A. Thomsen, E. L. Tavenner, H. Rubinsztein-Dunlop and P. Meredith, *Lead sulfide nanocrystal: Conducting polymer solar cells*, J. Phys. D-Appl. Phys. **38** (2005), no. 12, 2006-2012.

120. A. Martucci, J. Fick, J. Schell, G. Battaglin and M. Guglielmi, *Microstructural and nonlinear optical properties of silica-titania sol-gel film doped with pbs quantum dots*, J. Appl. Phys. **86** (1999), no. 1, 79-87.

121. I. Moriguichi, K. Hosoi, H. Nagaoka, I. Tanaka, Y. Teraoka and S. Kagawa, *Stepwise growth of size-confined cds in the two-dimensional hydrophilic interlayers of langmuir-blodgett films by the repeated sulfidation intercalation technique*, J. Chem. Soc.-Faraday Trans. **90** (1994), no. 2, 349-354.

122. H. S. Nalwa, "Handbook of organic-inorganic hybrid materials and nanocomposites," American Scientific, 2003.

123. E. H. Sargent, *Infrared quantum dots*, Advanced Materials **17** (2005), no. 5, 515-522.

124. A. K. Arora, M. Rajalakshmi, T. R. Ravindran and V. Sivasubramanian, *Raman spectroscopy of optical phonon confinement in nanostructured materials*, J. Raman Spectrosc. **38** (2007), no. 6, 604-617.

125. T. V. Basova, N. M. Kurochkina, A. Y. Tsivadze and A. K. Ray, *Formation of hybrid inorganic/organic nanocomposites*, J. Electron. Mater. **39** (2010), no. 2, 145-148.

126. G. D. Smith, S. Firth, R. J. H. Clark and M. Cardona, *First- and second-order raman spectra of galena (pbs)*, J. Appl. Phys. **92** (2002), no. 8, 4375-4380.

127. K. S. Babu, T. R. Kumar, P. Haridoss and C. Vijayan, *Effect of the organic solvent on the formation and stabilization of cds and pbs nanoclusters*, Talanta **66** (2005), no. 1, 160-165.

128. B. D. Cullity and S. R. Stock, *Elements of x-ray diffraction*, Prentice Hall, 2001.

129. Y. Wang and N. Herron, *Nanometer-sized semiconductor clusters:Materials synthesis, quantum size effects, and photophysical properties*, Journal of Physical Chemistry **95** (1991), no. 2, 525-532.

130. K. M. Noone and D. S. Ginger, *Doping for speed: Colloidal nanoparticles for thin-film optoelectronics*, ACS Nano **3** (2009), no. 2, 261-265.

131. N. P. Gaponik, D. V. Talapin and A. L. Rogach, *A light-emitting device based on a cdte nanocrystal/polyaniline composite*, PCCP Phys. Chem. Chem. Phys. **1** (1999), no. 8, 1787-1789.

132. N. P. Gaponik, D. V. Talapin, A. L. Rogach and A. Eychmuller, *Electrochemical synthesis of cdte nanocrystal/polypyrrole composites for optoelectronic applications*, Journal of Materials Chemistry **10** (2000), no. 9, 2163-2166.

133. M. Y. Gao, B. Richter, S. Kirstein and H. Mohwald, *Electroluminescence studies on self-assembled films of ppv and cdse nanoparticles*, J. Phys. Chem. B **102** (1998), no. 21, 4096-4103.

134. J. Lee, V. C. Sundar, J. R. Heine, M. G. Bawendi and K. F. Jensen, *Full color emission from ii-vi semiconductor quantum dot-polymer composites*, Advanced Materials **12** (2000), no. 15, 1102-+.

135. Y. Yang, S. H. Xue, S. Y. Liu, J. M. Huang and J. C. Shen, *Fabrication and characteristics of zns nanocrystals/polymer composite doped with tetraphenylbenzidine single layer structure light-emitting diode*, Appl. Phys. Lett. **69** (1996), no. 3, 377-379.

136. N. Tessler, V. Medvedev, M. Kazes, S. H. Kan and U. Banin, *Efficient near-infrared polymer nanocrystat light-emitting diodes*, Science **295** (2002), no. 5559, 1506-1508.

137. K. N. Bourdakos, D. Dissanayake, T. Lutz, S. R. P. Silva and R. J. Curry, *Highly efficient near-infrared hybrid organic-inorganic nanocrystal electroluminescence device*, Appl. Phys. Lett. **92** (2008), no. 15, 3.

138. Y. Wang and N. Herron, *Photoconductivity of cds nanocluster-doped polymers*, Chem. Phys. Lett. **200** (1992), no. 1-2, 71-75.

139. B. Q. Sun, E. Marx and N. C. Greenham, *Photovoltaic devices using blends of branched cdse nanoparticles and conjugated polymers*, Nano Lett. **3** (2003), no. 7, 961-963.

140. W. J. E. Beek, M. M. Wienk and R. A. J. Janssen, *Hybrid solar cells from regioregular polythiophene and zno nanoparticles*, Adv. Funct. Mater. **16** (2006), no. 8, 1112-1116.

141. B. Pradhan, A. Bandyopadhyay and A. J. Pal, *Molecular level control of donor/acceptor heterostructures in organic photovoltaic devices*, Appl. Phys. Lett. **85** (2004), no. 4, 663-665.

142. H. S. Nalwa, "Handbook of organic-inorganic hybrid materials and nanocomposites," vol. 2: Nanocomposites, American Scientific, 2003.

143. J. Seo, S. J. Kim, W. J. Kim, R. Singh, M. Samoc, A. N. Cartwright and P. N. Prasad, *Enhancement of the photovoltaic performance in pbs nanocrystal:P3ht hybrid composite devices by post-treatment-driven ligand exchange*, Nanotechnology **20** (2009), no. 9, 6.

144. G. Kickelbick, *Hybrid materials, synthesis, characterization and applications*, Wiley-VCH, 2007.

145. A. Watt, T. Eichmann, H. Rubinsztein-Dunlop and P. Meredith, *Carrier transport in pbs nanocrystal conducting polymer composites*, Appl. Phys. Lett. **87** (2005), no. 25, 3.

146. K. R. Choudhury, M. Samoc, A. Patra and P. N. Prasad, *Charge carrier transport in poly(n-vinylcarbazodle): Cds quantum dot hybrid nanocomposite*, J. Phys. Chem. B **108** (2004), no. 5, 1556-1562.

147. V. Coropceanu, J. Cornil, D. A. da Silva, Y. Olivier, R. Silbey and J. L. Bredas, *Charge transport in organic semiconductors*, chemical reviews **107** (2007), no. 4, 926-952.

148. F. Li, D. I. Son, S. M. Seo, H. M. Cha, H. J. Kim, B. J. Kim, J. H. Jung and T. W. Kim, *Organic bistable devices based on core/shell cdse/zns nanoparticles embedded in a conducting poly(n-vinylcarbazole) polymer layer*, Appl. Phys. Lett. **91** (2007), no. 12, 3.

149. F. S. Li, D. I. Son, H. M. Cha, S. M. Seo, B. J. Kim, H. J. Kim, J. H. Jung and T. W. Kim, *Memory effect of cdse/zns nanoparticles embedded in a conducting poly[2-methoxy-5-(2-ethylhexyloxy)-1,4-phenylene-vinylene] polymer layer*, Appl. Phys. Lett. **90** (2007), no. 22, 3.

150. S. P. Mondal, V. S. Reddy, S. Das, A. Dhar and S. K. Ray, *Memory effect in a junction-like cds nanocomposite/conducting polymer poly[2-methoxy-5-(2-ethylhexyloxy)1,4-phenylene-vinylene] heterostructure*, Nanotechnology **19** (2008), no. 21, 4.

151. S. H. Yang, T. P. Nguyen, P. Le Rendu and C. S. Hsu, *Optical and electrical investigations of poly(p-phenylene vinylene)/silicon oxide and poly(p-phenylene vinylene)/titanium oxide nanocomposites*, Thin Solid Films **471** (2005), no. 1-2, 230-235.

152. S. A. Carter, J. C. Scott and P. J. Brock, *Enhanced luminance in polymer composite light emitting devices*, Appl. Phys. Lett. **71** (1997), no. 9, 1145-1147.

153. S. J. Su and N. Kuramoto, *Processable polyaniline-titanium dioxide nanocomposites: Effect of titanium dioxide on the conductivity*, Synth. Met. **114** (2000), no. 2, 147-153.

154. C. R. Kagan, D. B. Mitiz and C. D. Dimitrakopoulos, *Organic-inorganic hybrid materials as semiconducting channels in thin-film field-effect transistors* Science **286** (1999), 945-947.

155. J. Park, J. W. Lee, D. W. Kim, B. J. Park, H. J. Choi and J. S. Choi, *Pentacene thin-film transistor with poly(methyl methacrylate-co-methacrylic acid)/tio2 nanocomposite gate insulator*, Thin Solid Films **518** (2009), no. 2, 588-590.

156. R. P. Ortiz, A. Facchetti and T. J. Marks, *High-k organic, inorganic, and hybrid dielectrics for low-voltage organic field-effect transistors*, chemical reviews **110** (2009), no. 1, 205-239.

157. H. Y. Noh, Y. G. Seol, S. I. Kim and N. E. Leez, *Mechanically flexible low-leakage nanocomposite gate dielectrics for flexible organic thin-film transistors*, Electrochem. Solid State Lett. **11** (2008), no. 8, H218-H221.

158. F. Y. Yang, M. Y. Hsu, G. W. Hwang and K. J. Chang, *High-performance poly(3-hexylthiophene) top-gate transistors incorporating tio2 nanocomposite dielectrics*, Organic electronics **11**, no. 1, 81-88.

159. P. M. Burnham, I. Chambrier, D. L. Hughes, B. Isare, R. J. Poynter, A. K. Powell and M. J. Cook, *Synthesis, lead lability and ring deformation of three 1,4,8,11,15,18,22,25-octasubstituted phthalocyaninato lead derivatives*, J. Porphyr. Phthalocyanines **10** (2006), no. 9-10, 1202-1211.

160. H. Hikita, S. Asai, Y. Himukashi and T. Ishikawa, *Absorption of hydrogen sulfide into aqueous ammonia and sodium hydroxide solutions.*, Journal of Chemical Engineering (Japan) **32** (1968), 278-285.

161. N. V. Tkachenko, *Optical spectroscopy, methods and instrumentation*, Elsevier, 2006.

162. I. Chambrier, M. J. Cook, M. Helliwell and A. K. Powell, *X-ray crystal-structure of a mesogenic octa-substituted phthalocyanine*, J. Chem. Soc.-Chem. Commun. (1992), no. 5, 444-446.

163. J. Tauc and A. Menth, *States in the gap*, Journal of Non-Crystalline Solids **8** (1972), no. 10, 569.

164. B. R. Hyun, Y. W. Zhong, A. C. Bartnik, L. F. Sun, H. D. Abruna, F. W. Wise, J. D. Goodreau, J. R. Matthews, T. M. Leslie and N. F. Borrelli, *Electron injection from colloidal pbs quantum dots into titanium dioxide nanoparticles*, ACS Nano **2** (2008), no. 11, 2206-2212.

165. Y. Alfredsson, B. Brena, K. Nilson, J. Ahlund, L. Kjeldgaard, M. Nyberg, Y. Luo, N. Martensson, A. Sandell, C. Puglia and H. Siegbahn, *Electronic structure of a vapor-deposited metal-free phthalocyanine thin film*, J. Chem. Phys. **122** (2005), no. 21, 6.

166. R. Schlaf, H. Murata and Z. H. Kafafi, *Work function measurements on indium tin oxide films*, J. Electron Spectrosc. Relat. Phenom. **120** (2001), no. 1-3, 149-154.

167. D. R. Lide (Editor), *Crc handbook of chemistry and physics. 2000-2001*, CRC, 2000.

168. N. M. Amar, R. D. Gould and A. M. Saleh, *Structural and electrical properties of the alpha-form of metal-free phthalocyanine (alpha-h2pc) semiconducting thin films*, Curr. Appl. Phys. **2** (2002), no. 6, 455-460.

169. J. Blochwitz, M. Pfeiffer, T. Fritz and K. Leo, *Low voltage organic light emitting diodes featuring doped phthalocyanine as hole transport material*, Appl. Phys. Lett. **73** (1998), no. 6, 729-731.

170. B. I. Shklovskii and A. L. Efros, *Electronic properties of doped semiconductors*, Springer-Verlag, Berline Heidelberg-New York, 1984.

171. N. F. Mott and E. A. Davis, *Electronic processes in non-crystalline materials*, Oxford university press, USA, 1979.

172. A. J. Campbell, M. S. Weaver, D. G. Lidzey and D. D. C. Bradley, *Bulk limited conduction in electroluminescent polymer devices*, J. Appl. Phys. **84** (1998), no. 12, 6737-6746.

173. W. Brutting, S. Berleb and A. G. Muckl, *Space-charge limited conduction with a field and temperature dependent mobility in alq light-emitting devices*, Synth. Met. **122** (2001), 99-104.

174. N. B. Pendyala and K. Rao, *Identification of surface states in pbs quantum dots by temperature dependent photoluminescence*, J. Lumines. **128** (2008), no. 11, 1826-1830.

175. A. I. Lakatos and M. Abkowitz, *Electrical properties of amorphous se, as2se3, and as2s3*, Physical Review B **3** (1971), no. 6, 1791-&.

176. S. O. Kasap, *Principles of electronic materials and devices*, McGraw-Hill, 2006.

177. M. Razeghi, *Fundamentals of solid state engineering*, Kluwer Academic, 2002.

List of publications

1- Khozaee Z., Cook M.J., Ray A.K, “Formation and characterization of lead sulphide quantum dots embedded in spun phthalocyanine films”, The 7th International Conference of Organic Electronics (ICOE), Paris, France, 22-25 June 2010.

2- Khozaee Z., Cook M.J., Ray A.K, "Bistable switching in the lead sulphide /metal-free phthalocyanine structure". (under preparation)

3- Khozaee Z., Ray A.K, "Hybrid nanocomposites containing lead sulphide quantum dots": a chapter in Nanotechnology, John Wiley & Sons, Editor: A. Eftekhari (under preparation)

Patent

The intellectual property right belongs jointly to the University of East Anglia and Queen Mary, University of London. Both universities are now process in identifying the patentable results for commercial exploitation.